

Copyright Warning & Restrictions

The copyright law of the United States (Title 17, United States Code) governs the making of photocopies or other reproductions of copyrighted material.

Under certain conditions specified in the law, libraries and archives are authorized to furnish a photocopy or other reproduction. One of these specified conditions is that the photocopy or reproduction is not to be “used for any purpose other than private study, scholarship, or research.” If a user makes a request for, or later uses, a photocopy or reproduction for purposes in excess of “fair use” that user may be liable for copyright infringement,

This institution reserves the right to refuse to accept a copying order if, in its judgment, fulfillment of the order would involve violation of copyright law.

Please Note: The author retains the copyright while the New Jersey Institute of Technology reserves the right to distribute this thesis or dissertation

Printing note: If you do not wish to print this page, then select “Pages from: first page # to: last page #” on the print dialog screen

The Van Houten library has removed some of the personal information and all signatures from the approval page and biographical sketches of theses and dissertations in order to protect the identity of NJIT graduates and faculty.

ABSTRACT

MAGNETIC FIELD EFFECTS ON LITHIUM ION BATTERIES

**by
Kevin Mahon**

The Nobel Prize in Chemistry 2019 was just recently awarded to John B. Goodenough, M. Stanley Whittingham, and Akira Yoshino for the development of lithium-ion batteries. Lithium-ion batteries have seen use in many different industries and applications such as in portable devices, power grids, and electric vehicles. As lithium-ion batteries become more commonplace they will need to be modeled more extensively. The magnetic field effect on lithium-ion batteries has not been studied significantly since they were first discovered.

Modeling these batteries is still difficult because of the many complexities of the operation of a battery. Lithium-ion batteries are commonly modeled through equivalent circuit models (ECM's) in where experimental data is replicated through the use of parallel and series resistors and capacitors. The values of these resistance and capacitances are tuned to the experimental data. The other route for modeling lithium-ion batteries involves looking at the fundamental electrochemistry that governs them. This involves solving the differential equations for conservation of mass and conservation of charge. These equations are very nonlinear, dependent on each other, and do not have closed-form solutions.

One-dimensional and two-dimensional batteries were modeled based on the underlying physics of a lithium-ion battery. Magnetic fields were injected into the batteries to see the effect on their voltage and current charge/discharge characteristics. It was observed that external magnetic fields result in reduced times during charging and discharging of lithium-ion batteries due to the paramagnetic nature of lithium ions.

**MAGNETIC FIELD EFFECTS
ON LITHIUM ION BATTERIES**

**by
Kevin Mahon**

**A Thesis
Submitted to the Faculty of
New Jersey Institute of Technology
in Partial Fulfillment of the Requirements for the Degree of
Master of Science in Electrical Engineering**

**Helen and John C. Hartmann Department of
Electrical and Computer Engineering**

December 2019

Blank Page

APPROVAL PAGE

**MAGNETIC FIELD EFFECTS
ON LITHIUM ION BATTERIES**

Kevin Mahon

Dr. Edip Niver, Thesis Advisor Date
Professor of Electrical and Computer Engineering, NJIT

Dr. Ali N. Akansu, Committee Member Date
Professor of Electrical and Computer Engineering, NJIT

Dr. Marek Sosnowski, Committee Member Date
Professor of Electrical and Computer Engineering, NJIT

Dr. Carlos Pereira, Committee Member Date
ARDEC, Picattiny Arsenal, US Army, Dover NJ

BIOGRAPHICAL SKETCH

Author: Kevin Mahon

Degree: Master of Science

Date: December 2019

Undergraduate and Graduate Education:

- Master of Science in Electrical Engineering,
New Jersey Institute of Technology, Newark, NJ, 2019
- Bachelor of Science in Electrical and Computer Engineering,
Rowan University, Glassboro, NJ, 2018

Major: Electrical Engineering

To my family.

ACKNOWLEDGMENT

I would first like to thank my thesis advisor, Professor Edip Niver to give me the opportunity to pursue a master thesis. This has given me the chance to improve my technical skills and writing skills in an academic environment. His support and recommendations were instrumental in this research effort. I would also like to thank Professor Ali N. Akansu, Professor Marek Sosnowski, and Dr. Carlos Periera for serving as my committee members. I also want to thank students Dakota Regner, Theofilos Kolilas, and Jonathan Davila.

Furthermore I would like to acknowledge all the help and suggestions including physical batteries to Dr. Andrew Manning of Lithium Battery Engineering, Dover, NJ. Additional thanks are due to Oksana Manzhura and Richard Salvador for developing the software tools to characterize the batteries throughout this work.

TABLE OF CONTENTS

Chapter	Page
1 INTRODUCTION	1
1.1 Battery Applications	1
1.2 Types of Batteries	2
1.3 Battery Operation	4
1.4 Lithium Ion Battery	7
2 MODELING LITHIUM ION BATTERIES	12
2.1 Physics Based Modeling	12
2.1.1 Continuity Equation	13
2.1.2 Conservation of Charge	13
2.1.3 Conservation of Mass in Electrolyte	13
2.1.4 Conservation of Mass in Solid Phase	14
2.1.5 Conservation of Charge in Electrolyte	15
2.1.6 Conservation of Charge in Solid Phase	16
2.1.7 Butler-Volmer Kinetic Equation	17
2.2 Equivalent Circuit Model	18
2.3 Magnetic Field Effect	21
3 RESEARCH	24
3.1 COMSOL Lithium Battery Interface	24
3.2 COMSOL 1D Modeling	29
3.2.1 Model Definition	29

3.2.2	Global Definitions	31
3.2.3	Geometries and Meshes	39
3.2.4	Charge Balance Solid Negative	41
3.2.5	Charge Balance Solid Positive	44
3.2.6	Charge Balance Electrolyte Negative	47
3.2.7	Charge Balance Electrolyte Separator	51
3.2.8	Charge Balance Electrolyte Positive	56
3.2.9	Material Balance Electrolyte Negative	59
3.2.10	Material Balance Electrolyte Separator	63
3.2.11	Material Balance Electrolyte Positive	67
3.2.12	Material Balance Solid Negative	70
3.2.13	Material Balance Solid Positive	75
3.2.14	Linear Extrusions	78
3.3	COMSOL 2D Modeling	82
3.3.1	Model Definition	82
3.3.2	Global Definitions	84
3.3.3	Geometries and Meshes	86
3.3.4	Charge Balance Solid Negative	90
3.3.5	Charge Balance Solid Positive	93
3.3.6	Charge Balance Electrolyte Negative	96
3.3.7	Charge Balance Electrolyte Separator	100
3.3.8	Charge Balance Electrolyte Positive	105
3.3.9	Material Balance Electrolyte Negative	109
3.3.10	Material Balance Electrolyte Separator	113

3.3.11	Material Balance Electrolyte Positive	118
3.3.12	Material Balance Solid Negative	121
3.3.13	Material Balance Solid Positive	126
3.3.14	Linear Extrusions	130
3.4	Magnetic Field	134
3.5	Experiment Setup	137
4	SIMULATION RESULTS AND EXPERIMENTAL RESULTS	141
4.1	1D Model	141
4.1.1	Discharge Charge Curves	141
4.1.2	MBEN, MBES, MBEP	142
4.1.3	CBEN, CBES, CBEP	143
4.1.4	MBSN, MBSP	145
4.1.5	CBSN	148
4.2	2D Model	150
4.2.1	PMF Discharge Charge Curves	150
4.2.2	PMF MBEN, MBES, MBEP	151
4.2.3	PMF CBEN, CBES, and CBEP	153
4.2.4	PMF MBSN and MBSP	155
4.2.5	PMF CBSN	158
4.2.6	NMF Discharge Charge Curves	160
4.2.7	NMF MBEN, MBES, MBEP	160
4.2.8	NMF CBEN, CBES, and CBEP	162
4.2.9	NMF MBSN and MBSP	164

4.2.10	PMF CBSN	167
4.3	Experimental Measurements	169
4.3.1	Magnetic Fields Generated from Coil	169
4.3.2	Small Battery LTB8	171
4.3.3	Small Battery LTB1	174
4.3.4	Big Battery FE19	177
5	CONCLUSION	180

LIST OF TABLES

Chapter	Page
1.1 Cathode Active Materials	9
1.2 Anode Active Materials	10
1.3 Electrolyte Materials	11
3.1 Variables Subnode	36
3.2 Constants and Parameters	38
3.3 1D Model, CBSN Parameters	42
3.4 1D Model, CBSP Parameters	45
3.5 1D Model, CBSP Flux/Source	47
3.6 1D Model, CBEN Parameters	48
3.7 1D Model, CBEN Flux/Source	51
3.8 1D Model, CBES Parameters	52
3.9 1D Model, CBES Flux/Source 1	55
3.10 1D Model, CBES Flux/Source 2	55
3.11 1D Model, CBEP Parameters	56
3.12 1D Model, CBEP Flux/Source	59
3.13 1D Model, MBEN Parameters	60
3.14 1D Model, MBEN Flux/Source	63
3.15 1D Model, MBES Parameters	64
3.16 1D Model, MBES Flux/Source 1	66
3.17 1D Model, MBES Flux/Source 2	67
3.18 1D Model, MBEP Parameters	68

3.19	1D Model, MBEP Flux/Source	70
3.20	1D Model, MBSN Parameters	73
3.21	1D Model, MBSN Flux/Source	75
3.22	1D Model, MBSP Parameters	76
3.23	1D Model, MBSP Flux/Source	78
3.24	Constants and Parameters 2	86
3.25	2D Model, CBSN Parameters	91
3.26	2D Model, CBSP Parameters	94
3.27	2D Model, CBSP Flux/Source	96
3.28	2D Model, CBEN Parameters	97
3.29	2D Model, CBEN Flux/Source	100
3.30	2D Model, CBES Parameters	101
3.31	2D Model, CBES Flux/Source 1	104
3.32	2D Model, CBES Flux/Source 2	105
3.33	2D Model, CBEP Parameters	106
3.34	2D Model, CBEP Flux/Source	109
3.35	2D Model, MBEN Parameters	110
3.36	2D Model, MBEN Flux/Source	113
3.37	2D Model, MBES Parameters	114
3.38	2D Model, MBES Flux/Source 1	117
3.39	2D Model, MBES Flux/Source 2	117
3.40	2D Model, MBEP Parameters	119
3.41	2D Model, MBEP Flux/Source	121
3.42	2D Model, MBSN Parameters	124

3.43	2D Model, MBSN Flux/Source	126
3.44	2D Model, MBSP Parameters	128
3.45	2D Model, MBSP Flux/Source	130
3.46	2D Model, CBEN Magnetic Field Parameters	135
3.47	2D Model, CBES Magnetic Field Parameters	135
3.48	2D Model, CBEP Magnetic Field Parameters	136
3.49	2D Model, CBSN Magnetic Field Parameters	136
3.50	2D Model, CBSP Magnetic Field Parameters	137

LIST OF FIGURES

Chapter		Page
1.1	Three regions of a battery.	4
1.2	Charge operation.	5
1.3	Discharge operation.	6
2.1	Equivalent circuit model.	20
2.2	ECM simulation.	21
3.1	1D model, model tree.	30
3.2	1D model, model diagram.	31
3.3	Electrolyte conductivity.	32
3.4	Negative equilibrium voltage.	33
3.5	Positive equilibrium voltage.	34
3.6	Step function.	36
3.7	1D model, 1d domain.	39
3.8	1D model, 1d points.	39
3.9	1D model, 1d domain regions.	40
3.10	1D model, 1d domain mesh.	40
3.11	1D model, 2d domain.	40
3.12	1D model, 2d domain boundaries.	41
3.13	1D model, 2d domain mesh.	41
3.14	1D model, cbsn region.	42
3.15	1D model, cbsn zero value.	43
3.16	1d model, cbsn zero flux boundary.	44

3.17	1D model, cbsp region.	44
3.18	1D model, cbsp zero flux boundary.	46
3.19	1D model, cbsp applied current boundary.	47
3.20	1D model, cben region.	47
3.21	1D model, cben dirichlet/flux boundary.	49
3.22	1D model, cben zero flux boundary.	50
3.23	1D model, cbes region.	51
3.24	1D model, cbes dirichlet/flux boundary 1.	53
3.25	1D model, cbes dirichlet/flux boundary 2.	54
3.26	1D model, cbep region.	56
3.27	1D model, cbep dirichlet/flux boundary.	58
3.28	1D model, cbep zero flux boundary.	58
3.29	1D model, mben region.	60
3.30	1D model, mben dirichlet/flux boundary.	61
3.31	1D model, mben zero flux boundary.	62
3.32	1D model, mbes region.	63
3.33	1D model, mbes dirichlet/flux boundary 1.	65
3.34	1D model, mbes dirichlet/flux boundary 2.	65
3.35	1D model, mbep region.	67
3.36	1D model, mbep dirichlet/flux boundary.	69
3.37	1D model, mbep zero flux boundary.	69
3.38	1D model, mbsn region.	71
3.39	1D model, mbsn flux/top boundary.	72
3.40	1D model, mbsn zero flux boundaries.	74

3.41	1D model, mbsp region.	75
3.42	1D model, mbsp flux/top boundary.	76
3.43	1D model, mbsp zero flux boundaries.	77
3.44	1D model, linear extrusion 1 source.	79
3.45	1D model, linear extrusion 1 destination.	79
3.46	1D model, linear extrusion 2 source.	80
3.47	1D model, linear extrusion 2 destination.	80
3.48	1D model, linear extrusion 3 source.	81
3.49	1D model, linear extrusion 3 destination.	81
3.50	1D model, linear extrusion 4 source.	82
3.51	1D model, linear extrusion 4 destination.	82
3.52	2D model, model tree.	83
3.53	2D model, model diagram.	84
3.54	2D model, 2d domain.	86
3.55	2D model, 2d points.	86
3.56	2D model, 2d domain boundaries.	87
3.57	2D model, 2d domain regions.	88
3.58	2D model, 2d domain mesh.	88
3.59	2D model, three dimensional domain.	89
3.60	2D model, 3d domain boundaries.	89
3.61	2D model, 3d domain mesh.	90
3.62	2D model, cbsn region.	90
3.63	2D model, cbsn zero value boundary.	92
3.64	2d model, cbsn zero flux boundaries.	92

3.65	2D model, cbsp region.	93
3.66	2D model, cbsp zero flux boundaries.	95
3.67	2D model, cbsp applied current boundary.	96
3.68	2D model, cben region.	96
3.69	2D model, cben dirichlet/flux boundary.	99
3.70	2D model, cben zero flux boundaries.	99
3.71	2D model, cbes region.	100
3.72	2D model, cbes dirichlet/flux boundary 1.	102
3.73	2D model, cbes dirichlet/flux boundary 2.	103
3.74	2D model, cbes zero flux boundaries.	103
3.75	2D model, cbep region.	105
3.76	2D model, cbep dirichlet/flux boundary.	108
3.77	2D model, cbep zero flux boundaries.	108
3.78	2D model, mben region.	109
3.79	2D model, mben dirichlet/flux boundary.	111
3.80	2D model, mben zero flux boundaries.	112
3.81	2D model, mbes region.	113
3.82	2D model, mbes dirichlet/flux boundary 1.	115
3.83	2D model, mbes dirichlet/flux boundary 2.	115
3.84	2D model, mbes zero flux boundaries.	116
3.85	2D model, mbep region.	118
3.86	2D model, mbep dirichlet/flux boundary.	120
3.87	2D model, mbep zero flux boundaries.	120
3.88	2D model, mbsn region.	122

3.89	2D model, mbsn flux/top boundary.	123
3.90	2D model, mbsn zero flux boundaries.	125
3.91	2D model, mbsp region.	127
3.92	2D model, mbsp flux/top boundary.	128
3.93	2D model, mbsp zero flux boundaries.	129
3.94	2D model, linear extrusion 1 source.	131
3.95	2D model, linear extrusion 1 destination.	131
3.96	2D model, linear extrusion 2 source.	132
3.97	2D model, linear extrusion 2 destination.	132
3.98	2D model, linear extrusion 3 source.	133
3.99	2D model, linear extrusion 3 destination.	133
3.100	2D model, linear extrusion 4 source.	134
3.101	2D model, linear extrusion 4 destination.	134
3.102	Experimental charging circuit.	137
3.103	Experimental discharging circuit.	137
3.104	Experimental coil.	138
3.105	Experimental batteries.	139
3.106	Experimental small battery on coil.	140
3.107	Experimental large battery on coil.	140
4.1	COMSOL 1d model, discharge charge curve.	141
4.2	1D model, discharge charge curve.	141
4.3	COMSOL 1d model, electrolyte concentration.	142
4.4	1D model, electrolyte concentration.	142
4.5	1D model, electrolyte concentration 2000s-4000s.	143

4.6	1D model, electrolyte concentration 4000s-5000s.	143
4.7	COMSOL 1d model, electrolyte potential 0-2000s.	144
4.8	1D model, electrolyte potential 0-2000s.	144
4.9	1D model, electrolyte potential 2000s-4000s.	144
4.10	1D model, electrolyte potential 4000s-5000s.	144
4.11	COMSOL 1d model, solid concentration.	145
4.12	1D model, solid negative phase concentration.	146
4.13	1D model, solid positive phase concentration.	146
4.14	1D model, mbsn surface plot 10s.	146
4.15	1D model, mbsp surface plot 10s.	146
4.16	1D model, mbsn surface plot 1200s.	147
4.17	1D model, mbsp surface plot 1200s.	147
4.18	1D model, mbsn surface plot 1800s.	148
4.19	1D model, mbsp surface plot 1800s.	148
4.20	1D model, cbsn 0-2000s.	149
4.21	1D model, cbsn 2000s-4000s.	149
4.22	COMSOL 1d model, cbsn 4000s-5000s.	149
4.23	COMSOL 2d model, discharge charge curves.	150
4.24	2D model, 0mT electrolyte concentration 0-2000s.	151
4.25	2D model, 0.5mT electrolyte concentration 0-2000s.	151
4.26	2D model, 0mT electrolyte concentration 2000s-4000s.	152
4.27	2D model, 0.5mT electrolyte concentration 2000s-4000s.	152
4.28	2D model, 0mT electrolyte concentration 4000s-5000s.	153
4.29	2D model, 0.5mT electrolyte concentration 4000s-5000s.	153

4.30	2D model, 0mT electrolyte potential 0-2000s.	154
4.31	2D model, 0.5mT electrolyte potential 0-2000s.	154
4.32	2D model, 0mT electrolyte potential 2000s-4000s.	154
4.33	2D model, 0.5mT electrolyte potential 2000s-4000s.	154
4.34	2D model, 0mT electrolyte potential 4000s-5000s.	155
4.35	2D model, 0.5mT electrolyte potential 4000s-5000s.	155
4.36	2D model, 0mT mbsn 10s.	156
4.37	2D model, 0.5mT mbsn 10s.	156
4.38	2D model, 0mT mbsn 500s.	156
4.39	2D model, 0.5mT mbsn 500s.	156
4.40	2D model, 0mT mbsp 10s.	157
4.41	2D model, 0.5mT mbsp 10s.	157
4.42	2D model, 0mT mbsp 500s.	157
4.43	2D model, 0.5mT mbsp 500s.	157
4.44	2D model, 0mT cbsn 0-2000s.	158
4.45	2D model, 0.5mT cbsn 0-2000s.	158
4.46	2D model, 0mT cbsn 2000s-4000s.	159
4.47	2D model, 0.5mT cbsn 2000s-4000s.	159
4.48	2D model, 0mT cbsn 4000s-5000s.	159
4.49	2D model, 0.5mT cbsn 4000s-5000s.	159
4.50	2D model, nmf discharge charge curves.	160
4.51	2D model, 0.75mT electrolyte concentration 0-2000s.	161
4.52	2D model, -1mT electrolyte concentration 0-2000s.	161
4.53	2D model, 0.75mT electrolyte concentration 2000s-4000s.	161

4.54	2D model, -1mT electrolyte concentration 2000s-4000s.	161
4.55	2D model, 0.75mT electrolyte concentration 4000s-5000s.	162
4.56	2D model, -1mT electrolyte concentration 4000s-5000s.	162
4.57	2D model, 0.75mT electrolyte potential 0-2000s.	163
4.58	2D model, -1mT electrolyte potential 0-2000s.	163
4.59	2D model, 0.75mT electrolyte potential 2000s-4000s.	163
4.60	2D model, -1mT electrolyte potential 2000s-4000s.	163
4.61	2D model, 0.75mT electrolyte potential 4000s-5000s.	164
4.62	2D model, -1mT electrolyte potential 4000s-5000s.	164
4.63	2D model, 0.75mT mbsn 10s.	165
4.64	2D model, -1mT mbsn 10s.	165
4.65	2D model, 0.75mT mbsn 500s.	165
4.66	2D model, -1mT mbsn 500s.	165
4.67	2D model, 0.75mT mbsp 10s.	166
4.68	2D model, -1mT mbsp 10s.	166
4.69	2D model, 0.75mT mbsp 500s.	167
4.70	2D model, -1mT mbsp 500s.	167
4.71	2D model, 0.75mT cbsn 0-2000s.	168
4.72	2D model, -1mT cbsn 0-2000s.	168
4.73	2D model, 0.75mT cbsn 2000s-4000s.	168
4.74	2D model, -1mT cbsn 2000s-4000s.	168
4.75	2D model, 0.75mT cbsn 4000s-5000s.	169
4.76	2D model, -1mT cbsn 4000s-5000s.	169
4.77	Magnetic fields 2mm into top of coil.	170

4.78	Magnetic fields 0mm into top of coil.	170
4.79	Magnetic fields 2mm into bottom of coil.	171
4.80	Magnetic fields 0mm into bottom of coil.	171
4.81	Small battery LTB8 charge current.	172
4.82	Small battery LTB8 charge voltage.	172
4.83	Small battery LTB8 optimal.	173
4.84	Small battery LTB8 discharge current.	174
4.85	Small battery LTB8 discharge voltage.	174
4.86	Small battery LTB1 charge current.	175
4.87	Small battery LTB1 charge voltage.	175
4.88	Small battery LTB1 optimal.	176
4.89	Small battery LTB1 discharge current.	177
4.90	Small battery LTB1 discharge voltage.	177
4.91	Big battery FE19 charge current.	178
4.92	Big battery FE19 charge voltage.	178
4.93	Big battery FE19 discharge current.	179
4.94	Big battery FE19 discharge voltage.	179

CHAPTER 1

INTRODUCTION

1.1 Battery Applications

Batteries come in many shapes and sizes and see many different applications. In recent years electrical storage has seen an increased interest due to the emergence of renewable sources of energy. Across the world nations have made self-imposed requirements on their fuel sources that power their electric grids. The issue with some of these renewable sources of energy are that they are not as reliable as other forms of energy. While coal or natural gas can be burned at any time of day, wind and solar only work when there is a breeze or the sun is up. For most of the history of electric grids around the world supply meets demand; electricity is supplied exactly when it is demanded. These two factors, reliability and demand, cause the need for energy storage if the world is to want to rely on these forms of energy. While the sun is up some of this energy can be supplied directly to the grid while some may be used to fill battery banks.

Electric vehicles have also seen an increased area of research for higher energy and more capacity batteries. Most people's concern with electric vehicles is range and charging times. If higher energy density batteries can be discovered, this would help to solve both the range and the charging issues. Another application for energy storage is that of smaller electronics or portable equipment such as phones, laptops, power tools, and other instruments. Higher density batteries in this case provide a longer charge that allows the user to charge their battery less frequently. If more capacity is the goal, a battery taking up the same space could last longer. If weight is a concern, the same capacity can be seen

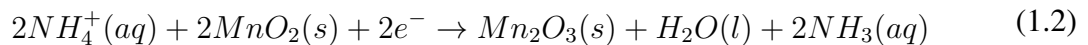
while taking up less space.

1.2 Types of Batteries

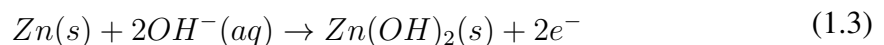
Batteries come in two different types, primary and secondary. Primary batteries are non-reversible single use batteries. These types of batteries see use in consumer electronics, weapon systems, medical applications, aerospace applications, and more. They are typically used when the price of rechargeable batteries is not economically feasible or charging is impractical because of their application. Typical primary batteries are the zinc-carbon battery or the alkaline dry cell [1]. The zinc-carbon battery has zinc as the anode; a graphite rod in the center, surrounded by a paste of manganese dioxide, ammonium and zinc chlorides, and carbon black, is the cathode. The reaction that occurs at the anode is approximated by



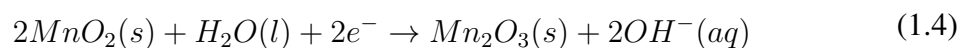
The reaction that occurs at the cathode is approximated as



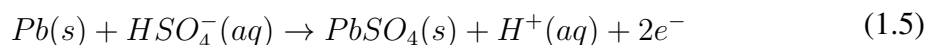
An alkaline dry cell is similar to the zinc-carbon battery except potassium hydroxide is used instead of ammonium chloride. At the anode the reaction is



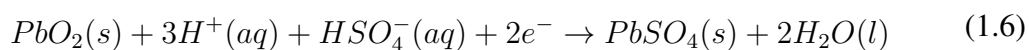
At the cathode the reaction is expressed as



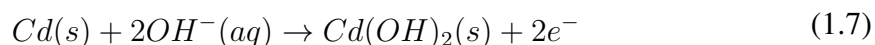
A natural evolution of the primary cell was the secondary cell which made up for its shortcoming of only being single use. The advantage of the secondary cell is that it is rechargeable. Two types of secondary batteries are the lead storage cells and the nickel-cadmium cells [1]. The lead storage cell consists of electrodes of lead alloy grids; one electrode is packed with a spongy lead to form the anode, and the other electrode is packed with lead (IV) oxide to form the cathode. The reaction that occurs at the anode is shown below



and the reaction occurring at the cathode is



In the nickel-cadmium cell the anode consists of cadmium and the cathode is hydrated nickel oxide (approximately NiOOH) on nickel; the electrolyte is potassium hydroxide. The reaction that occurs at the anode is



and the reaction occurring at the cathode is



1.3 Battery Operation

A typical battery is composed of three regions; the negative electrode, the separator, and the positive electrode. These three regions are shown below in Figure 1.1.

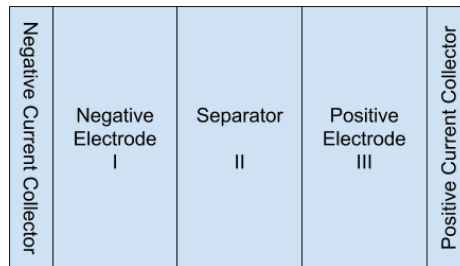


Figure 1.1 Three regions of a battery.

All three regions are immersed in an electrolyte that allows positive and negative ions to move between the two electrodes. Connected to the the positive electrode is the positive current collector and connected to the negative electrode is the negative current collector. When the battery is being charged an external voltage source is connected to the negative current collector and the positive current collector. Pictured below in Figure 1.2 is when the battery is being charged.

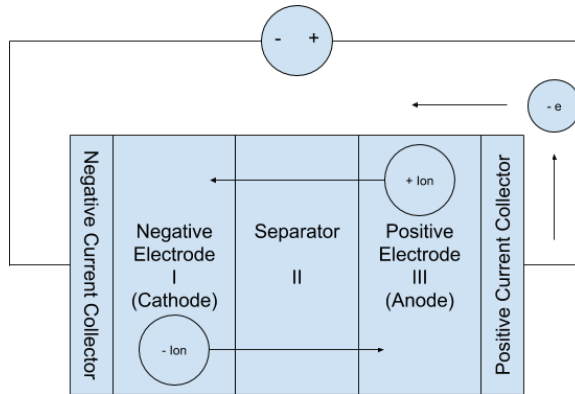


Figure 1.2 Charge operation.

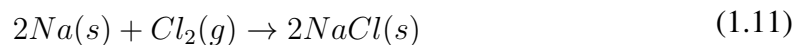
The negative electrode acts as the cathode where a reduction reaction occurs which produces a positive ion and an electron. This relation shown below corresponds to the half reaction of sodium chloride



The positive electrode acts as the anode where an oxidation reaction occurs which consumes the now free positive ion and electron. This relation shown below corresponds to the half reaction of sodium chloride



Presenting half reactions allows more concentration into what each electrode material is contributing. Shown below is the full reaction for sodium chloride



Electrons move from the anode to the positive current collector, from the positive current collector to an external voltage source, from the external voltage source to the negative current collector, and from the negative current collector to the cathode. For a discharge operation much of the opposite occurs as shown in Figure 1.3.

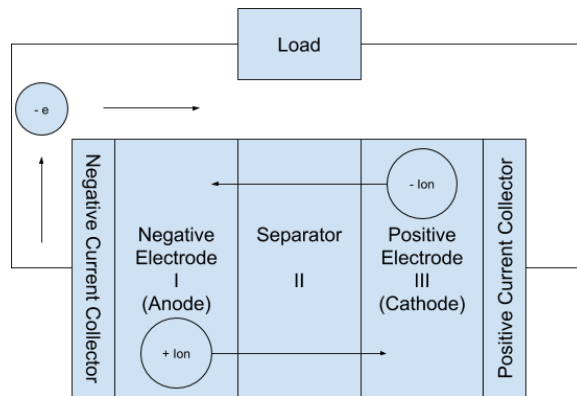


Figure 1.3 Discharge operation.

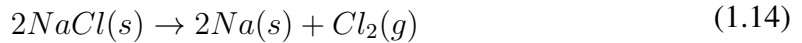
When the battery is discharged the negative electrode is the anode, the oxidation reaction that occurs for the case of sodium chloride is given by



For discharge the positive electrode acts as the cathode and the reduction reaction that occurs for the case of sodium chloride is given as



Combining both of these half reactions produces the full reaction shown below as



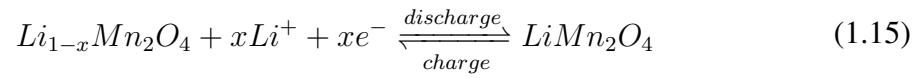
Positive ions move from the anode to the cathode through the electrolyte and the separator as negative ions move from the cathode to the anode. The cathode builds up a positive charge during this exchange and the anode builds up a negative charge. This creates a voltage difference between the anode and the cathode. In discharge, electrons move from the anode to the negative current collector, from the negative current collector to an external load, from the external load to the positive current collector, and from the positive current collector to the cathode [2].

1.4 Lithium Ion Battery

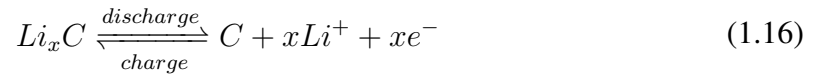
Lithium has seen recent interest because of its desirable properties. Two of those properties are its higher energy density compared to other comparable cells and its higher voltage. Compared to NiMh you could create a battery with the same energy but it would be half the size and half the weight. Typical NiMh and NiCd rechargeable cells operate about 1.2-1.5V nominal, whereas lithium-ion cells typically operate between 3.2 and 3.8V nominal. Having a high voltage is important in that it means that you need to connect fewer cells together in series in order to achieve a desired pack voltage [3]. Shown below in Tables 1.1 - 1.3 are some of the more commonly used materials in lithium ion batteries for the cathode, anode, and electrolyte respectively [4].

Considering lithium manganese oxide (LMO) batteries as an example, during charging the Li^+ escapes from the $LiMn_2O_4$ at the cathode, under the electromotive force, the Li^+ passes through the electrolyte and embeds into the carbon interlayer of the graphite.

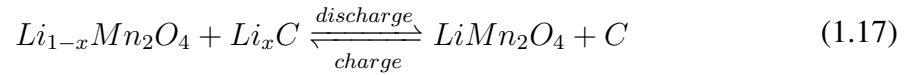
Thus the lithium and carbon interlayer are combined internally. When discharging, the Li^+ escapes from the carbon interlayer of the anode, through an opposite process under the electromotive force, and embeds into the anode $LiMn_2O_4$ [5]. The reaction in the anode is



The reaction for the cathode is



The overall reaction is shown below



Selection of an appropriate cathode depends on the particular application and desired properties. For cathode materials that may be higher power capability, cost, safety, energy density, nominal voltage, or stability.

Table 1.1 Cathode Active Materials

Cathode Material	Specific Capacity $mAhg^{-1}$	Midpoint Voltage Versus Li at at $\frac{C}{20}$	Comments
$LiCoO_2$	140-155	3.9	Prevalent in portable electronics, cobalt is expensive
$LiNi_{0.8}Co_{0.15}Al_{0.05}O_2$	200	3.73	High end applications (satellites, etc.), high capacity, safety comparable to $LiCoO_2$
$LiNi_{1-x-y}Co_xMn_yO_2$	140-180	-3.8	One of the prospective automotive li-ion battery cathode candidates, slightly safer than $LiCoO_2$
$LiMn_2O_4$	100-120	4.05	Inexpensive, safer than $LiCoO_2$, poor cycling at elevated temperatures due to manganese (Mn_{2+}) solubility in electrolytes
$LiFePO_4$	160	3.45	Lower energy, safer alternative to $LiNi_{1-x-y}Co_xMn_yO_2$

Source: [4]

Anodes are typically made of some form of carbon either graphite or soft or hard carbons. Currently, the most common commercial anodes are carbons that possess relatively low surface area and intercalate lithium ions into their layered structure without forming metallic lithium under standard operating voltage, temperature, and current rate conditions [4]. Intercalation is the process by which a molecule is inserted into a lattice. It is also known as the reversible insertion of a guest species into a host lattice. Either molecules or ions can get inserted and host materials can be inorganic. Intercalation reactions are the basis of all Li-ion batteries.

Table 1.2 Anode Active Materials

Manufacturer	Grade	Type	Reversible Capacity $mAhg^{-1}$	First Cycle Efficiency %
Osaka Gas	MCMB 6-28	Soft Carbon, Graphitized at 2800 °C	295.3	92
	MCMB 10-28		326.9	92
	MCMB 25-28		334.0	92
	OMAC-15	Soft Carbon,	364.9	96
	OMAC-21	Graphitized	356.0	93
Hydro-Quebec	SNG-12		370	86
Superior Graphite	LBG-1025	Natural Graphite	360	91
Superior Graphite	SLA-1020	Thermally Purified Natural Graphite	363	92
Superior Graphite	SLA-1015	Surface Treated Natural Graphite	352	92

Source: [4]

Electrolytes for lithium ion batteries are typically chosen to meet certain criteria. It should be completely dissolved and dissociated in the solvent mixture. The solvated lithium cations should move within the media with high mobility. The anion should be inert to electrolyte solvents. The salt anion should be stable against oxidative decomposition at the cathode. Both the anion and the cation should remain inert toward all the cell components, such as separator, electrode substrates, and cell packaging materials. And the anion should be nontoxic and stable against thermally induced reactions with electrolyte solvents and other cell components [4].

Table 1.3 Electrolyte Materials

Solvent	MW g mol^{-1}	T _m °C	T _b °C	T _f °C	η , cP 25 °C	Dipole moment debye	d, g cm^{-3}
Ethylene Carbonate, EC	88	36.4	248	160	1.90 (40 °C)	4.61	1.321
Propylene Carbonate, PC	102	-48.8	242	132	2.53	4.81	1.200
Dimethyl Carbonate, DMC	90	4.6	91	18	0.59 (40 °C)	0.76	1.063
Diethyl Carbonate DEC	118	-74.3	126	31	0.75	0.96	0.969
Ethyl Methyl Carbonate, EMC	104	-53	110	23.9	0.65	0.89	1.006

Source: [4]

CHAPTER 2

MODELING LITHIUM ION BATTERIES

Modeling lithium ion batteries is a difficult task because of the nature of the equations that govern them. They are extremely nonlinear and they depend on each other. No close-form solution exists for them, so the only way of solving them is employing numerical methods as presented in [6]. Some of the common methods for modeling lithium ion batteries. They include empirical models, electrochemical engineering models, ohmic porous-electrode models, pseudo-two dimensional models, multiphysics models, thermal models, stack models, and molecular/atomistic models. From a system engineering perspective they proposed ways of improving simulation time by reducing complexity of models. A molecular model was utilized in [7] to study the effects of pulse current charging. Their model involved 51 Li^+ molecules, 51 $TFSI^-$ (bis(trifluoromethanesulfonyl)imide) molecules, and 600 PC (propylene carbonate) molecules for a total of 8616 atoms to see the effect on diffusion.

2.1 Physics Based Modeling

Physics based modeling uses fundamental conservation laws to describe the electrochemical interactions in the battery. The most common model is based on Newman's model [8], and is what COMSOL's built-in one-dimensional model is based on [9]. There are typically four governing partial differential equations for the charge and mass conservation in the electrolyte and electrodes.

2.1.1 Continuity Equation

The continuity equation is used for mass or species conservation for both the electrolyte and the electrodes and is shown below

$$\frac{\partial \rho}{\partial t} = -\nabla \cdot (\rho V) \quad (2.1)$$

where ρ is the mass density and V is the velocity. The continuity equation simply states that the time evolution of the mass enclosed by a surface is equal to the mass that travels through that surface.

2.1.2 Conservation of Charge

Charge conservation also comes from the continuity equation. Shown below is the conservation of charge used for the electrolyte and the electrodes

$$\nabla \cdot j = -\frac{\partial \rho}{\partial t} \quad (2.2)$$

where j is the current density and ρ is the volumetric charge density.

2.1.3 Conservation of Mass in Electrolyte

Starting with the electrolyte is the conservation of mass, in this case the conservation of lithium in all three regions as shown in Figure 1.1. Shown below is the governing equation for the conservation of mass in the electrolyte phase

$$\epsilon_e \frac{\partial C_e}{\partial t} = \nabla \cdot (D_e^{eff} \nabla C_e) + \frac{j_{li}(1 - t_+)}{F} \quad (2.3)$$

where ϵ_e is the volume fraction of electrolyte, C_e is the concentration in electrolyte, D_e^{eff} is the diffusion coefficient, t_+ is the transference number, F is Faraday's constant, and j_{li} is the pore-wall flux across the interface. Each region of the battery also has initial conditions for the concentration of mass in the electrolyte phase. Also there are Neumann boundary conditions such as zero flux on both the current collectors and continuity on the internal boundaries of the interfaces of the negative, separator, and positive regions. There are also Dirichlet boundary conditions on the internal boundaries of the interfaces to make the concentrations equal at the boundaries. For a one dimensional domain the conditions are shown as

$$\begin{aligned}
-D_e^{eff} \frac{\partial C_e}{\partial x} \Big|_{x=0} &= 0 \\
-D_e^{eff} \frac{\partial C_e}{\partial x} \Big|_{x=L_{neg}^-} &= -D_e^{eff} \frac{\partial C_e}{\partial x} \Big|_{x=L_{neg}^+} \\
-D_e^{eff} \frac{\partial C_e}{\partial x} \Big|_{x=(L_{neg}+L_{sep})^-} &= -D_e^{eff} \frac{\partial C_e}{\partial x} \Big|_{x=(L_{neg}+L_{sep})^+} \\
-D_e^{eff} \frac{\partial C_e}{\partial x} \Big|_{x=L_{neg}+L_{sep}+L_{pos}} &= 0 \\
C_e(x, 0) &= C_e^{init}(x) \\
C_e(L_{neg}^-, t) &= C_e(L_{neg}^+, t) \\
C_e((L_{neg} + L_{sep})^-, t) &= C_e((L_{neg} + L_{sep})^+, t)
\end{aligned} \tag{2.4}$$

2.1.4 Conservation of Mass in Solid Phase

Conservation of mass with the solid phase is a little more complex. The solid electrodes are modeled on the porous electrode theory which states that the solid phase particles are uniformly distributed throughout the negative and positive electrodes and the electrolyte flows between these particles. The concentration at any given point in the positive or neg-

active electrode in the battery is taken to be the concentration at the surface of an equivalent spherical particle at that point. Lithium diffuses to the center of the particle according to Fick's Second Law which is shown below as

$$\frac{\partial C_s}{\partial t} = \frac{D_s}{r^2} \frac{\partial}{\partial r} \left(r^2 \frac{\partial C_s}{\partial r} \right) \quad (2.5)$$

where C_s is the concentration in the solid phase and D_s is the diffusion coefficient. The entire particle has initial conditions for the concentration of mass in the solid. Also there are Neumann boundary conditions such as zero flux at the center of the particle and an applied current density at the surface of the particle. These conditions are shown as

$$\begin{aligned} -D_s \frac{\partial C_s}{\partial r} \Big|_{r=0} &= 0 \\ -D_s \frac{\partial C_s}{\partial r} \Big|_{r=R_p} &= \frac{j_{li}}{a_s F} \\ C_s(r, 0) &= C_s^{init}(r) \end{aligned} \quad (2.6)$$

where j_{li} is the pore-wall flux across the interface, F is Faraday's constant, and a_s is the surface area to volume ratio.

2.1.5 Conservation of Charge in Electrolyte

For conservation of charge in the electrolyte the conservation of charge shown in equation (2.2) was modified. The partial differential equation for the electrolyte in all three regions is shown below

$$-j_{li} = \nabla \left(\kappa^{eff} \nabla \varphi_e + \kappa_d^{eff} \nabla \frac{\nabla C_e}{C_e} \right) \quad (2.7)$$

where j_{li} is the pore-wall flux across the interface, κ^{eff} is the effective ionic conductivity, φ_e is the electrolyte potential, κ_d^{eff} is the effective diffusion coefficient, and C_e is the concentration of species in electrolyte. Each region of the battery also has initial conditions for the potential in the electrolyte. There are Neumann boundary conditions such as zero flux at the electrode/current collector boundaries and continuity on the internal boundaries of the interfaces of the negative separator, and positive regions. There are also Dirichlet boundary conditions on the internal boundaries of the interfaces to make the potentials equal at the boundaries. For a one dimensional domain the conditions are shown as

$$\begin{aligned}
& -\left(\kappa^{eff}\frac{\partial\varphi_e}{\partial x} + \kappa_d^{eff}\frac{\partial C_e}{C_e}\right)\Bigg|_{x=0} = 0 \\
& -\left(\kappa^{eff}\frac{\partial\varphi_e}{\partial x} + \kappa_d^{eff}\frac{\partial C_e}{C_e}\right)\Bigg|_{x=L_{neg}^-} = -\left(\kappa^{eff}\frac{\partial\varphi_e}{\partial x} + \kappa_d^{eff}\frac{\partial C_e}{C_e}\right)\Bigg|_{x=L_{neg}^+} \\
& -\left(\kappa^{eff}\frac{\partial\varphi_e}{\partial x} + \kappa_d^{eff}\frac{\partial C_e}{C_e}\right)\Bigg|_{x=(L_{neg}^+, L_{sep})^-} = -\left(\kappa^{eff}\frac{\partial\varphi_e}{\partial x} + \kappa_d^{eff}\frac{\partial C_e}{C_e}\right)\Bigg|_{x=(L_{neg}^+, L_{sep})^+} \\
& -\left(\kappa^{eff}\frac{\partial\varphi_e}{\partial x} + \kappa_d^{eff}\frac{\partial C_e}{C_e}\right)\Bigg|_{x=L_{neg}^+ + L_{sep} + L_{pos}} = 0 \\
& \varphi_e(L_{neg}^-, t) = \varphi_e(L_{neg}^+, t) \\
& \varphi_e((L_{neg} + L_{sep})^-, t) = \varphi_e((L_{neg} + L_{sep})^+, t) \\
& \varphi_e(x, 0) = \varphi_e^{init}(x)
\end{aligned} \tag{2.8}$$

2.1.6 Conservation of Charge in Solid Phase

Conservation of charge in the solid phase is similar to equation (2.2). The partial differential equation for the solid phase in the negative and positive electrodes is

$$j_{li} = \nabla(\sigma_{eff}\nabla\varphi_s) \tag{2.9}$$

where j_{li} is the pore-wall flux across the interface, σ_{eff} is the effective electrical conductivity, and φ_s is the solid potential. Each region of the battery also has initial conditions for the potential in the solid phase. There are Neumann boundary conditions such as zero flux at the electrode/separator boundaries and an applied current density at the electrode/current collector boundaries. There is also a Dirichlet boundary condition on the negative electrode/current collector grounding the potential at that point. For a one dimensional domain conditions are shown below as

$$\begin{aligned}
-\sigma_{eff} \frac{\partial \varphi_s}{\partial x} \Big|_{x=0} &= 0 \\
-\sigma_{eff} \frac{\partial \varphi_s}{\partial x} \Big|_{x=L_{neg}} &= 0 \\
-\sigma_{eff} \frac{\partial \varphi_s}{\partial x} \Big|_{x=L_{neg}+L_{sep}} &= 0 \\
-\sigma_{eff} \frac{\partial \varphi_s}{\partial x} \Big|_{x=L_{neg}+L_{sep}+L_{pos}} &= -I_{app} \\
\varphi_s(x, 0) &= \varphi_s^{init}(x) \\
\varphi_s(0, t) &= 0
\end{aligned} \tag{2.10}$$

2.1.7 Butler-Volmer Kinetic Equation

Connecting all four of the previous partial differential equations is the expression for the pore wall flux across the interface. This equation is shown below as

$$j_{li} = a_s i_o \left[e^{\frac{\alpha_a F}{RT} (\varphi_s - \varphi_e - U)} - e^{-\frac{\alpha_c F}{RT} (\varphi_s - \varphi_e - U)} \right] \tag{2.11}$$

where j_{li} is the pore wall flux across the interface, a_s is the surface area to volume ratio, $i_o = F k_o C_e^{\alpha_a} (C_{s,max} - C_{s,surface})^{\alpha_a} C_{s,surface}^{\alpha_c}$, F is Faraday's constant, k_o is the kinetic

rate constant, C_e is the concentration in electrolyte, α_a is the anodic transfer coefficient, $C_{s,max}$ is the maximum concentration in the solid phase, $C_{s,surface}$ is the concentration at the surface in the solid phase, α_c is the cathodic transfer coefficient, R is the universal gas constant, T is the temperature, φ_s is the potential in the solid phase, φ_e is the potential in the electrolyte phase, and U is the equilibrium voltage.

Physics based modeling was used in [10] to model a $LiFePO_4/Li$ half cell. Verification of the model was done through an impedance spectroscopy test. This modeling technique was also used to develop a control-oriented fully observable/fully controllable state variable model from an impedance representation of electrochemical kinetic, species and charge conservation equations governing discharge/charge behaviors of a Li-ion cell [11].

Being a physics based model means that other physics can be added to it to make it a multiphysics model. Some industries are interested in the thermal properties of lithium batteries As shown in [12] the thermal effects on the currents, voltages, and concentrations can be seen. A detailed mathematical of the transport theory considering thermal effects was shown in [13].

2.2 Equivalent Circuit Model

An equivalent circuit model takes the overall characteristics of the lithium ion battery and estimates the output using dependent and independent current and voltage sources, capacitances, resistances, and inductances.

In [10] they mentioned that most battery management systems utilize ECM to protect the battery, predict, vehicle range, and update the range prediction depending on the driving conditions. They also mentioned that ECM's are commonly derived from

impedance spectroscopy.

In [14] the physics based model is used as the foundation of the equivalent circuit model. First using the Laplace transform of the solid phase concentration given in (2.5) and the Laplace transform of the current density given in (2.9) to produce the equation shown below

$$\frac{C_s(s)}{J(s)} = \frac{R_s}{FD_s} \left(\frac{\tanh(R_S \sqrt{\frac{s}{D_s}})}{\tanh(R_S \sqrt{\frac{s}{D_s}}) - R_s \sqrt{\frac{s}{D_s}}} \right) \quad (2.12)$$

Then the Laplace transform of the relationship between the intercalation current density and the overpotential shown below yields

$$N(s) = \frac{RT}{Fi_0(\alpha_a + \alpha_c)} J(s) \quad (2.13)$$

The Laplace transform of the electrolyte potential given in (2.7) is then calculated and is shown below

$$\tilde{\Phi}_e(L, s) = \frac{2RT(1 - t_+^0)}{C_{e,o}F} (C_e(L, s) - C_e(0, s)) - \frac{I(s)}{2A} \left(\frac{\delta}{\kappa^{eff}} + \frac{2\delta_{sep}}{\kappa_{sep}^{eff}} + \frac{\delta_+}{\kappa_+^{eff}} \right) \quad (2.14)$$

The internal resistance of the battery is estimated using the relationship shown below

$$V_f(s) = R_f I(s) \quad (2.15)$$

With equations (2.12 - 2.15) a terminal voltage can be derived and this relationship results in

$$V_{cell}(s) = \left(U_p \left(\frac{C_{s,pos}(s)}{c_{s,p,max}} \right) - U_n \left(\frac{C_{s,neg}(s)}{c_{s,n,max}} \right) \right) - (N_+(s) + N_-(s)) - (\Phi_{e,+}(s) - \Phi_{e,-}(s)) - R_f I(s) \quad (2.16)$$

Then a 2nd order Thevinin model was created assuming that the diffusion and migration at the electrodes are assumed to be realized by paralleled resistance and capacitance parts respectively, and an added resistance to compensate the changes of the electrolyte. The equivalent model produced from this derivation is shown below in Figure 2.1.

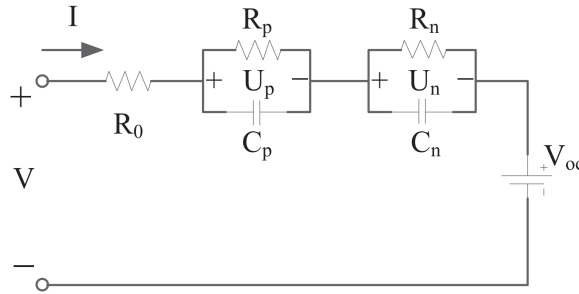


Figure 2.1 Equivalent circuit model.

Source: [4]

To determine the values of R_p , C_p , R_n , C_n , and R_0 the most commonly used method is the Recursive Least Square (RLS) method which fits the parameters to some measured data of the input current and output voltage. Instead electrochemical equation (2.16) is used with the equivalent circuit model shown in Figure 2.1 to improve on the estimation of the resistances and capacitances. In this proposed method is an improvement on the traditional method of RLS as shown below in Figure 2.2.

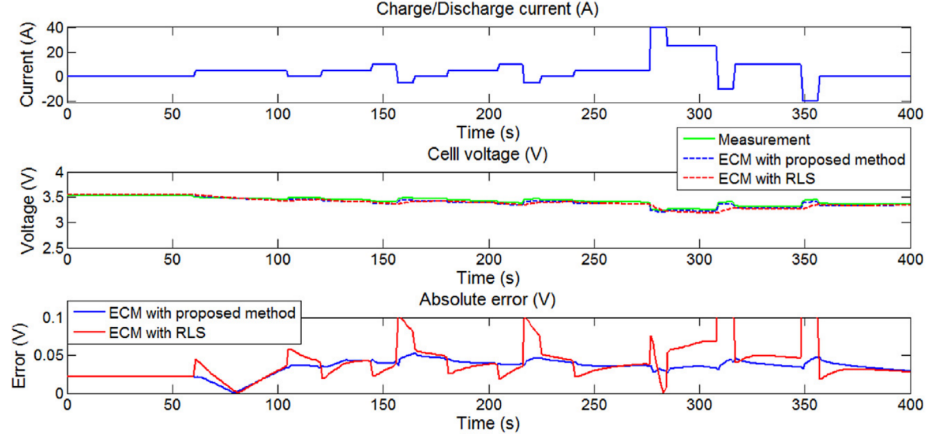


Figure 2.2 ECM simulation.

Source: [4]

2.3 Magnetic Field Effect

In [15] the magnetic field effect on a flowing electrolyte was studied extensively. They proposed that as a consequence of the Lorentz forces acting on the charge components of the electrolyte phase, a potential difference is induced in the electrolyte phase between two titanium electrode. The induced potential difference would be described as shown below

$$\Delta\phi_{MAG} = 2Bav_m \quad (2.17)$$

where $\Delta\phi_{MAG}$ is the induced potential, a is the inner radius of the pipe, v_m is the average flow velocity, and B is the applied magnetic flux density. Coupling of the magnetic field into the model was done through the method employed by [16]. In the absence of a magnetic field Ohm's Law gives the current density, $J = \sigma E$. Considering the Hall Effect, the modified expression for a general current density would be what is shown below

$$\bar{\mathbf{J}} = \sigma \bar{\mathbf{E}} + \frac{\sigma^2}{C_l F} (\bar{\mathbf{B}} \times \bar{\mathbf{E}}) \quad (2.18)$$

where $\bar{\mathbf{J}}$ is the current density, σ is the conductivity, $\bar{\mathbf{E}}$ is the electric field intensity, C_l is the concentration in electrolyte, F is Faraday's constant, and $\bar{\mathbf{B}}$ is the impressed (external) magnetic flux density. This modified current density equation was then inserted into the previously defined equations (2.7) and (2.9). The modified current density for the electrolyte is shown below

$$-j_{li} = \nabla \left(\kappa^{eff} \nabla \varphi_e + \frac{(\kappa^{eff})^2}{C_e F} (\bar{\mathbf{B}} \times \nabla \varphi_e) + \kappa_d^{eff} \nabla \frac{\nabla C_e}{C_e} \right) \quad (2.19)$$

where j_{li} is the pore-wall flux across the interface, κ_{eff} is the effective ionic conductivity, C_e is the concentration of species in electrolyte, F is Faraday's constant, $\bar{\mathbf{B}}$ is the magnetic flux density, φ_e is the electrolyte potential, and κ_d^{eff} is the effective diffusion coefficient.

The modified current density for the solid phase is shown below

$$j_{li} = \nabla (\sigma_{eff} \nabla \varphi_s + \frac{\sigma_{eff}^2}{C_e F} (\bar{\mathbf{B}} \times \nabla \varphi_s)) \quad (2.20)$$

where j_{li} is the pore-wall flux across the interface, σ_{eff} is the effective electrical conductivity, φ_s is the solid potential, C_e is the concentration of species in electrolyte, F is Faraday's constant, $\bar{\mathbf{B}}$ is the magnetic flux density.

At least a two dimensional domain is needed to implement these equations. The same authors of [16] showed a similar model in [17]. A similar phenomenon is used in

detecting structural changes in electrode materials known as nuclear magnetic resonance (NMR). This process provides information on different structural processes that can occur and on the mobility of the various species [18]. The magnetic field effect on lithium batteries in electric vehicles was studied in [19]. Through the use of equivalent circuit models (ECM's) they estimate the cross-coupling of the power inverters and converters to the battery system. Mitigation of these effects is done through common mode noise filtering, differential mode noise filtering, EMI suppression filters, and electromagnetic shielding [20].

Magnetic fields generated from lithium batteries themselves are also studied in [21]. Through the position of the tabs that come out of the batteries, they were able to see an effect from the fields that were generated from the batteries. Their motivation for the study was to see the effect in the context of the power drawn from the battery in cellphones under traditional protocols such as the global system for mobile communications (GSM) and code division multiple access (CDMA).

The effect of magnetic fields was also studied in [23] in the battery management systems (BMS) for lithium-ion batteries. They discussed the different ways that electromagnetic interference (EMI) affects the BMS for the lithium ion battery packs.

CHAPTER 3

RESEARCH

3.1 COMSOL Lithium Battery Interface

To compare the one dimensional domain to be created an understanding of COMSOL's existing lithium-ion battery interface is needed. There are many subtleties and nuisances that are implemented in the battery interface that need to be transferred over to the proposed model. The lithium-ion battery interface solves for the current balance in the electrolyte, the current balances in the electrodes, the mass balance for the lithium salt, and the mass balance of lithium in the batteries. The physics interface solves for five dependent variables; ϕ_s the electric potential, ϕ_l the electrolyte potential, $\Delta\phi_{s, film}$ the potential losses due to a resistive film on the electrode particles, c_s the concentration of lithium in the electrode particles, and c_l the electrolyte salt concentration.

The domain equations in the electrolyte are the conservation of current and the mass balance for the salt shown in equations (3.1) and (3.2)

$$i_{tot} + Q_l = \nabla \cdot \left(-\sigma_l \nabla \phi_l + \frac{2\sigma_l RT}{F} \left(1 + \frac{\partial \ln f}{\partial \ln c_l} \right) (1 - t_+) \Delta \ln c_l \right) \quad (3.1)$$

where σ_l is the electrolyte conductivity, f is the activity coefficient, t_+ is the transport number for Li^+ , i_{tot} is the sum of all electrochemical current sources, Q_l is the arbitrary electrolyte current and

$$\epsilon_l \frac{\delta c_l}{\delta t} \nabla \cdot (-\epsilon_l D_l \nabla c_l) = R_l - \left(\frac{i_{tot} + Q_l}{F} \right) t_+ \quad (3.2)$$

where ϵ_l is the electrolyte volume fraction, D_l is the electrolyte salt diffusivity, R_L is the total Li^+ source term in the electrolyte. In the electrode, the current density, i_s is shown below

$$i_s = -\sigma_s \nabla \phi_s \quad (3.3)$$

where σ_s is the electrical conductivity. The domain equation for the electrode is the conservation of current shown below

$$\nabla \cdot i_s = -i_{tot} + Q_s \quad (3.4)$$

where Q_s is the arbitrary current source term. The electrochemical reactions in the physics interface are assumed to be insertion reactions occurring at the surface of small solid spherical particles of radius r_p in the electrodes. The insertion reaction is shown below



where Θ_s is the free reaction site, $Li\Theta_s$ is the occupied reaction site at the solid particle surface. The concentration of Θ_s does not have to be solved for since the total concentration of reaction sites, $c_{s,max}$ is assumed to be constant as

$$c_{\Theta_s} = c_{s,max} - c_s \quad (3.6)$$

The state of charge variable is related to the max concentration and the current concentration. This relationship is shown below as

$$SOC = \frac{c_s}{c_{s,max}} \quad (3.7)$$

The electrode reaction occurs on the particle surface and lithium diffuses to and from the surface in the particles. The mass balance of lithium is shown below

$$\frac{\delta c_s}{\delta t} = -\nabla \cdot (-D_s \nabla c_s) \quad (3.8)$$

where c_s is the concentration of Li in the solid phase. This equation is solved locally by the physics interface in a 1D pseudo dimension, with the solid phase concentrations at the nodal points for the element discretization of the particle as the independent variables. The gradient is calculated in cartesian, cylindrical, or spherical coordinates, depending on if the particles are assumed to be best described as flakes, rods, or spheres, respectively. The boundary conditions are shown below

$$\begin{aligned} \frac{\delta c_s}{\delta r} &= 0 \Big|_{r=0} \\ -D_s \frac{\delta c_s}{\delta r} &= -R_{Li\Theta} \Big|_{r=r_p} \end{aligned} \quad (3.9)$$

where $R_{Li\Theta}$ is the molar flux of lithium at the particle surface. The stoichiometric notations used in the physics interface are according to the general electrochemical reaction as

$$\sum_{ox} v_{ox} S_{ox} + ne^{-1} \Leftrightarrow \sum_{red} v_{red} S_{red} \quad (3.10)$$

where v_{ox} is positive for products and v_{red} is negative for reactants. The number of electrons, n , in the electrode reaction can be calculated as

$$n = - \sum_i z_i v_i \quad (3.11)$$

where z_i is the charge of the species i . According to these relations, the lithium insertion reaction has the following stoichiometric coefficients as shown below

$$\begin{aligned} v_{Li^+} &= -1 \\ v_{an^-} &= 0 \\ v_{Li\Theta_s} &= 1 \end{aligned} \quad (3.12)$$

In the porous electrode, i_{tot} , denotes the sum of all charge transfer current density contributions according to what is shown below

$$i_{tot} = \sum A_{v,m} i_{loc,m} \quad (3.13)$$

where A_v is the specific surface. The source term in the mass balance is calculated as shown below

$$R_{l,p} = - \sum_m A_{v,m} \frac{v_{Li^+,m} i_{loc,m}}{n_m F} \quad (3.14)$$

At the surface of the solid particles following relationship applies as seen below

$$R_{Li\Theta} = - \sum_m \frac{v_{Li^+,m} \dot{i}_{loc,m}}{n_m F} \times \frac{A_{v,m}}{\frac{N_{shape} \epsilon_s}{r_p}} \quad (3.15)$$

The last factor in the previous equation is a scaling factor accounting for differences between the surface area ($A_{v,m}$) used to calculate the volumetric current density, and the surface area of the particles in the solid lithium diffusion model. N_{shape} is 1 for cartesian, 2 for cylindrical, and 3 for spherical coordinates.

If the solid phase diffusion coefficient is very large or if the spatial concentration gradients in the particle can be neglected, the solid phase concentration evolution in time can be calculated as

$$\frac{\delta \epsilon_s c_s}{\delta t} = R_{v\Theta} \quad (3.16)$$

The molar source $R_{v\Theta}$ at the positive and negative electrodes is given as

$$R_{v\Theta} = - \sum_m \frac{v_{Li\Theta,m} A_{v,m} \dot{i}_{loc,m}}{n_m F} \quad (3.17)$$

A resistive film (also called solid-electrolyte interface, SEI) might form on the solid particles resulting in additional potential losses in the electrodes. To model a film resistance, an extra solution variable for the potential variation over the film, $\Delta \phi_{s,film}$, is introduced in the physics interface. This relationship is shown below

$$\Delta\phi_{s,film} = i_{tot}R_{film} \quad (3.18)$$

where R_{film} is a generalized film resistance. The activation overpotentials, η_m , for all electrode reactions in the electrode then receives an extra potential contribution shown below

$$\eta_m = \phi_s - \Delta\phi_{s,film} - \phi_l - E_{eq,m} \quad (3.19)$$

3.2 COMSOL 1D Modeling

Another area of interest, which is the area concerned with this research, is that of identifying the effect of magnetic fields on batteries. The physics based model that was derived in Section 2.1 was utilized in COMSOL Multiphysics 5.4. A one dimensional domain was created to represent a negative electrode, a separator, and and a positive electrode. Then a two dimensional domain was created to represent the diffusion in the solid negative electrode. Followed by an additional two dimensional domain to represent the diffusion in the solid positive electrode. This was created to provide verification on a two dimensional model that could experience the effects of a magnetic field.

3.2.1 Model Definition

Starting with the one dimensional domain are three line segments connected together. The first line segment represents the negative electrode, the second line segment represents the separator, and the final line segment represents the positive electrode. In the negative electrode there are three partial differential equations; one for the charge balance in the

solid negative electrode, one for the charge balance in the electrolyte in that region, and one for the material balance in the electrolyte in that region. In the separator region there are two partial differential equations; one for the charge balance in the electrolyte in that region and one for the material balance in the electrolyte in that region. In the positive electrode there are three partial differential equations; one for the charge balance in the solid positive electrode, one for the charge balance in the electrolyte in that region, and one for the material balance in the electrolyte in that region.

For the negative electrode there is a two dimensional domain representing the diffusion. And for the positive electrode there is an additional two dimensional domain representing the diffusion. Shown below in Figure 3.1 is the model tree showing each aspect of the model.

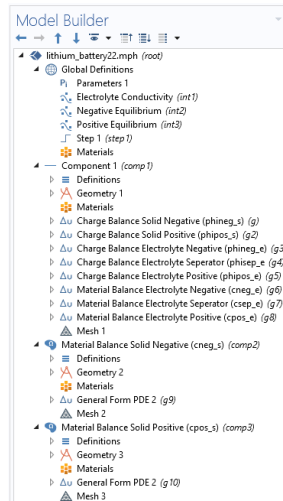


Figure 3.1 1D model, model tree.

Shown below in Figure 3.2 is a diagram of where each variable is solved and the three domains.

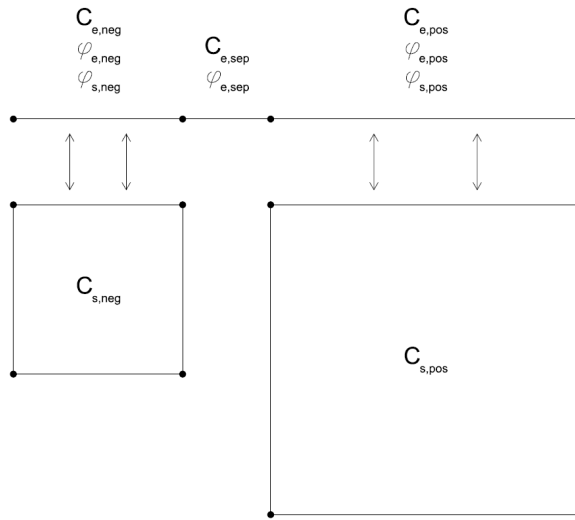


Figure 3.2 1D model, model diagram.

In the above figure the boundary on top of $C_{s,neg}$ is extruded to the region containing $C_{e,neg}$, $\varphi_{e,neg}$, and $\varphi_{s,neg}$. Similarly, $C_{s,pos}$ is extruded to the region containing $C_{e,pos}$, $\varphi_{e,pos}$, and $\varphi_{s,pos}$.

3.2.2 Global Definitions

Within the three previously described domains are common functions and parameters that are used in each. The first function is the electrolyte conductivity from [22] which is a function of the concentration of electrolyte at every point. This coefficient is used in the effective ionic conductivity and effective diffusion coefficients described in equation (2.7). Shown below in Figure 3.3 is the input/output relation for the electrolyte conductivity.

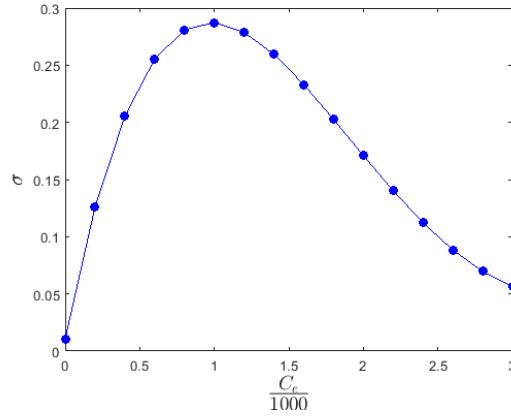


Figure 3.3 Electrolyte conductivity.

This electrolyte conductivity is used within the model by having its input be the electrolyte concentration divided by 1000. This relationship is shown below

$$\kappa(x) = u\left(\frac{C_e}{1000}\right) \quad (3.20)$$

where κ is the electrolyte conductivity, u is the graph shown in Figure 3.3, and C_e is the concentration in the electrolyte. From Figure 3.3 the electrolyte conductivity ranges from 0.02 to 0.28. The input concentrations range from 0 to 3000. The second function is that of the negative equilibrium voltage from [22] in the negative electrode. This equilibrium voltage is used in the Butler-Volmer equation shown in Equation 2.11. Shown below in Figure 3.4 is the relation for the negative equilibrium voltage.

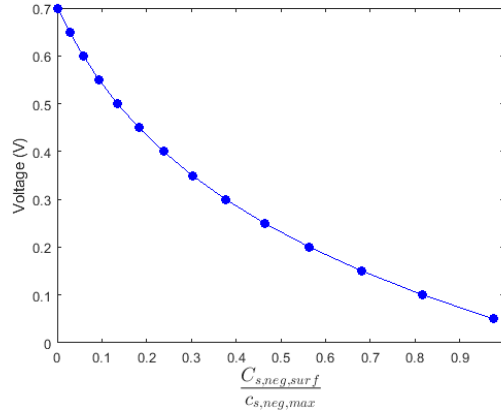


Figure 3.4 Negative equilibrium voltage.

This negative equilibrium voltage is used within the model by having its input be the concentration of the solid phase in the negative electrode at the surface divided by the max concentration allowed in the negative electrode. This relationship is shown below

$$U_{neg}(x) = u\left(\frac{C_{s,neg,surf}}{C_{s,neg,max}}\right) \quad (3.21)$$

where U_{neg} is the equilibrium voltage in the negative electrode, u is the relationship shown in Figure 3.4, $C_{s,neg,surf}$ is the concentration in the solid phase in the negative electrode at the surface, and $C_{s,neg,max}$ is the maximum concentration in the solid phase in the negative electrode. From Figure 3.4 the negative equilibrium voltage ranges from 0 to 1. The input concentrations range from a ratio of 0 and a ratio of 0.7.

The third function is that of the positive equilibrium voltage from [22] in the positive electrode. This equilibrium voltage is used in the Butler-Volmer equation shown in equation (2.11). Shown below in Figure 3.5 is the relation for the positive equilibrium voltage.

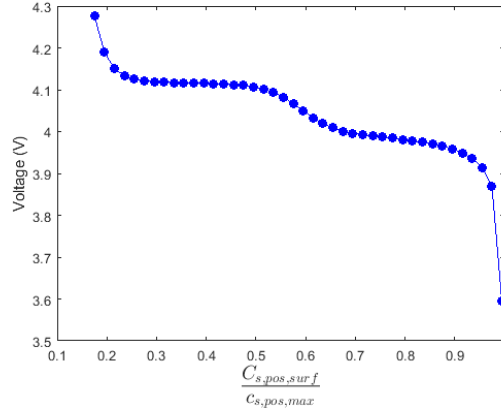


Figure 3.5 Positive equilibrium voltage.

The positive equilibrium voltage is used within the model by having its input be the concentration of the solid phase in the positive electrode at the surface divided by the max concentration allowed in the positive electrode. This relationship is shown below

$$U_{pos}(x) = u\left(\frac{C_{s,pos,surf}}{C_{s,pos,max}}\right) \quad (3.22)$$

where U_{pos} is the equilibrium voltage in the negative electrode, u is the relationship shown in Figure 3.5, $C_{s,pos,surf}$ is the concentration in the solid phase in the negative electrode at the surface, and $C_{s,pos,max}$ is the maximum concentration in the solid phase in the negative electrode. From Figure 3.5 the positive equilibrium voltage ranges from 3.6 to 4.3. The input concentrations range from a ratio of 0.2 to a ratio of 1.

The fourth function is that of the pore-wall flux across the interface for the negative electrode. This equation is shown below

$$j_{li,neg} = a_{s,neg} i_{o,neg} \left[e^{\frac{\alpha_a F}{RT} (\varphi_{s,neg} - \varphi_{e,neg} - U_{neg})} - e^{-\frac{\alpha_c F}{RT} (\varphi_{s,neg} - \varphi_{e,neg} - U_{neg})} \right] \quad (3.23)$$

where $j_{li,neg}$ is the pore-wall flux across the interface in the negative electrode, $a_{s,neg}$ is the surface to volume ratio in the negative electrode, $i_{o,neg} = Fk_{o,neg}C_{e,neg}^{\alpha_a}(C_{s,neg,max} - C_{s,neg,surf})^{\alpha_a}C_{s,neg,surf}^{\alpha_c}$, F is Faraday's constant, $k_{o,neg}$ is the kinetic rate constant in the negative electrode, $C_{e,neg}$ is the concentration in the electrolyte in the negative electrode, α_a is the anodic transfer coefficient, $C_{s,neg,max}$ is the maximum concentration in the negative solid electrode, $C_{s,neg,surf}$ is the maximum concentration in the negative solid electrode, α_c is the cathodic transfer coefficient, R is the universal gas constant, T is the temperature, $\varphi_{s,neg}$ is the potential in the solid negative electrode, $\varphi_{e,neg}$ is the potential in the electrolyte in the negative electrode, and U_{neg} is the equilibrium in the negative electrode. The fifth function is that of the pore-wall flux across the interface for the positive electrode. This equation is shown below

$$j_{li,pos} = a_{s,pos}i_{o,pos} \left[e^{\frac{\alpha_a F}{RT}(\varphi_{s,pos} - \varphi_{e,pos} - U_{pos})} - e^{-\frac{\alpha_c F}{RT}(\varphi_{s,pos} - \varphi_{e,pos} - U_{pos})} \right] \quad (3.24)$$

where $j_{li,pos}$ is the pore-wall flux across the interface in the positive electrode, $a_{s,neg}$ is the surface to volume ratio in the positive electrode, $i_{o,pos} = Fk_{o,pos}C_{e,pos}^{\alpha_a}(C_{s,pos,max} - C_{s,pos,surf})^{\alpha_a}C_{s,pos,surf}^{\alpha_c}$, F is Faraday's constant, $k_{o,pos}$ is the kinetic rate constant in the positive electrode, $C_{e,pos}$ is the concentration in the electrolyte in the positive electrode, α_a is the anodic transfer coefficient, $C_{s,pos,max}$ is the maximum concentration in the positive solid electrode, $C_{s,pos,surf}$ is the maximum concentration in the positive solid electrode, α_c is the cathodic transfer coefficient, R is the universal gas constant, T is the temperature, $\varphi_{s,pos}$ is the potential in the solid positive electrode, $\varphi_{e,pos}$ is the potential in the electrolyte in the positive electrode, and U_{pos} is the equilibrium in the positive electrode. The sixth

function is a step function. This function is preprogrammed in COMSOL. Shown below in Figure 3.6 is a plot of the step function.

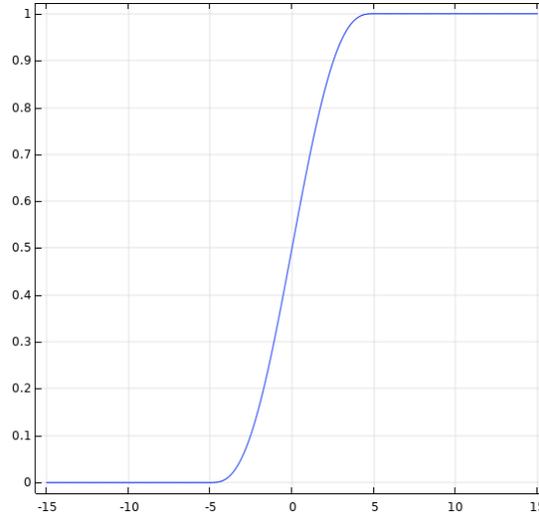


Figure 3.6 Step function.

The user has control over the size of the transition zone. In this case it was set to 10. To set the step function up properly a Variables subnode needs to be created in the Definitions subnode for Component 1. The table needed for the variables subnode is shown below in Table 3.1.

Table 3.1 Variables Subnode

Name	Expression
I_{app}	$i_{app} * dis_{on} - i_{app} * ch_{on}$
dis_{on}	$step1\left(\left(t_{disch} - t\right)\left[\frac{1}{s}\right]\right)$
ch_{on}	$step1\left(\left(t - t_{disch} - t_{ocp}\right)\left[\frac{1}{s}\right]\right) \times step1\left(\left(t_{charge} + t_{discharge} + t_{ocp} - t\right)\left[\frac{1}{s}\right]\right)$

To set up the model properly many constants and parameters were taken from [22]

and COMSOL's pre-built one-dimensional model. Some of the parameters are fixed and well defined. However some are not and it becomes difficult to obtain accurate simulations that can match experimental measurements based on constructed batteries. The constants used for the negative electrode, the separator, and the positive electrode are shown on the next page in Table 3.2. For parameters taken from [22] a ¹ is used and for parameters taken from COMSOL a ² is used. Some values are not explicitly defined, but are derived from other values. Shown below is the expression for the polymer phase volume fraction

$$\epsilon_{p,i} = 1 - \epsilon_{e,i} - \epsilon_{f,i} \quad (3.25)$$

where i is the negative or positive electrode, ϵ_p is the polymer phase volume fraction, ϵ_e is the electrolyte phase volume fraction, and ϵ_f is the conductive filler phase volume fraction. Another derived value in Table 3.2 is that of the active interfacial surface area for the negative and positive electrodes. Shown below is the expression for the active interfacial surface area

$$a_{i,s} = \frac{3\epsilon_{p,i}}{R_{s,i}} \quad (3.26)$$

where a is the active interfacial surface area, i is the positive or negative electrode, ϵ_p is the polymer phase volume fraction, and R_s is the particle radius.

Table 3.2 Constants and Parameters

Name	Value	Description
$R_{s,neg}$	12.5E-6	Particle Radius Negative ¹
$R_{s,pos}$	8E-6	Particle Radius Positive ¹
L_{neg}	100E-6	Negative Electrode Length ¹
L_{sep}	52E-6	Separator Length ¹
L_{pos}	183E-6	Positive Electrode Length ²
F	96485	Faraday's Constant
α_a	0.5	Anodic Charge Transfer Coefficient ²
α_c	0.5	Cathodic Charge Transfer Coefficient ²
t_+	0.363	Transfer Coefficient ²
σ_{neg}	100	Electrical Conductivity in Negative Electrode ¹
σ_{pos}	3.8	Electrical Conductivity in Positive Electrode ¹
i_{app}	17.5	Applied Current Density ¹
brugg	3.3	Bruggeman Correction Coefficient ¹
$D_{s,neg}$	3.9E-14	Diffusion Coefficient in Solid Negative Electrode ¹
$D_{s,pos}$	1E-13	Diffusion Coefficient in Solid Positive Electrode ¹
$D_{e,neg}$	7.5E-11	Diffusion Coefficient in Electrolyte Negative Electrode ²
$D_{e,sep}$	7.5E-11	Diffusion Coefficient in Electrolyte Separator Electrode ²
$D_{e,pos}$	7.5E-11	Diffusion Coefficient in Electrolyte Positive Electrode ²
$\epsilon_{e,neg}$	0.503	Negative Electrolyte Phase Volume Fraction ²
$\epsilon_{e,sep}$	1	Separator Electrolyte Phase Volume Fraction ²
$\epsilon_{e,pos}$	0.63	Positive Electrolyte Phase Volume Fraction ²
$\epsilon_{f,neg}$	0.026	Negative Conductive Filler Volume Fraction ¹
$\epsilon_{f,pos}$	0.073	Positive Conductive Filler Volume Fraction ¹
$\epsilon_{p,neg}$	0.471	Negative Polymer Phase Volume Fraction
$\epsilon_{p,pos}$	0.297	Positive Polymer Phase Volume Fraction
$a_{neg,s}$	1.1304E5	Active Interfacial Negative Surface Area
$a_{pos,s}$	1.1138E5	Active Interfacial Positive Surface Area
$k_{neg,o}$	4.4E-10	Negative Kinetic Constant ²
$k_{pos,o}$	4.8E-10	Positive Kinetic Constant ²
$c_{s,neg,max}$	26390	Maximum Concentration in Negative Electrode ²
$c_{s,pos,max}$	22860	Maximum Concentration in Positive Electrode ²
R	8.314	Universal Gas Constant
T	298	Temperature
$c_{s0,neg}$	14870	Initial Positive Solid Electrode ¹
$c_{s0,pos}$	3900	Initial Negative Solid Electrode ¹
c_{l0}	2000	Initial Electrolyte Concentration ¹
$t_{discharge}$	2000	Discharge Duration ²
t_{ocp}	300	Open Circuit Duration ²
t_{charge}	2000	Charge Duration ²

With the above parameters in real-life batteries it is not realistic to determine these values. Knowing some of these parameters such as the initial concentrations, diffusion coefficients, volume fractions, and conductivity is impossible to determine.

3.2.3 Geometries and Meshes

Shown below in Figure 3.7 are the three regions for the one dimensional domain representing the negative electrode, separator, and positive electrode.

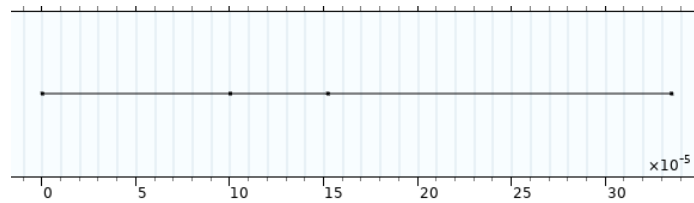


Figure 3.7 1D model, 1d domain.

The numbering convention for points on the domain is shown below in Figure 3.8.

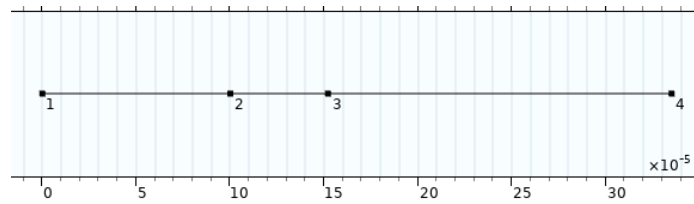


Figure 3.8 1D model, 1d points.

The distance between points 1 and 2 is L_{neg} , the distance between points 2 and 3 is L_{sep} , and the distance between points 3 and 4 is L_{pos} . Different differential equations apply to different regions of the geometry shown in Figure 3.7. Shown below in Figure 3.9 are the three regions for the negative electrode, separator, and positive electrode.

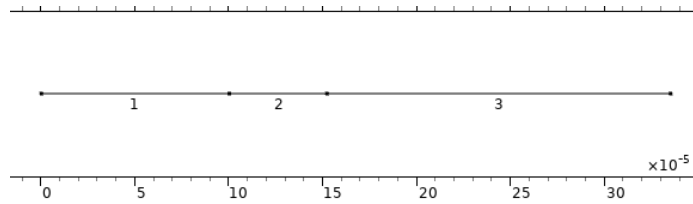


Figure 3.9 1D model, 1d domain regions.

Shown below in Figure 3.10 is the mesh used for the one dimensional domain.

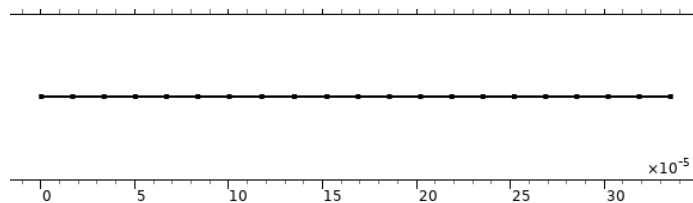


Figure 3.10 1D model, 1d domain mesh.

The mesh used for the domain utilized the pre-built defined Element Size of Fine which resulted in 20 domain elements. Shown below in Figure 3.11 is the two dimensional domain used separately for the material balance in the negative electrode solid phase. An exact copy of it was used for the material balance in the positive electrode solid phase.

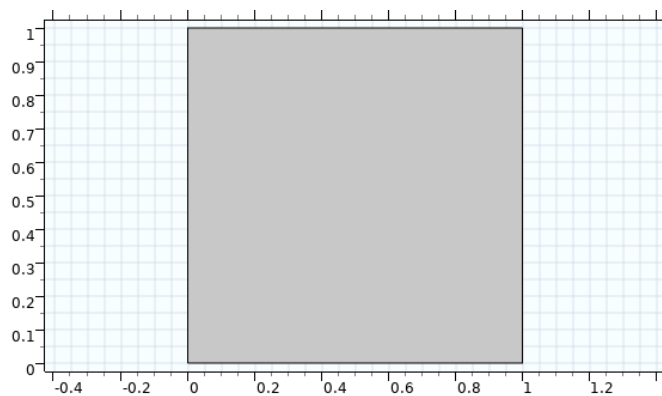


Figure 3.11 1D model, 2d domain.

To apply different fluxes on the boundaries of the domain, the numbering convention shown in Figure 3.12 was used.

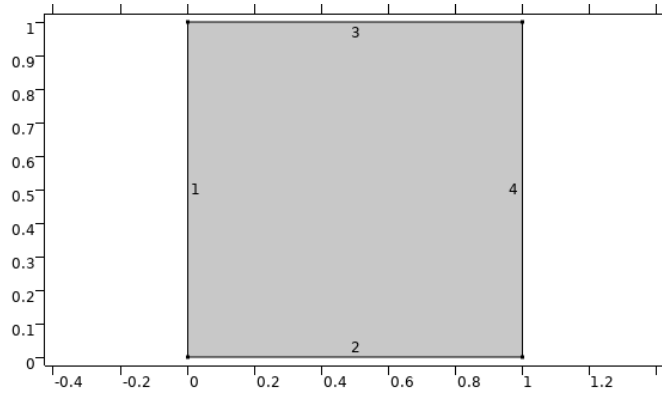


Figure 3.12 1D model, 2d domain boundaries.

A point along Boundary 3 represents the surface of a spherical particle at that point. A point along Boundary 2 represents the center of a spherical particle at that point. Shown below in Figure 3.13 is the mesh used for the two dimensional domain.

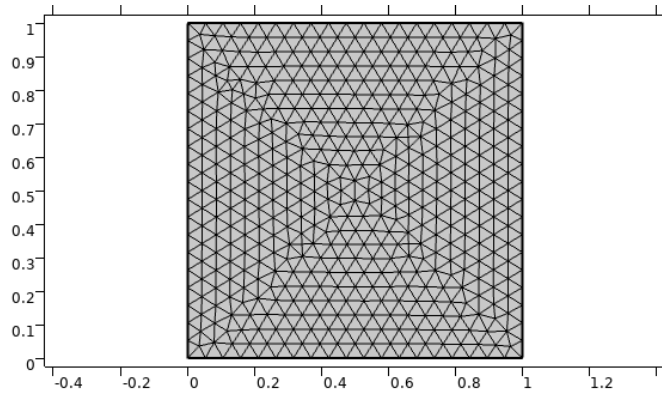


Figure 3.13 1D model, 2d domain mesh.

The mesh used for the domain utilized the pre-built defined Element Size of Fine which resulted in 928 domain elements and 76 boundary elements.

3.2.4 Charge Balance Solid Negative

The charge balance in the solid phase of the negative electrode (CBSN) was applied to region 1 shown below in Figure 3.14.

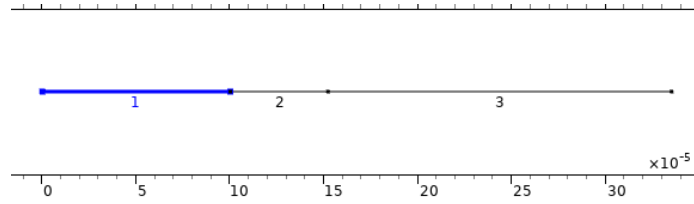


Figure 3.14 1D model, cbsn region.

The General Form PDE in the Mathematics-PDE Interfaces was used to implement the partial differential equation described in equation (2.9) to solve for $\varphi_{s,neg}$. The General Form PDE equation is shown below

$$f = e_a \frac{\partial^2 u}{\partial t^2} + d_a \frac{\partial u}{\partial t} + \nabla \cdot \Gamma \quad (3.27)$$

where f is the source term, e_a is the mass coefficient, u is the dependent variable, d_a is the damping or mass coefficient, $\nabla = \frac{\partial}{\partial x}$, and Γ is the conservative flux. Matching like coefficients between equations (2.9) and (3.27), results in the relations shown below in Table 3.3.

Table 3.3 1D Model, CBSN Parameters

General Form	Value
f	$\dot{I}l_{i,neg}$
e_a	0
d_a	0
Γ	$\sigma_{eff,neg} \frac{\partial}{\partial x} \varphi_{s,neg}$

The effective electrical conductivity used in the conservative flux in equation (3.27), $\sigma_{eff,neg}$, was set equal to σ_{neg} as in there was no Bruggeman correction used. Shown below is this relationship

$$\sigma_{eff,neg} = \sigma_{neg} \quad (3.28)$$

where $\sigma_{eff,neg}$ is the effective electrical conductivity, and σ_{neg} is the electrical conductivity. Within the General Form PDE interface an Initial Value subnode was created. Within this subnode, the region shown in Figure 3.14 was selected, and the initial value for $\varphi_{s,neg}$ was set to 0 as shown below

$$\varphi_{s,neg}(x, 0) = 0 \quad (3.29)$$

where $\varphi_{s,neg}$ is the potential in the solid negative electrode. Then within the interface a Dirichlet Boundary Condition subnode was created. The leftmost boundary shown in Figure 3.15 was selected and the value of $\varphi_{s,neg}$ was set to 0 as shown below

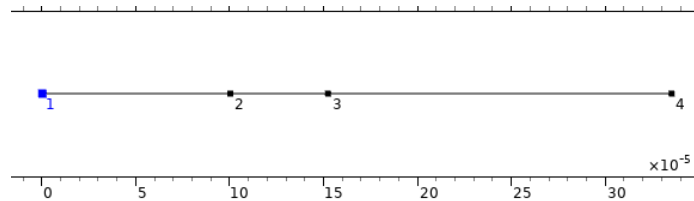


Figure 3.15 1D model, cbsn zero value.

$$\varphi_{s,neg}(0, t) = 0 \quad (3.30)$$

where $\varphi_{s,neg}$ is the potential in the solid negative electrode. Finally the flux at the boundary between the negative electrode and the separator shown in Figure 3.16 was set to 0. The equation used for the Zero Flux subnode is shown below

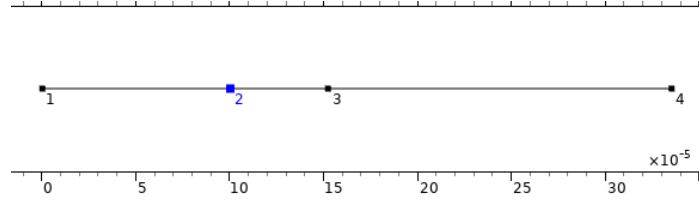


Figure 3.16 1d model, cbsn zero flux boundary.

$$-n \cdot \Gamma = 0 \quad (3.31)$$

where n is the normal vector and Γ is the conservative flux.

3.2.5 Charge Balance Solid Positive

The charge balance in the solid phase of the positive electrode (CBSP) was applied to region 3 shown below in Figure 3.17.

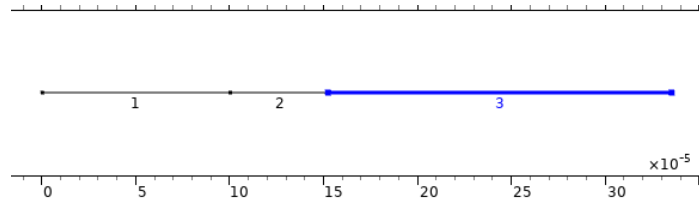


Figure 3.17 1D model, cbsp region.

The General Form PDE in the Mathematics-PDE Interfaces was used to implement the partial differential equation described in equation (2.9) to solve for $\varphi_{s,pos}$. The General Form PDE equation is shown below

$$f = e_a \frac{\partial^2 u}{\partial t^2} + d_a \frac{\partial u}{\partial t} + \nabla \cdot \Gamma \quad (3.32)$$

where f is the source term, e_a is the mass coefficient, u is the dependent variable, d_a is

the damping or mass coefficient, $\nabla = \frac{\partial}{\partial x}$, and Γ is the conservative flux. Matching like coefficients between equations (2.9) and (3.32), results in the relations shown below in Table 3.4.

Table 3.4 1D Model, CBSP Parameters

General Form	Value
\mathbf{f}	$j_{li,pos}$
e_a	0
d_a	0
Γ	$\sigma_{eff,pos} \frac{\partial}{\partial x} \varphi_{s,pos}$

The effective electrical conductivity used in the conservative flux in equation (3.32), $\sigma_{eff,pos}$, was set equal to σ_{pos} as in there was no Bruggeman correction used. Shown below is this relationship

$$\sigma_{eff,pos} = \sigma_{pos} \quad (3.33)$$

where $\sigma_{eff,pos}$ is the effective electrical conductivity and σ_{pos} is the electrical conductivity. Within the General Form PDE interface an Initial Value subnode was created. Within this subnode, the region shown in Figure 3.17 was selected, and the initial value for $\varphi_{s,pos}$ was set to the voltage difference between the equilibrium voltage at the positive electrode and the equilibrium voltage at the negative electrode at the initial concentrations in each respective electrode shown below

$$\varphi_{s,pos}(x, 0) = U_{pos} \left(\frac{c_{s0,pos}}{c_{s,pos,max}} \right) - U_{neg} \left(\frac{c_{s0,neg}}{c_{s,neg,max}} \right) \quad (3.34)$$

where $\varphi_{s,pos}$ is the potential in the solid positive electrode, U_{pos} is the positive equilibrium voltage, $c_{s0,pos}$ is the initial concentration in the solid positive electrode, $c_{s,pos,max}$ is the maximum concentration in the solid positive electrode, U_{neg} is the negative equilibrium voltage, $c_{s0,neg}$ is the initial concentration in the solid negative electrode, and $c_{s,neg,max}$ is the maximum concentration in the solid negative electrode. Next the flux at the boundary between the positive electrode and the separator as shown in Figure 3.18 was set to 0. The equation used for the Zero Flux subnode is shown below

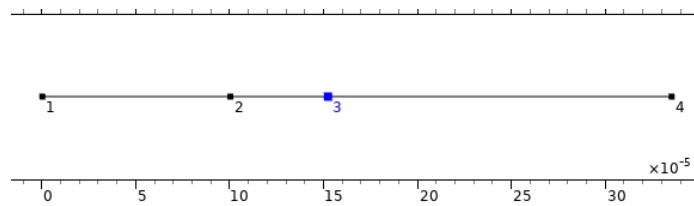


Figure 3.18 1D model, cbsp zero flux boundary.

$$-n \cdot \Gamma = 0 \quad (3.35)$$

where n is the normal vector and Γ is the conservative flux. Finally within the interface a Flux/Source subnode was created. The equation used for the Flux/Source subnode is shown below

$$-n \cdot \Gamma = g - qu \quad (3.36)$$

where n is the normal vector, Γ is the conservative flux, g is the boundary flux/source, q is the boundary absorption/impedance term, and u is the dependent variable. This flux is for the current density on the rightmost positive electrode boundary shown in Figure 3.19.

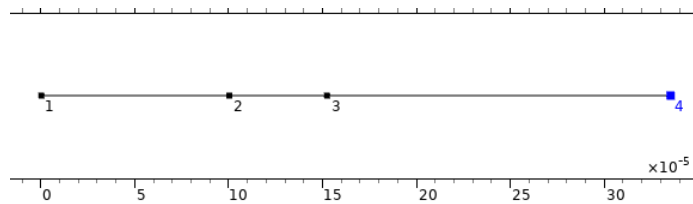


Figure 3.19 1D model, cbasp applied current boundary.

Matching like coefficients between equations (2.8) and (3.36), results in the relations shown below in Table 3.5. With the convention that the negative of the normal vector is pointing into the domain, a positive applied current means that the vector would be pointing into the domain and the current would be moving to the left.

Table 3.5 1D Model, CBSP Flux/Source

Flux/Source	Value
g	I_{app}
q	0

3.2.6 Charge Balance Electrolyte Negative

The charge balance in the electrolyte phase of the negative electrode (CBEN) was applied to region 1 shown below in Figure 3.20.

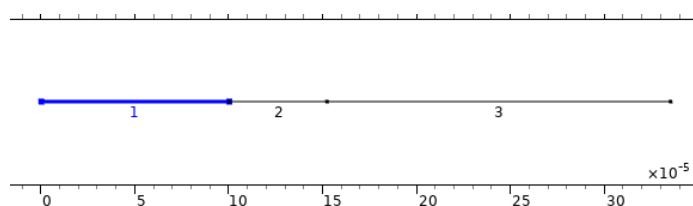


Figure 3.20 1D model, cben region.

The General Form PDE in the Mathematics-PDE Interfaces was used to implement the partial differential equation described in equation (2.7) to solve for $\varphi_{e,neg}$. The General Form PDE equation is shown below

$$f = e_a \frac{\partial^2 u}{\partial t^2} + d_a \frac{\partial u}{\partial t} + \nabla \cdot \Gamma \quad (3.37)$$

where f is the source term, e_a is the mass coefficient, u is the dependent variable, d_a is the damping or mass coefficient, $\nabla = \frac{\partial}{\partial x}$, and Γ is the conservative flux. Matching like coefficients between equations (2.7) and (3.37), results in the relations shown below in Table 3.6.

Table 3.6 1D Model, CBEN Parameters

General Form	Value
f	$-j_{i,neg}$
e_a	0
d_a	0
Γ	$\kappa^{eff,neg} \frac{\partial}{\partial x} \varphi_{e,neg} + \kappa_{d,neg}^{eff,neg} \frac{\partial}{\partial x} \frac{\frac{\partial C_{e,neg}}{\partial x}}{C_{e,neg}}$

The effective ionic conductivity used in the conservative flux in equation (3.37), $\kappa^{eff,neg}$, was set equal to $\kappa_{neg}(\epsilon_{e,neg})^{brugg}$ as in there is Bruggeman correction used. Shown below is this relationship

$$\kappa^{eff,neg} = \kappa_{neg}(\epsilon_{e,neg})^{brugg} \quad (3.38)$$

where $\kappa^{eff,neg}$ is the effective electrical ionic conductivity, κ_{neg} is the graph in Figure 3.3, $\epsilon_{e,neg}$ is the negative electrolyte phase volume fraction, and $brugg$ is the Bruggeman correction coefficient. The effective diffusion coefficient used in the conservative flux in Equation 3.37, $\kappa_{d,neg}^{eff,neg}$, was set equal to $\frac{2RT}{F}(t_+ - 1)\kappa_{neg}(\epsilon_{e,neg})^{brugg}$ as in there is Bruggeman correction used. Shown below is this relationship

$$\kappa_{d,neg}^{eff,neg} = \frac{2RT}{F}(t_+ - 1)\kappa_{neg}(\epsilon_{e,neg})^{brugg} \quad (3.39)$$

where $\kappa_{d,neg}^{eff,neg}$ is the effective diffusion coefficient, R is the universal gas constant, T is temperature, F is Faraday's constant, t_+ is the transference number, κ_{neg} is the graph in Figure 3.3, $\epsilon_{e,neg}$ is the negative electrolyte phase volume fraction, and $brugg$ is the bruggeman correction coefficient. Within the General Form PDE interface an Initial Value subnode was created. Within this subnode, the region shown in Figure 3.20 was selected, and the initial value for $\varphi_{e,neg}$ was set to $-U_{neg}$ shown below

$$\varphi_{e,neg}(x, 0) = -U_{neg} \left(\frac{c_{s0,neg}}{c_{s,neg,max}} \right) \quad (3.40)$$

where $\varphi_{s,neg}$ is the potential in the electrolyte in the negative electrode, U_{neg} is the negative equilibrium voltage, $c_{s0,neg}$ is the initial concentration in the solid negative electrode, and $c_{s,neg,max}$ is the maximum concentration in the solid negative electrode. Then within the interface a Dirichlet Boundary Condition subnode was created. The boundary between the negative electrode and the separator shown in Figure 3.21 was selected and the value of $\varphi_{e,neg}$ was set equal to $\varphi_{e,sep}$ as shown below to maintain continuity

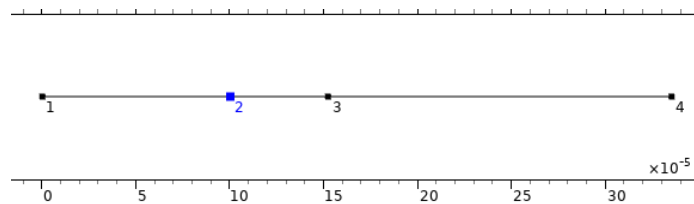


Figure 3.21 1D model, cben dirichlet/flux boundary.

$$\varphi_{e,neg}(L_{neg}, t) = \varphi_{e,sep}(L_{neg}, t) \quad (3.41)$$

where $\varphi_{e,neg}$ is the potential in the negative electrolyte and $\varphi_{e,sep}$ is the potential in the separator electrolyte. Next the flux at the leftmost boundary shown in Figure 3.22 was set to 0. The equation used for the Zero Flux subnode is shown below as

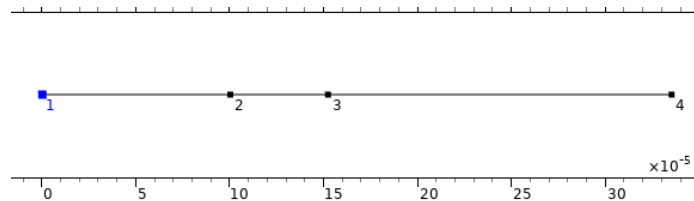


Figure 3.22 1D model, cben zero flux boundary.

$$-n \cdot \Gamma = 0 \quad (3.42)$$

where n is the normal vector and Γ is the conservative flux. Finally within the interface a Flux/Source subnode was created. The equation used for the Flux/Source subnode is shown below in Equation 3.43.

$$-n \cdot \Gamma = g - qu \quad (3.43)$$

where n is the normal vector, Γ is the conservative flux, g is the boundary flux/source, q is the boundary absorption/impedance term, and u is the dependent variable. This flux is for continuity between the negative electrode and separator at the boundary shown in Figure 3.21. Matching like coefficients between equations (2.8) and (3.43), results in the relations

shown below in Table 3.7. With the convention that the negative of the normal vector is pointing into the domain, a negative flux means that the vector would be pointing out of the domain and the potential would be moving to the right.

Table 3.7 1D Model, CBEN Flux/Source

Flux/Source	Value
g	$-\left(\kappa^{eff,sep} \frac{\partial}{\partial x} \varphi_{e,sep} + \kappa_{d,sep}^{eff} \frac{\partial}{\partial x} \frac{\partial C_{e,sep}}{C_{e,sep}} \right)$
q	0

3.2.7 Charge Balance Electrolyte Separator

The charge balance in the electrolyte phase of the separator (CBES) was applied to region 2 shown below in Figure 3.23.

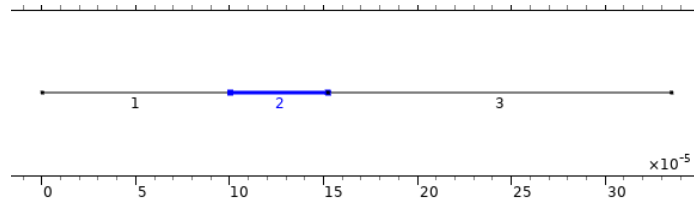


Figure 3.23 1D model, cbes region.

The General Form PDE in the Mathematics-PDE Interfaces was used to implement the partial differential equation described in equation (2.7) to solve for $\varphi_{e,sep}$. The General Form PDE equation is shown below

$$f = e_a \frac{\partial^2 u}{\partial t^2} + d_a \frac{\partial u}{\partial t} + \nabla \cdot \Gamma \quad (3.44)$$

where f is the source term, e_a is the mass coefficient, u is the dependent variable, d_a is the damping or mass coefficient, $\nabla = \frac{\partial}{\partial x}$, and Γ is the conservative flux. Matching like

coefficients between equations (2.7) and (3.44), results in the relations shown below in Table 3.8.

Table 3.8 1D Model, CBES Parameters

General Form	Value
f	0
e_a	0
d_a	0
Γ	$\kappa^{eff,sep} \frac{\partial}{\partial x} \varphi_{e,sep} + \kappa_{d,sep}^{eff,sep} \frac{\partial}{\partial x} \frac{\frac{\partial C_{e,sep}}{\partial x}}{C_{e,sep}}$

The effective ionic conductivity used in the conservative flux in equation (3.44), $\kappa^{eff,sep}$, was set equal to $\kappa_{sep}(\epsilon_{e,sep})^{brugg}$ as in there is Bruggeman correction used. Shown below is this relationship

$$\kappa^{eff,sep} = \kappa_{sep}(\epsilon_{e,sep})^{brugg} \quad (3.45)$$

where $\kappa^{eff,sep}$ is the effective electrical ionic conductivity, κ_{sep} is the graph in Figure 3.3, $\epsilon_{e,sep}$ is the separator electrolyte phase volume fraction, and *brugg* is the Bruggeman correction coefficient. The effective diffusion coefficient used in the conservative flux in equation (3.44), $\kappa_{d,sep}^{eff,sep}$, was set equal to $\frac{2RT}{F}(t_+ - 1)\kappa_{sep}(\epsilon_{e,sep})^{brugg}$ as in there is Bruggeman correction used. Shown below is this relationship

$$\kappa_{d,sep}^{eff,sep} = \frac{2RT}{F}(t_+ - 1)\kappa_{sep}(\epsilon_{e,sep})^{brugg} \quad (3.46)$$

where $\kappa_{d,sep}^{eff,sep}$ is the effective diffusion coefficient, R is the universal gas constant, T is temperature, F is Faraday's constant, t_+ is the transference number, κ_{sep} is the graph

in Figure 3.3, $\epsilon_{e,neg}$ is the separator electrolyte phase volume fraction, and $brugg$ is the Bruggeman correction coefficient. Within the General Form PDE interface an Initial Value subnode was created. Within this subnode, the region shown in Figure 3.23 was selected, and the initial value for $\varphi_{e,sep}$ was set to $-U_{neg}$ shown below

$$\varphi_{e,sep}(x, 0) = -U_{neg} \left(\frac{C_{s0,neg}}{C_{s,neg,max}} \right) \quad (3.47)$$

where $\varphi_{s,sep}$ is the potential in the electrolyte in the separator electrode, U_{neg} is the negative equilibrium voltage, $C_{s0,neg}$ is the initial concentration in the solid negative electrode, and $C_{s,neg,max}$ is the maximum concentration in the solid negative electrode. Then within the interface a Dirichlet Boundary Condition subnode was created. The boundary between the separator and the negative electrode shown in Figure 3.24 was selected and the value of $\varphi_{e,sep}$ was set equal to $\varphi_{e,neg}$ to maintain continuity as shown below

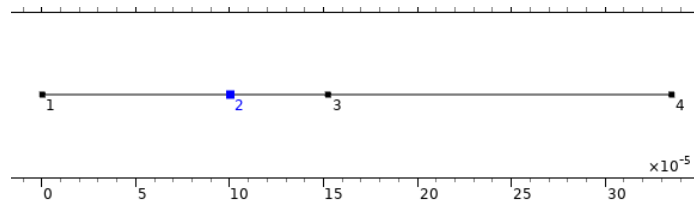


Figure 3.24 1D model, cbes dirichlet/flux boundary 1.

$$\varphi_{e,sep}(L_{neg}, t) = \varphi_{e,neg}(L_{neg}, t) \quad (3.48)$$

where $\varphi_{e,sep}$ is the potential in the separator electrolyte and $\varphi_{e,neg}$ is the potential in the negative electrolyte. After that within the interface an additional Dirichlet Boundary Condition subnode was created. The boundary between the separator and the positive electrode

as shown in Figure 3.25 was selected and the value of $\varphi_{e,sep}$ was set equal to $\varphi_{e,pos}$ to maintain continuity as shown below

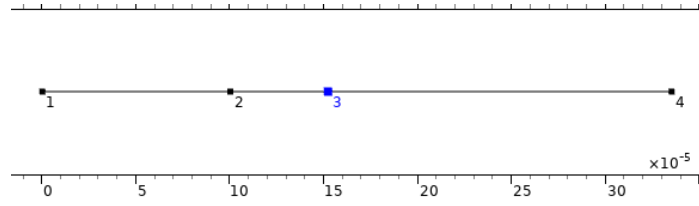


Figure 3.25 1D model, cbes dirichlet/flux boundary 2.

$$\varphi_{e,sep} \left((L_{neg} + L_{sep}), t \right) = \varphi_{e,pos} \left((L_{neg} + L_{sep}), t \right) \quad (3.49)$$

where $\varphi_{e,sep}$ is the potential in the separator electrolyte and $\varphi_{e,pos}$ is the potential in the positive electrolyte. Next within the interface a Flux/Source subnode was created. The equation used for the Flux/Source subnode is shown below as

$$-n \cdot \Gamma = g - qu \quad (3.50)$$

where n is the normal vector, Γ is the conservative flux, g is the boundary flux/source, q is the boundary absorption/impedance term, and u is the dependent variable. This flux is for continuity between the separator and negative electrode at the boundary as shown in Figure 3.24. Matching like coefficients between equations (2.8) and (3.50), results in the relations shown below in Table 3.9. With the convention that the negative of the normal vector is pointing into the domain, a positive flux means that the vector would be pointing into the domain and the potential would be moving to the right.

Table 3.9 1D Model, CBES Flux/Source 1

Flux/Source	Value
g	$\left(\kappa^{eff,neg} \frac{\partial}{\partial x} \varphi_{e,neg} + \kappa_{d,neg}^{eff,neg} \frac{\partial}{\partial x} \frac{\partial C_{e,neg}}{C_{e,neg}} \right)$
q	0

Finally within the interface an additional Flux/Source subnode was created. The equation used for the Flux/Source subnode is shown below

$$-n \cdot \Gamma = g - qu \quad (3.51)$$

where n is the normal vector, Γ is the conservative flux, g is the boundary flux/source, q is the boundary absorption/impedance term, and u is the dependent variable. This flux is for continuity between the separator and positive electrode at the boundary as shown in Figure 3.25. Matching like coefficients between equations (2.8) and (3.51), results in the relations shown below in Table 3.10. With the convention that the negative of the normal vector is pointing into the domain, a negative flux means that the vector would be pointing out of the domain and the potential would be moving to the right.

Table 3.10 1D Model, CBES Flux/Source 2

Flux/Source	Value
g	$-\left(\kappa^{eff,pos} \frac{\partial}{\partial x} \varphi_{e,pos} + \kappa_{d,pos}^{eff,pos} \frac{\partial}{\partial x} \frac{\partial C_{e,pos}}{C_{e,pos}} \right)$
q	0

3.2.8 Charge Balance Electrolyte Positive

The charge balance in the electrolyte phase of the positive electrode (CBEP) was applied to region 3 shown below in Figure 3.26.

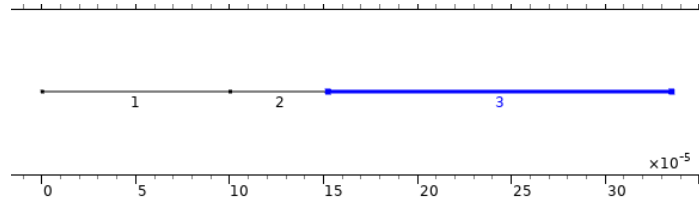


Figure 3.26 1D model, cbep region.

The General Form PDE in the Mathematics-PDE Interfaces was used to implement the partial differential equation described in equation (2.7) to solve for $\varphi_{e,pos}$. The General Form PDE equation is shown below

$$f = e_a \frac{\partial^2 u}{\partial t^2} + d_a \frac{\partial u}{\partial t} + \nabla \cdot \Gamma \quad (3.52)$$

where f is the source term, e_a is the mass coefficient, u is the dependent variable, d_a is the damping or mass coefficient, $\nabla = \frac{\partial}{\partial x}$, and Γ is the conservative flux. Matching like coefficients between equations (2.7) and (3.52), results in the relations shown below in Table 3.11.

Table 3.11 1D Model, CBEP Parameters

General Form	Value
f	$-\dot{J}_{i,neg}$
e_a	0
d_a	0
Γ	$\kappa^{eff,pos} \frac{\partial}{\partial x} \varphi_{e,pos} + \kappa_{d,pos}^{eff,pos} \frac{\partial}{\partial x} \frac{\partial C_{e,pos}}{C_{e,pos}}$

The effective ionic conductivity used in the conservative flux in equation (3.52), $\kappa^{eff,pos}$, was set equal to $\kappa_{pos}(\epsilon_{e,pos})^{brugg}$ as in there is Bruggeman correction used. Shown below is this relationship

$$\kappa^{eff,pos} = \kappa_{pos}(\epsilon_{e,pos})^{brugg} \quad (3.53)$$

where $\kappa^{eff,pos}$ is the effective electrical ionic conductivity, κ_{pos} is the graph in Figure 3.3, $\epsilon_{e,pos}$ is the positive electrolyte phase volume fraction, and *brugg* is the Bruggeman correction coefficient. The effective diffusion coefficient used in the conservative flux in equation (3.52), $\kappa_{d,pos}^{eff,pos}$, was set equal to $\frac{2RT}{F}(t_+ - 1)\kappa_{pos}(\epsilon_{e,pos})^{brugg}$ as in there is Bruggeman correction used. Shown below is this relationship

$$\kappa_{d,pos}^{eff,pos} = \frac{2RT}{F}(t_+ - 1)\kappa_{pos}(\epsilon_{e,pos})^{brugg} \quad (3.54)$$

where $\kappa_{d,pos}^{eff,pos}$ is the effective diffusion coefficient, R is the universal gas constant, T is temperature, F is Faraday's constant, t_+ is the transference number, κ_{neg} is the graph in Figure 3.3, $\epsilon_{e,pos}$ is the positive electrolyte phase volume fraction, and *brugg* is the bruggeman correction coefficient. Within the General Form PDE interface an Initial Value subnode was created. Within this subnode, the region shown in Figure 3.26 was selected, and the initial value for $\varphi_{e,pos}$ was set to $-U_{neg}$ shown as

$$\varphi_{e,pos}(x, 0) = -U_{neg} \left(\frac{C_{s0,neg}}{C_{s,neg,max}} \right) \quad (3.55)$$

where $\varphi_{s,pos}$ is the potential in the electrolyte in the positive electrode, U_{neg} is the negative equilibrium voltage, $c_{s0,neg}$ is the initial concentration in the solid negative electrode, and $c_{s,neg,max}$ is the maximum concentration in the solid negative electrode. Then within the interface a Dirichlet Boundary Condition subnode was created. The boundary between the positive electrode and the separator shown in Figure 3.27 was selected and the value of $\varphi_{e,pos}$ was set equal to $\varphi_{e,sep}$ as shown below to maintain continuity

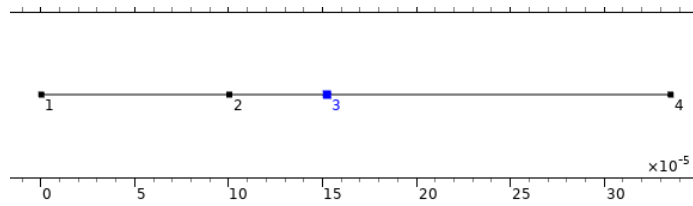


Figure 3.27 1D model, cbep dirichlet/flux boundary.

$$\varphi_{e,pos} \left((L_{neg} + L_{sep}), t \right) = \varphi_{e,sep} \left((L_{neg} + L_{sep}), t \right) \quad (3.56)$$

where $\varphi_{e,pos}$ is the potential in the positive electrolyte and $\varphi_{e,sep}$ is the potential in the separator electrolyte. Next the flux at the rightmost boundary as shown in Figure 3.28 was set to 0. The equation used for the Zero Flux subnode is shown below

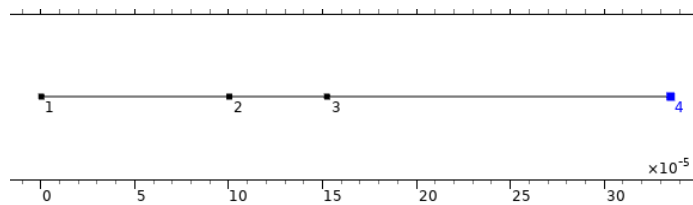


Figure 3.28 1D model, cbep zero flux boundary.

$$-n \cdot \Gamma = 0 \quad (3.57)$$

where n is the normal vector and Γ is the conservative flux. Finally within the interface a Flux/Source subnode was created. The equation used for the Flux/Source subnode is shown below

$$-n \cdot \Gamma = g - qu \quad (3.58)$$

where n is the normal vector, Γ is the conservative flux, g is the boundary flux/source, q is the boundary absorption/impedance term, and u is the dependent variable. This flux is for continuity between the positive electrode and separator at the boundary shown in Figure 3.27. Matching like coefficients between equations (2.8) and (3.58), results in the relations shown below in Table 3.12. With the convention that the negative of the normal vector is pointing into the domain, a positive flux means that the vector would be pointing into the domain and the potential would be moving to the right.

Table 3.12 1D Model, CBEP Flux/Source

Flux/Source	Value
g	$\left(\kappa^{eff,sep} \frac{\partial}{\partial x} \varphi_{e,sep} + \kappa_{d,sep}^{eff} \frac{\partial}{\partial x} \frac{\frac{\partial C_{e,sep}}{\partial x}}{C_{e,sep}} \right)$
q	0

3.2.9 Material Balance Electrolyte Negative

The material balance in the electrolyte phase of the negative electrode (MBEN) was applied to region 1 shown below in Figure 3.29.

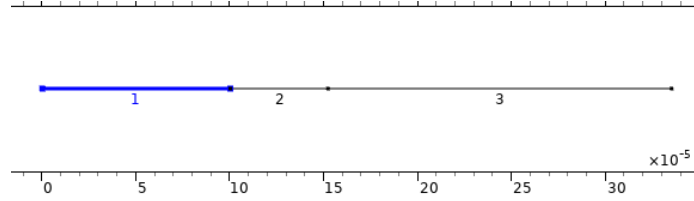


Figure 3.29 1D model, mben region.

The General Form PDE in the Mathematics-PDE Interfaces was used to implement the partial differential equation described in equation (2.3) to solve for $C_{e,neg}$. The General Form PDE equation is shown below

$$f = e_a \frac{\partial^2 u}{\partial t^2} + d_a \frac{\partial u}{\partial t} + \nabla \cdot \Gamma \quad (3.59)$$

where f is the source term, e_a is the mass coefficient, u is the dependent variable, d_a is the damping or mass coefficient, $\nabla = \frac{\partial}{\partial x}$, and Γ is the conservative flux. Matching like coefficients between equations (2.3) and (3.59), results in the relations shown below in Table 3.13.

Table 3.13 1D Model, MBEN Parameters

General Form	Value
f	$\frac{j_{i,neg}(1-t_+)}{F}$
e_a	0
d_a	$\epsilon_{e,neg}$
Γ	$-D_{e,neg}^{eff} \frac{\partial C_{e,neg}}{\partial x}$

The diffusion coefficient used in the conservative flux in equation (3.59), $D_{e,neg}^{eff}$, was set equal to $D_{e,neg}(\epsilon_{e,neg})^{brugg}$ as in there is Bruggeman correction used. Shown below is this relationship

$$D_{e,neg}^{eff} = D_{e,neg}(\epsilon_{e,neg})^{brugg} \quad (3.60)$$

where $D_{e,neg}^{eff}$ is the effective diffusion coefficient, $D_{e,neg}$ is the diffusion coefficient, $\epsilon_{e,neg}$ is the negative electrolyte phase volume fraction, and $brugg$ is the Bruggeman correction coefficient. Within the General Form PDE interface an Initial Value subnode was created. Within this subnode, the region shown in Figure 3.29 was selected, and the initial value for $C_{e,neg}$ was set to c_{l0} as shown below

$$C_{e,neg}(x, 0) = c_{l0} \quad (3.61)$$

where $C_{e,neg}$ is the concentration in the electrolyte in the negative electrode and c_{l0} is the initial concentration. Then within the interface a Dirichlet Boundary Condition subnode was created. The boundary between the negative electrode and the separator shown in Figure 3.30 was selected and the value of $C_{e,neg}$ was set equal to $C_{e,sep}$ as shown below to maintain continuity

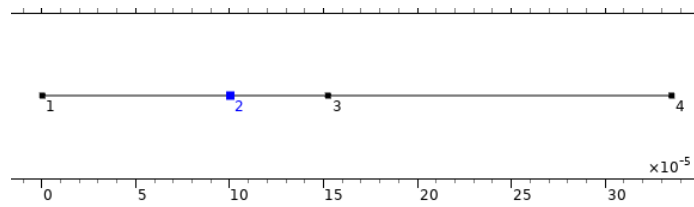


Figure 3.30 1D model, mben dirichlet/flux boundary.

$$C_{e,neg}(L_{neg}, t) = C_{e,sep}(L_{neg}, t) \quad (3.62)$$

where $C_{e,neg}$ is the concentration in the negative electrolyte and $C_{e,sep}$ is the concentration in the separator electrolyte. Next the flux at the leftmost boundary shown in Figure 3.31 was set to 0. The equation used for the Zero Flux subnode is shown below

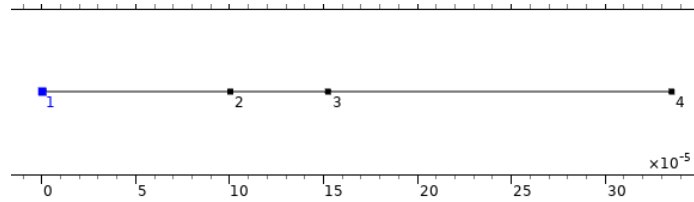


Figure 3.31 1D model, mben zero flux boundary.

$$-n \cdot \Gamma = 0 \quad (3.63)$$

where n is the normal vector and Γ is the conservative flux. Finally within the interface a Flux/Source subnode was created. The equation used for the Flux/Source subnode is shown below

$$-n \cdot \Gamma = g - qu \quad (3.64)$$

where n is the normal vector, Γ is the conservative flux, g is the boundary flux/source, q is the boundary absorption/impedance term, and u is the dependent variable. This flux is for continuity between the negative electrode and separator at the boundary shown in Figure 3.30. Matching like coefficients between equations (2.4) and (3.64), results in the relations shown below in Table 3.14. With the convention that the negative of the normal vector is pointing into the domain, a positive flux means that the vector would be pointing into the domain and the flux would be moving to the left.

Table 3.14 1D Model, MBEN Flux/Source

Flux/Source	Value
g	$D_{e,sep}(\epsilon_{e,sep})^{brugg} \frac{\partial C_{e,sep}}{\partial x}$
q	0

3.2.10 Material Balance Electrolyte Separator

The material balance in the electrolyte phase of the separator (MBES) was applied to region 2 shown below in Figure 3.32.

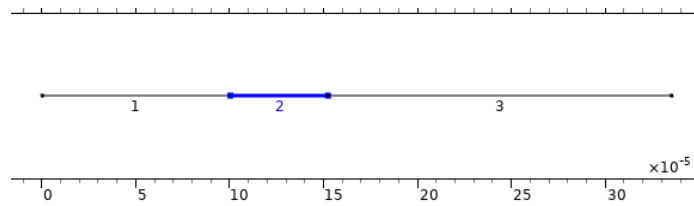


Figure 3.32 1D model, mbes region.

The General Form PDE in the Mathematics-PDE Interfaces was used to implement the partial differential equation described in equation (2.3) to solve for $C_{e,sep}$. The General Form PDE equation is shown below

$$f = e_a \frac{\partial^2 u}{\partial t^2} + d_a \frac{\partial u}{\partial t} + \nabla \cdot \Gamma \quad (3.65)$$

where f is the source term, e_a is the mass coefficient, u is the dependent variable, d_a is the damping or mass coefficient, $\nabla = \frac{\partial}{\partial x}$, and Γ is the conservative flux. Matching like coefficients between equations (2.3) and (3.65), results in the relations shown in Table 3.15.

Table 3.15 1D Model, MBES Parameters

General Form	Value
f	0
e_a	0
d_a	$\epsilon_{e,sep}$
Γ	$-D_{e,sep}^{eff} \frac{\partial C_{e,sep}}{\partial x}$

The diffusion coefficient used in the conservative flux in equation (3.65), $D_{e,sep}^{eff}$, was set equal to $D_{e,sep}(\epsilon_{e,sep})^{brugg}$ as in there is Bruggeman correction used. Shown below is this relationship

$$D_{e,sep}^{eff} = D_{e,sep}(\epsilon_{e,sep})^{brugg} \quad (3.66)$$

where $D_{e,sep}^{eff}$ is the effective diffusion coefficient, $D_{e,sep}$ is the diffusion coefficient, $\epsilon_{e,sep}$ is the separator electrolyte phase volume fraction, and $brugg$ is the Bruggeman correction coefficient. Within the General Form PDE interface an Initial Value subnode was created. Within this subnode, the region shown in Figure 3.32 was selected, and the initial value for $C_{e,sep}$ was set to c_{l0} shown below

$$C_{e,sep}(x, 0) = c_{l0} \quad (3.67)$$

where $C_{e,sep}$ is the concentration in the electrolyte in the separator electrode and c_{l0} is the initial concentration. Then within the interface a Dirichlet Boundary Condition subnode was created. The boundary between the separator and the negative electrode shown in Figure 3.33 was selected and the value of $C_{e,sep}$ was set equal to $C_{e,neg}$ to maintain continuity

as shown below

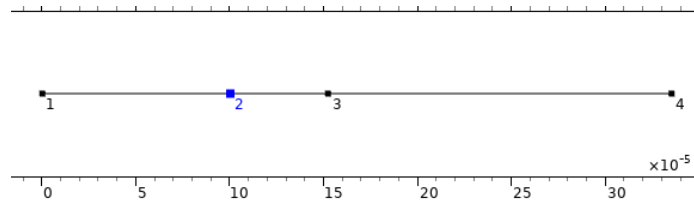


Figure 3.33 1D model, mbes dirichlet/flux boundary 1.

$$C_{e,sep}(L_{neg}, t) = C_{e,neg}(L_{neg}, t) \quad (3.68)$$

where $C_{e,sep}$ is the concentration in the separator electrolyte and $C_{e,neg}$ is the concentration in the negative electrolyte. Then an additional Dirichlet Boundary Condition subnode was created. The boundary between the separator and the positive electrode as shown in Figure 3.34 was selected and the value of $C_{e,sep}$ was set equal to $C_{e,pos}$ to maintain continuity as shown below

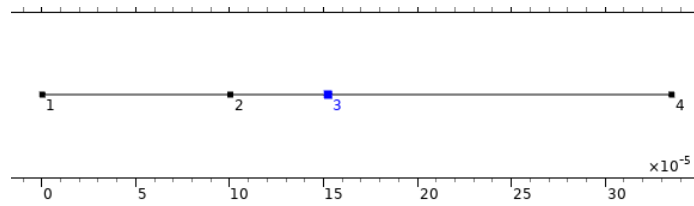


Figure 3.34 1D model, mbes dirichlet/flux boundary 2.

$$C_{e,sep}\left((L_{neg} + L_{sep}), t\right) = C_{e,pos}\left((L_{neg} + L_{sep}), t\right) \quad (3.69)$$

where $C_{e,sep}$ is the concentration in the separator electrolyte and $C_{e,pos}$ is the concentration in the positive electrolyte. Then within the interface a Flux/Source subnode was created. The equation used for the Flux/Source subnode is shown as

$$-n \cdot \Gamma = g - qu \quad (3.70)$$

where n is the normal vector, Γ is the conservative flux, g is the boundary flux/source, q is the boundary absorption/impedance term, and u is the dependent variable. This flux is for continuity between the separator and the negative electrode at the boundary as shown in Figure 3.33. Matching like coefficients between equations (2.4) and (3.70), results in the relations shown below in Table 3.16. With the convention that the negative of the normal vector is pointing into the domain, a negative flux means that the vector would be pointing out of the domain and the flux would be moving to the left.

Table 3.16 1D Model, MBES Flux/Source 1

Flux/Source	Value
g	$-D_{e,neg}(\epsilon_{e,neg})^{brugg} \frac{\partial C_{e,neg}}{\partial x}$
q	0

Finally within the interface an additional Flux/Source subnode was created. The equation used for the Flux/Source subnode is shown below

$$-n \cdot \Gamma = g - qu \quad (3.71)$$

where n is the normal vector, Γ is the conservative flux, g is the boundary flux/source, q is the boundary absorption/impedance term, and u is the dependent variable. This flux is for continuity between the separator and the positive electrode at the boundary as shown in Figure 3.34. Matching like coefficients between equations (2.4) and (3.71), results in the

relations shown below in Table 3.17. With the convention that the negative of the normal vector is pointing into the domain, a positive flux means that the vector would be pointing into the domain and the flux would be moving to the left.

Table 3.17 1D Model, MBES Flux/Source 2

Flux/Source	Value
g	$D_{e,pos}(\epsilon_{e,pos})^{brugg} \frac{\partial C_{e,pos}}{\partial x}$
q	0

3.2.11 Material Balance Electrolyte Positive

The material balance in the electrolyte phase of the positive electrode (MBEP) was applied to region 3 shown below in Figure 3.35.

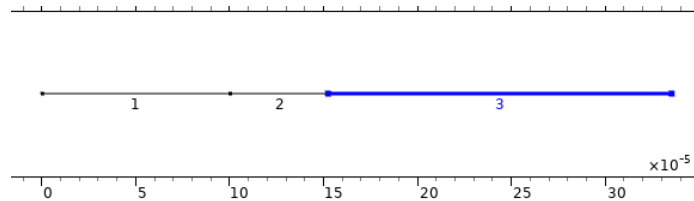


Figure 3.35 1D model, mbep region.

The General Form PDE in the Mathematics-PDE Interfaces was used to implement the partial differential equation described in equation (2.3) to solve for $C_{e,pos}$. The General Form PDE equation is shown below

$$f = e_a \frac{\partial^2 u}{\partial t^2} + d_a \frac{\partial u}{\partial t} + \nabla \cdot \Gamma \quad (3.72)$$

where f is the source term, e_a is the mass coefficient, u is the dependent variable, d_a is the damping or mass coefficient, $\nabla = \frac{\partial}{\partial x}$, and Γ is the conservative flux. Matching like

coefficients between equations (2.3) and (3.72), results in the relations shown below in Table 3.18.

Table 3.18 1D Model, MBEP Parameters

General Form	Value
f	$\frac{j_{i,pos}(1-t_+)}{F}$
e_a	0
d_a	$\epsilon_{e,pos}$
Γ	$-D_{e,pos}^{eff} \frac{\partial C_{e,pos}}{\partial x}$

The diffusion coefficient used in the conservative flux in equation (3.72), $D_{e,pos}^{eff}$, was set equal to $D_{e,pos}(\epsilon_{e,pos})^{brugg}$ as in there is Bruggeman correction used. Shown below is this relationship

$$D_{e,pos}^{eff} = D_{e,pos}(\epsilon_{e,pos})^{brugg} \quad (3.73)$$

where $D_{e,pos}^{eff}$ is the effective diffusion coefficient, $D_{e,pos}$ is the diffusion coefficient, $\epsilon_{e,pos}$ is the positive electrolyte phase volume fraction, and $brugg$ is the Bruggeman correction coefficient. Within the General Form PDE interface an Initial Value subnode was created. Within this subnode, the region shown in Figure 3.35 was selected, and the initial value for $C_{e,pos}$ was set to c_{l0} as shown below

$$C_{e,pos}(x, 0) = c_{l0} \quad (3.74)$$

where $C_{e,pos}$ is the concentration in the electrolyte in the positive electrode and c_{l0} is the initial concentration. Then within the interface a Dirichlet Boundary Condition subnode

was created. The boundary between the positive electrode and the separator shown in Figure 3.36 was selected and the value of $C_{e,pos}$ was set equal to $C_{e,sep}$ as shown below to maintain continuity.

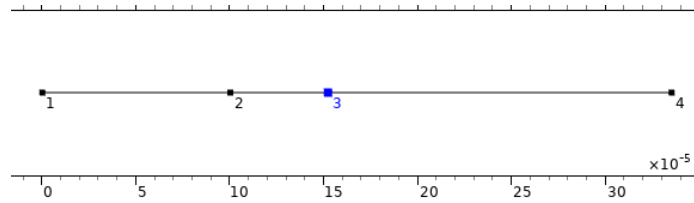


Figure 3.36 1D model, mbep dirichlet/flux boundary.

$$C_{e,pos}\left((L_{neg} + L_{sep}), t\right) = C_{e,sep}\left((L_{neg} + L_{sep}), t\right) \quad (3.75)$$

where $C_{e,pos}$ is the concentration in the positive electrolyte and $C_{e,sep}$ is the concentration in the separator electrolyte. Next the flux at the rightmost boundary shown in Figure 3.37 was set to 0. The equation used for the Zero Flux subnode is shown below

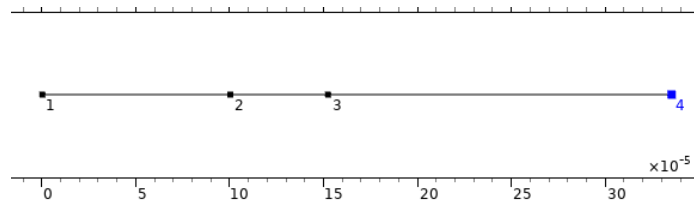


Figure 3.37 1D model, mbep zero flux boundary.

$$-n \cdot \Gamma = 0 \quad (3.76)$$

where n is the normal vector and Γ is the conservative flux. Finally within the interface a Flux/Source subnode was created. The equation used for the Flux/Source subnode is shown below

$$-n \cdot \Gamma = g - qu \quad (3.77)$$

where n is the normal vector, Γ is the conservative flux, g is the boundary flux/source, q is the boundary absorption/impedance term, and u is the dependent variable. This flux is for continuity between the positive electrode and separator at the boundary shown in Figure 3.36. Matching like coefficients between equations (2.4) and (3.77), results in the relations shown below in Table 3.19. With the convention that the negative of the normal vector is pointing into the domain, a negative flux means that the vector would be pointing out of the domain and the flux would be moving to the left.

Table 3.19 1D Model, MBEP Flux/Source

Flux/Source	Value
g	$-D_{e,sep}(\epsilon_{e,sep})^{brugg} \frac{\partial C_{e,sep}}{\partial x}$
q	0

3.2.12 Material Balance Solid Negative

The material balance in the solid phase of the negative electrode (MBSN) is calculated in its own two dimensional domain. Shown below in Figure 3.38 is the two dimensional domain.

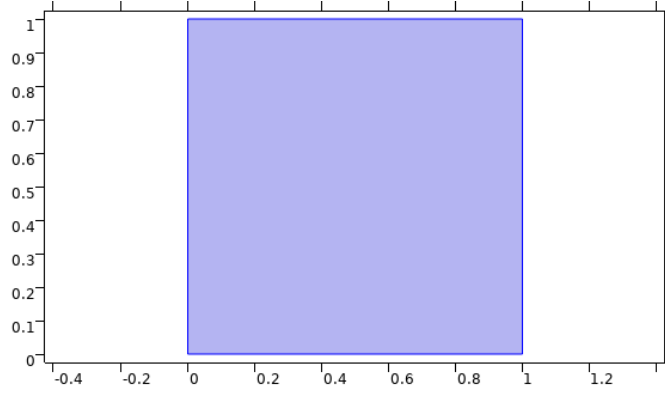


Figure 3.38 1D model, mbsn region.

The General Form PDE in the Mathematics-PDE Interfaces was used to implement the partial differential equation described in equation (2.5) to solve for $C_{s,neg}$. The General Form PDE equation is shown below

$$f = e_a \frac{\partial^2 u}{\partial t^2} + d_a \frac{\partial u}{\partial t} + \nabla \cdot \Gamma \quad (3.78)$$

where f is the source term, e_a is the mass coefficient, u is the dependent variable, d_a is the damping or mass coefficient, $\nabla = \frac{\partial}{\partial x}, \frac{\partial}{\partial y}$, and Γ is the conservative flux. The top boundary shown in Figure 3.39 of the domain is the function that is mapped to the one dimensional domain for the negative electrode. The y-dimension represents the radius of a sphere at that x value. The top boundary is when y is equal to the radius of the spherical particle ($r = R_p$). The bottom boundary is when y is equal to 0 which represents the center of a spherical particle ($r = 0$).

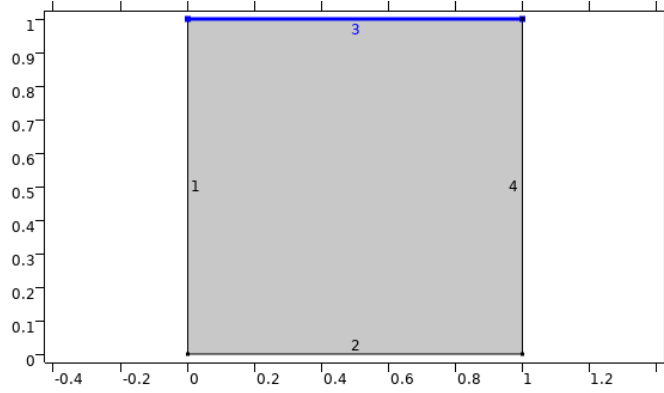


Figure 3.39 1D model, mbsn flux/top boundary.

To avoid division by zero when ($r = 0$), equation (2.5) is multiplied by r^2 . The resulting partial differential equation is shown below

$$r^2 \frac{\partial C_s}{\partial t} = D_s \frac{\partial}{\partial r} \left(r^2 \frac{\partial C_s}{\partial r} \right) \quad (3.79)$$

where C_s is the concentration in the solid phase and D_s is the diffusion coefficient. After that the equation is scaled in reference to the particle radius. The scaling is done through the relationship shown below

$$\begin{aligned} \hat{r} &= \frac{r}{R_p} \\ \frac{\partial}{\partial r} &= \frac{1}{R_p} \frac{\partial}{\partial \hat{r}} \end{aligned} \quad (3.80)$$

With these changes the new partial differential equation that describes the diffusion of lithium in the solid phase is shown below as

$$\hat{r}^2 \frac{\partial C_s}{\partial t} = D_s \frac{\partial}{\partial \hat{r}} \left(\frac{\hat{r}^2}{R_p^2} \frac{\partial C_s}{\partial \hat{r}} \right) \quad (3.81)$$

where C_s is the concentration in the solid phase, D_s is the diffusion coefficient, and R_p is the particle radius. Matching like coefficients between equations (3.81) and (3.78), results in the relations shown below in Table 3.20.

Table 3.20 1D Model, MBSN Parameters

General Form	Value
f	0
e_a	0
d_a	r^2
Γ_x	0
Γ_y	$-D_{s,neg} \frac{r^2}{(R_{s,neg})^2} \frac{\partial C_{s,neg}}{\partial r}$

The flux at the surface of the particle would also need to change. Shown below is the adjusted flux at the surface while the other two conditions in equation (2.6) are reiterated

$$\begin{aligned}
 -D_s \frac{\partial C_s}{\partial x} \Big|_{r=0} &= 0 \\
 -D_s \frac{\partial C_s}{\partial x} \Big|_{r=R_p} &= \frac{\hat{r}^2}{R_p} \frac{j_{li}}{a_s F} \\
 C_s(r, 0) &= C_s^{init}(r)
 \end{aligned} \tag{3.82}$$

where R_p is the radius of the particle, j_{li} is the pore-wall flux across the interface, F is Faraday's constant, and a_s is the surface area to volume ratio. Within the General Form PDE interface an Initial Value subnode was created. Within this subnode, the region shown in Figure 3.38 was selected, and the initial value for $C_{s,neg}$ was set to $c_{s0,neg}$ as shown below

$$C_{s,neg}(r, y, 0) = c_{s0,neg} \tag{3.83}$$

where $C_{s,neg}$ is the concentration in the solid negative electrode and $c_{s0,neg}$ is the initial concentration in the solid phase. Next the flux at the boundaries labelled 1, 2, and 4 as shown in Figure 3.40 were set to zero. The equation used for the Zero Flux subnode is shown below

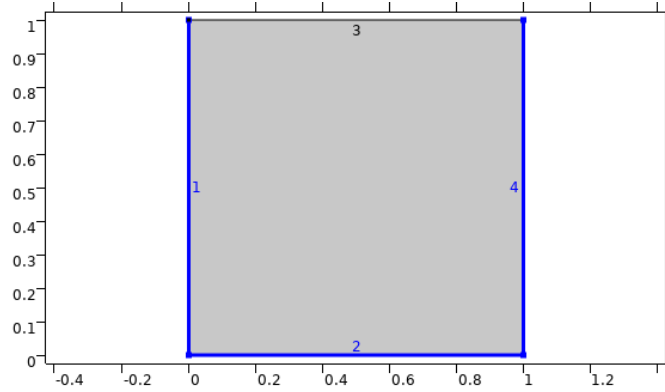


Figure 3.40 1D model, mbsn zero flux boundaries.

$$-n \cdot \Gamma = 0 \quad (3.84)$$

where n is the normal vector and Γ is the conservative flux. Finally within the interface a Flux/Source subnode was created. The equation used for the Flux/Source subnode is shown below

$$-n \cdot \Gamma = g - qu \quad (3.85)$$

where n is the normal vector, Γ is the conservative flux, g is the boundary flux/source, q is the boundary absorption/impedance term, and u is the dependent variable. This flux is for pore-wall flux across the interface on the boundary shown in Figure 3.39. Matching like

coefficients between equations (3.82) and (3.85), results in the relations shown below in Table 3.21. With the convention that the negative of the normal vector is pointing into the domain, a negative flux means that the vector would be pointing out of the domain and the flux would be moving to the upwards.

Table 3.21 1D Model, MBSN Flux/Source

Flux/Source	Value
g	$-\frac{r^2}{R_{s,neg}} \frac{j_{li,neg}}{a_{s,neg} F}$
q	0

3.2.13 Material Balance Solid Positive

The material balance in the solid phase of the positive electrode (MBSP) is calculated in its own two dimensional domain. Shown below in Figure 3.41 is the two dimensional domain.

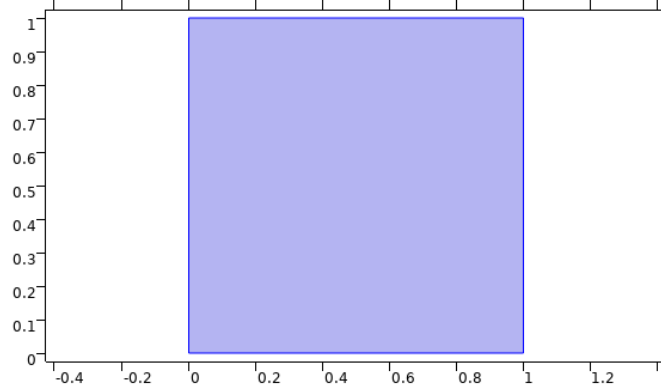


Figure 3.41 1D model, mbsp region.

The General Form PDE in the Mathematics-PDE Interfaces was used to implement the partial differential equation described in equation (3.81) to solve for $C_{s,pos}$. The General Form PDE equation is shown below

$$f = e_a \frac{\partial^2 u}{\partial t^2} + d_a \frac{\partial u}{\partial t} + \nabla \cdot \Gamma \quad (3.86)$$

where f is the source term, e_a is the mass coefficient, u is the dependent variable, d_a is the damping or mass coefficient, $\nabla = \frac{\partial}{\partial x}, \frac{\partial}{\partial y}$, and Γ is the conservative flux. The top boundary shown in Figure 3.42 of the domain is the function that is mapped to the one dimensional domain for the positive electrode. The y-dimension represents the radius of a sphere at that x value. The top boundary is when y is equal to the radius of the spherical particle ($r = R_p$). The bottom boundary is when y is equal to 0 which represents the center of a spherical particle ($r = 0$).

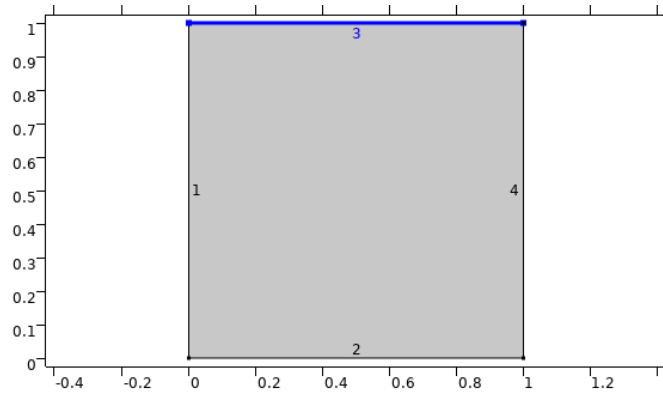


Figure 3.42 1D model, mbsp flux/top boundary.

Matching like coefficients between equations (3.81) and (3.86), results in the relations shown below in Table 3.22.

Table 3.22 1D Model, MBSP Parameters

General Form	Value
f	0
e_a	0
d_a	r^2
Γ_x	0
Γ_y	$-D_{s,pos} \frac{r^2}{(R_{s,pos})^2} \frac{\partial C_{s,pos}}{\partial r}$

Within the General Form PDE interface an Initial Value subnode was created. Within this subnode, the region shown in Figure 3.41 was selected, and the initial value for $C_{s,pos}$ was set to $c_{s0,pos}$ as shown below

$$C_{s,pos}(r, y, 0) = c_{s0,pos} \quad (3.87)$$

where $C_{s,pos}$ is the concentration in the solid negative positive and c_{pos} is the initial concentration in the solid phase. Next the flux at the boundaries labelled 1, 2, and 4 as shown in Figure 3.43 were set to zero. The equation used for the Zero Flux subnode is shown below

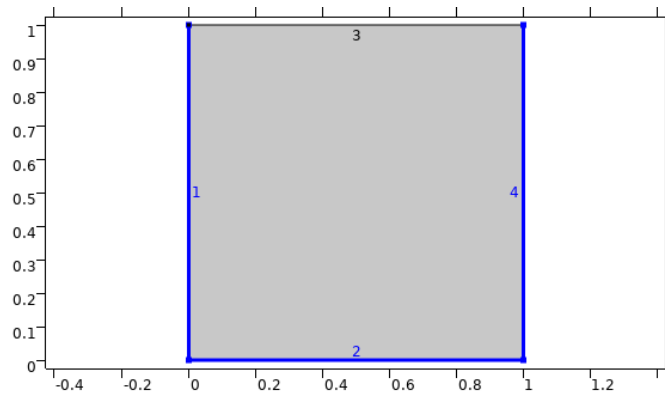


Figure 3.43 1D model, mbsp zero flux boundaries.

$$-n \cdot \Gamma = 0 \quad (3.88)$$

where n is the normal vector and Γ is the conservative flux. Finally within the interface a Flux/Source subnode was created. The equation used for the Flux/Source subnode is shown below

$$-n \cdot \Gamma = g - qu \tag{3.89}$$

where n is the normal vector, Γ is the conservative flux, g is the boundary flux/source, q is the boundary absorption/impedance term, and u is the dependent variable. This flux is for pore-wall flux across the interface on the boundary shown in Figure 3.42. Matching like coefficients between equations (3.82) and (3.89), results in the relations shown below in Table 3.23. With the convention that the negative of the normal vector is pointing into the domain, a negative flux means that the vector would be pointing out of the domain and the flux would be moving to the upwards.

Table 3.23 1D Model, MBSP Flux/Source

Flux/Source	Value
g	$-\frac{r^2}{R_{s,pos}} \frac{j_{li,pos}}{a_{s,pos} F}$
q	0

3.2.14 Linear Extrusions

Because the model has three components to it; a one dimensional domain, a two dimensional domain, and an additional two dimensional name, COMSOL does not directly allow solved dependent variables to be cross coupled to other components. To accomplish this there are multiple options. The the most abstract way is what COMSOL calls General Extrusions. But in the case of this model a Linear Extrusion would suffice because in all three cases a boundary is being mapped to a boundary.

For the component that consists of eight partial differential equations; CBSN, CBSP, CBEN, CBES, CBEP, MBEN, MBES, and MBEP two linear extrusions are required. One

linear extrusion is required to couple the variables to the material balance in the solid negative electrode (MBSN), and the second linear extrusion is required to couple the variables to the material balance in the solid positive electrode (MBSP).

For the linear extrusion to the MBSN, the source domain would be the region shown in Figures 3.14, 3.20, and 3.29. This region is again shown below in Figure 3.44. The destination domain would be Geometry 2 which is the geometry for the MBSN shown in the model tree in Figure 3.1 and shown below in Figure 3.45.

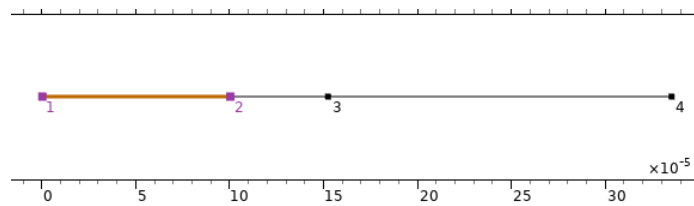


Figure 3.44 1D model, linear extrusion 1 source.

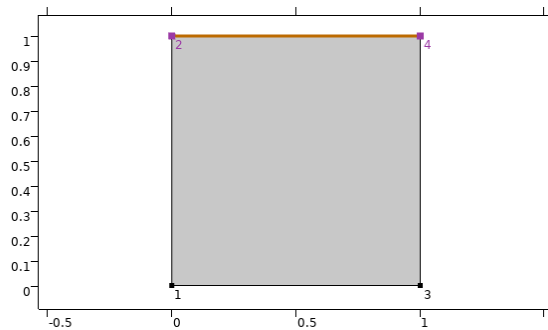


Figure 3.45 1D model, linear extrusion 1 destination.

Source vertex 1 would be point 1 in Figure 3.44 and source vertex 2 would be point 2 in Figure 3.44. Destination vertex 1 would be point 2 in Figure 3.45 and destination vertex 2 would be point 4 in Figure 3.45.

For the linear extrusion to the MBSP, the source domain would be the region shown in Figures 3.17, 3.26, and 3.35. This region is again shown below in Figure 3.46. The destination domain would be Geometry 3 which is the geometry for the MBSP shown in

the model tree in Figure 3.1 and shown below in Figure 3.47.

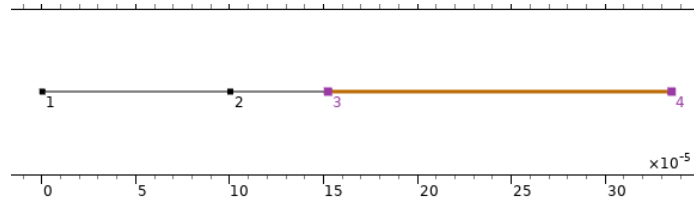


Figure 3.46 1D model, linear extrusion 2 source.

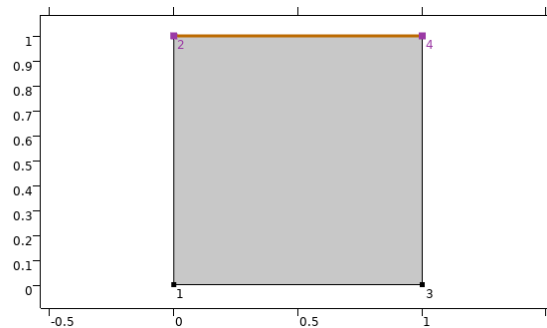


Figure 3.47 1D model, linear extrusion 2 destination.

Source vertex 1 would be point 3 in Figure 3.46 and source vertex 2 would be point 4 in Figure 3.46. Destination vertex 1 would be point 2 in Figure 3.47 and destination vertex 2 would be point 4 in Figure 3.47.

For the component that consists of the partial differential equation for the material balance in the solid negative electrode (MBSN), one linear extrusion is required. One is only because it is only mapping to the component that has the CBSN, CBSP, CBEN, CBES, CBEP, MBEN, MBES, and MBEP equations.

For the linear extrusion to the main component, the source domain would be region shown below in Figure 3.48. The destination domain would be Geometry 1 which is the geometry for the main component shown in the model tree in Figure 3.1, and the region shown in Figures 3.14, 3.20, and 3.29. This region is again shown below in Figure 3.49.

Source vertex 1 would be point 2 in Figure 3.48 and source vertex 2 would be point

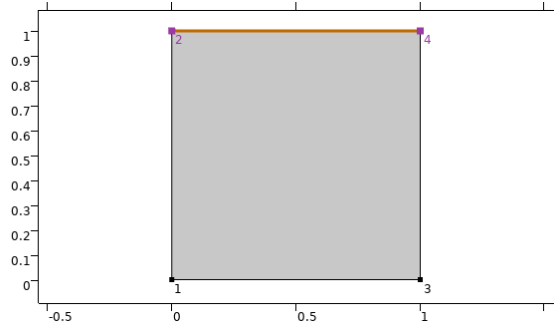


Figure 3.48 1D model, linear extrusion 3 source.

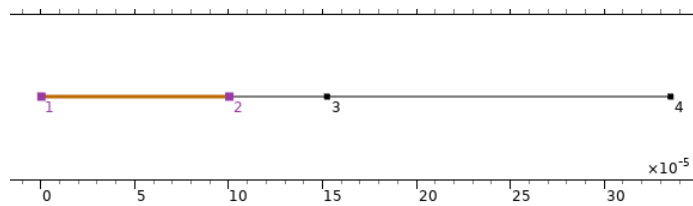


Figure 3.49 1D model, linear extrusion 3 destination.

4 in Figure 3.48. Destination vertex 1 would be point 1 in Figure 3.49 and destination vertex 2 would be point 2 in Figure 3.49.

For the component that consists of the partial differential equation for the material balance in the solid positive electrode (MBSP), one linear extrusion is required. One is only required because it is only mapping to the component that has the CBSN, CBSP, CBEN, CBES, CBEP, MBEN, MBES, and MBEP equations.

For the linear extrusion to the main component, the source domain would be region shown below in Figure 3.50. The destination domain would be Geometry 1 which is the geometry for the main component shown in the model tree in Figure 3.1, and the region shown in Figures 3.17, 3.26, and 3.35. This region is again shown below in Figure 3.51.

Source vertex 1 would be point 2 in Figure 3.50 and source vertex 2 would be point 4 in Figure 3.50. Destination vertex 1 would be point 3 in Figure 3.51 and destination vertex 2 would be point 4 in Figure 3.51.

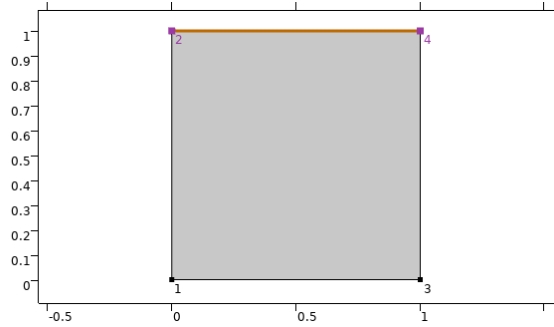


Figure 3.50 1D model, linear extrusion 4 source.

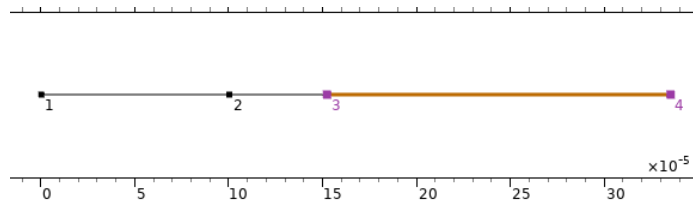


Figure 3.51 1D model, linear extrusion 4 destination.

3.3 COMSOL 2D Modeling

Building on the one dimensional model developed in the previous section is a two dimensional model that could experience the effects of a magnetic field. A two dimensional domain was created to represent a negative electrode, a separator, and a positive electrode. Then a three dimensional domain was created to represent the diffusion in the solid negative electrode. Followed by an additional three dimensional domain to represent the diffusion in the solid positive electrode.

3.3.1 Model Definition

Starting with a two dimensional domain are three rectangles connected together. The first rectangle represents the negative electrode, the second rectangle represents the separator, and the final rectangle represents the positive electrode. In the negative electrode are three partial differential equations; one for the charge balance in the solid negative electrode, one for the charge balance in the electrolyte in that region, and one for the material balance in the

electrolyte in that region. In the separator region there are two partial differential equations; one for the charge balance in the electrolyte in that region and one for the material balance in the electrolyte in that region. In the positive electrode there are three partial differential equations; one for the charge balance in the solid positive electrode, one for the charge balance in the electrolyte in that region, and one for the material balance in the electrolyte in that region.

For the negative electrode there is a three dimensional domain representing the diffusion. And for the positive electrode there is an additional three dimensional domain representing the diffusion. Shown below in Figure 3.52 is the model tree showing each aspect of the model.

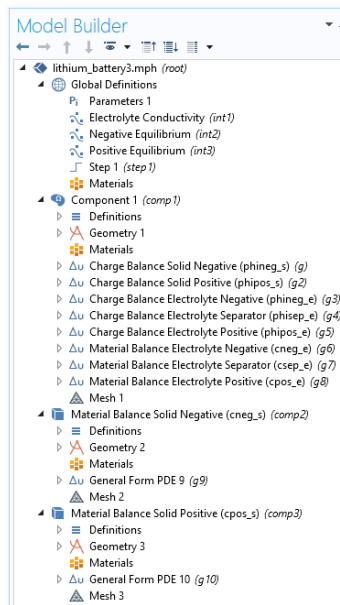


Figure 3.52 2D model, model tree.

Shown below in Figure 3.53 is a diagram of where each variable is solved and the three domains.

With the above figure the top face of $C_{s,neg}$ is extruded to the region containing $C_{e,neg}$, $\varphi_{e,neg}$, and $\varphi_{s,neg}$. Similarly $C_{s,pos}$ is extruded to the region containing $C_{e,pos}$, φ_{pos} ,

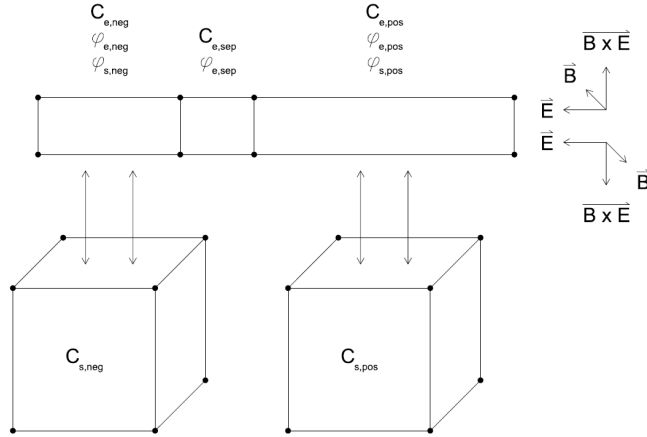


Figure 3.53 2D model, model diagram.

and $\varphi_{s,pos}$.

3.3.2 Global Definitions

Within the previously described domains are common functions and parameters that are used in each. The first function is the electrolyte conductivity which is a function of the concentration of electrolyte at every point. This coefficient is used in the effective ionic conductivity and effective diffusion coefficients described in equation (2.7). It was shown previously in Figure 3.3. This electrolyte conductivity is used within the model by having its input be the electrolyte concentration divided by 1000. This relationship was shown previously in equation (3.20). From Figure 3.3 the electrolyte conductivity ranges from 0.02 to 0.28. The input concentrations range from 0 to 3000.

The second function is that of the negative equilibrium voltage in the negative electrode. This equilibrium voltage is used in the Butler-Volmer equation shown in equation (2.11). Shown previously in Figure 3.4 is the relation for the negative equilibrium voltage. This negative equilibrium voltage is used within the model by having its input be the concentration of the solid phase in the negative electrode at the surface divided by the max

concentration allowed in the negative electrode. This relationship was shown previously in equation (3.21). From Figure 3.4 the negative equilibrium voltage ranges from 0 to 1. The input concentrations range from a ratio of 0 and a ratio of 0.7.

The third function is that of the positive equilibrium voltage in the positive electrode. This equilibrium voltage is used in the Butler-Volmer equation shown in equation (2.11). Shown previously in Figure 3.5 is the relation for the positive equilibrium voltage. The positive equilibrium voltage is used within the model by having its input be the concentration of the solid phase in the positive electrode at the surface divided by the max concentration allowed in the positive electrode. This relationship was shown previously in equation (3.22). From Figure 3.5 the positive equilibrium voltage ranges from 3.6 to 4.3. The input concentrations range from a ratio of 0.2 to a ratio of 1.

The fourth function is that of the pore-wall flux across the interface for the negative electrode. This equation was shown previously in equation (3.23). The fifth function is that of the pore-wall flux across the interface for the positive electrode. This equation was shown previously in equation (3.24).

The sixth function is that of the step function shown in Figure 3.6. The same Variables subnode was also used to properly implement the step function in the model. The information for this subnode is found in Table 3.1.

To set up the model properly many constants and parameters were used. The same constants used for the negative electrode, the separator, and the positive electrode in the one dimensional model were used for the two dimensional model and are shown in Table 3.2. Additional parameters were needed for the increased dimensions and for the magnetic field. The additional parameters are shown below in Table 3.24.

There is a derived value in Table 3.24 and it is that of the magnetic flux density B_z .

Table 3.24 Constants and Parameters 2

Name	Value	Description
L_{height}	40E-6	Height of Electrode
B_z	10E-3	Magnetic Flux Density
μ_0	$4\pi 10E-7$	Permeability of Free Space
H_z	795.775	Magnetic Field Strength

Shown below is the expression for the magnetic flux density.

$$B_z = \mu_0 H_z \quad (3.90)$$

where B_z is the magnetic flux density, μ_0 is the permeability of free space, and H_z is the magnetic field strength.

3.3.3 Geometries and Meshes

Shown below in Figure 3.54 are the three regions for the two dimensional domain representing the negative electrode, separator, and positive electrode.

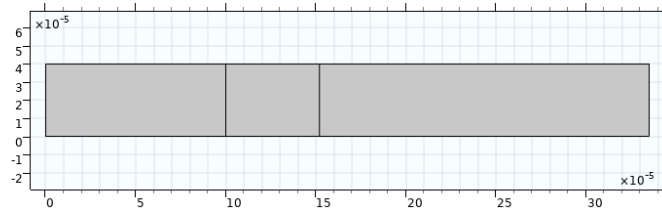


Figure 3.54 2D model, 2d domain.

The numbering convention for the points is shown below in Figure 3.55.

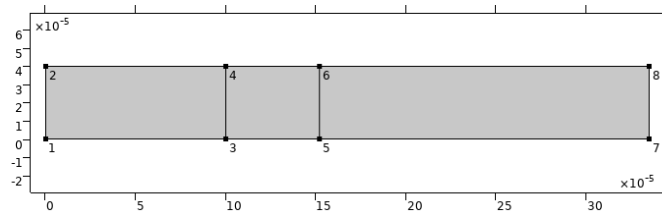


Figure 3.55 2D model, 2d points.

The distance between points 1 and 3 is L_{neg} , the distance between points 3 and 5 is L_{sep} , and the distance between points 5 and 7 is L_{pos} . The distance between points 1 and 2, 3 and 4, 5 and 6, and 7 and 8 is L_{height} . Different partial differential equations apply to different regions of the geometry shown in Figure 3.54. The numbering convention for boundaries is shown below in Figure 3.56.

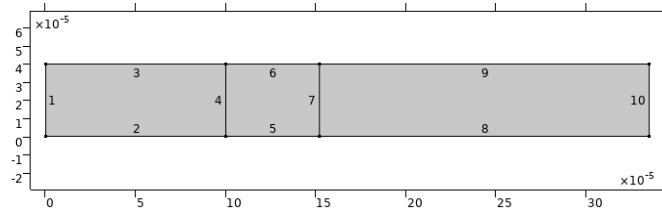


Figure 3.56 2D model, 2d domain boundaries.

Shown below in Figure 3.57 are the three regions for the negative electrode, separator, and positive electrode.

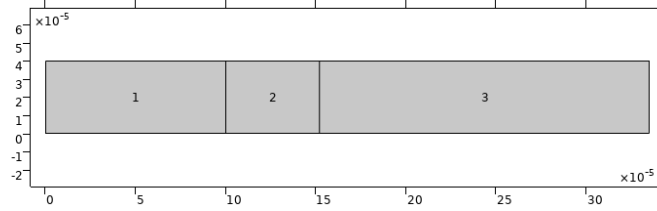


Figure 3.57 2D model, 2d domain regions.

Shown below in Figure 3.58 is the mesh used for the two dimensional domain.

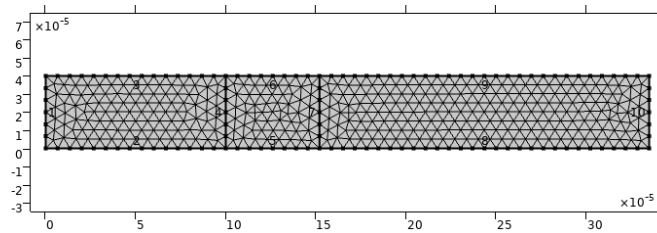


Figure 3.58 2D model, 2d domain mesh.

The mesh used for the domain utilized the pre-built defined Element Size of Extra fine which resulted in 824 domain elements and 126 boundary elements. Shown below in Figure 3.59 is the three dimensional domain used separately for the material balance in the negative electrode solid phase. An exact copy of it was used for the material balance in the positive electrode solid phase.

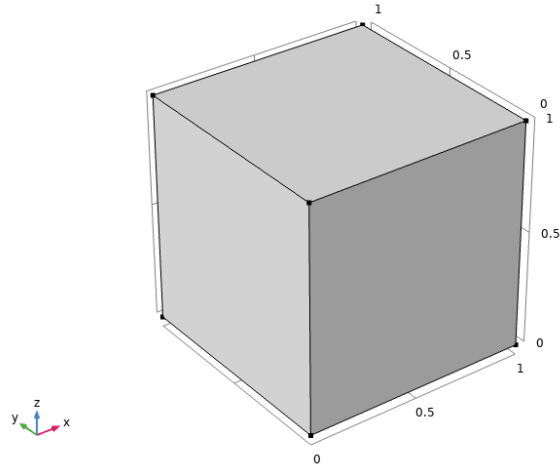


Figure 3.59 2D model, three dimensional domain.

To apply different fluxes on the boundaries of the domain, the numbering convention shown in Figure 3.60 was used.

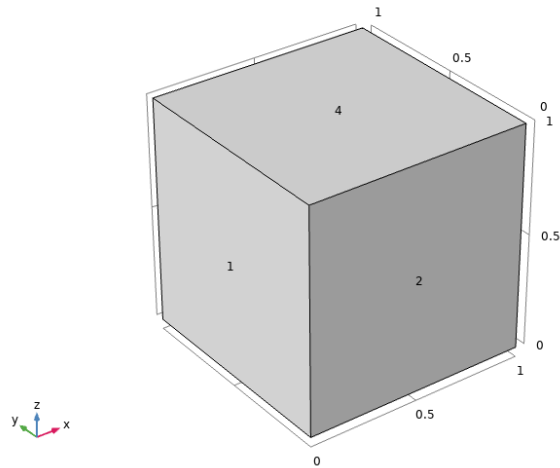


Figure 3.60 2D model, 3d domain boundaries.

Face 1, 2, and 4 are shown. Face 3 is the bottom face, face 5 is opposite of face 2, and face 6 is opposite of face 1. A point on face 4 represents the surface of a spherical particle at that point. A point on face 3 represents the center of a spherical particle at that point. Shown below in Figure 3.61 is the mesh used for the three dimensional domain.

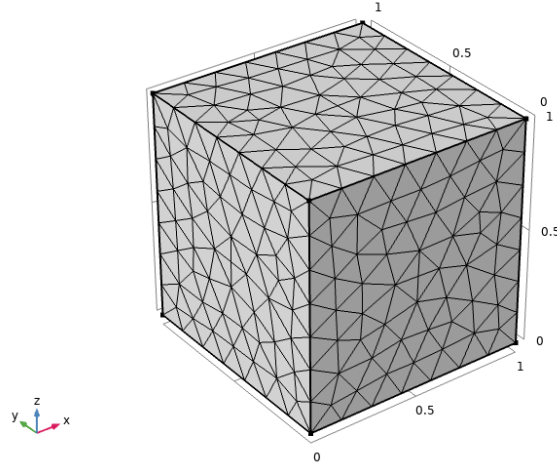


Figure 3.61 2D model, 3d domain mesh.

The mesh used for the domain utilized the pre-built defined Element Size of Coarse which resulted in 4893 domain elements, 744 boundary elements, and 84 edge elements.

3.3.4 Charge Balance Solid Negative

The charge balance in the solid phase of the negative electrode (CBSN) was applied to region 1 shown below in Figure 3.62.

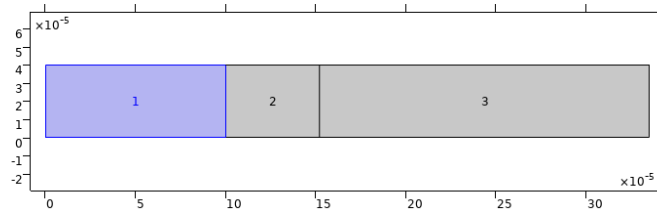


Figure 3.62 2D model, cbsn region.

The General Form PDE in the Mathematics-PDE Interfaces was used to implement the partial differential equation described in equation (2.9) to solve for $\varphi_{s,neg}$. The General Form PDE equation is shown below

$$f = e_a \frac{\partial^2 u}{\partial t^2} + d_a \frac{\partial u}{\partial t} + \nabla \cdot \Gamma \quad (3.91)$$

where f is the source term, e_a is the mass coefficient, u is the dependent variable, d_a is the damping or mass coefficient, $\nabla = \frac{\partial}{\partial x}, \frac{\partial}{\partial y}$, and Γ is the conservative flux. Matching like coefficients between equations (2.9) and (3.91), results in the relations shown below in Table 3.25.

Table 3.25 2D Model, CBSN Parameters

General Form	Value
f	$\dot{I}l_{i,neg}$
e_a	0
d_a	0
Γ_x	$\sigma_{eff,neg} \frac{\partial}{\partial x} \varphi_{s,neg}$
Γ_y	$\sigma_{eff,neg} \frac{\partial}{\partial y} \varphi_{s,neg}$

The effective electrical conductivity used in the conservative flux in equation (3.91), $\sigma_{eff,neg}$, was set equal to σ_{neg} as in there was no Bruggeman correction used. Shown below is this relationship

$$\begin{aligned}
 \sigma_{eff,neg} &= \sigma_{neg} \\
 \text{where} & \\
 \sigma_{eff,neg} &= \text{Effective electrical conductivity} \\
 \sigma_{neg} &= \text{Electrical conductivity}
 \end{aligned}
 \tag{3.92}$$

where $\sigma_{eff,neg}$ is the effective electrical conductivity and σ_{neg} is the electrical conductivity. Within the General Form PDE interface an Initial Value subnode was created. Within this subnode, the region shown in Figure 3.62 was selected, and the initial value for $\varphi_{s,neg}$ was set to 0 as shown below

$$\varphi_{s,neg}(x, y, 0) = 0 \quad (3.93)$$

where $\varphi_{s,neg}$ is the potential in the solid negative electrode. Then within the interface a Dirichlet Boundary Condition subnode was created. The leftmost boundary shown in Figure 3.63 was selected and the value of $\varphi_{s,neg}$ was set to 0 as shown below

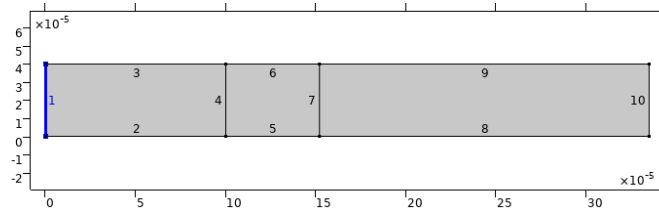


Figure 3.63 2D model, cbsn zero value boundary.

$$\varphi_{s,neg}(0, y, t) = 0 \quad (3.94)$$

where $\varphi_{s,neg}$ is the potential in the solid negative electrode. The flux at the boundary between the negative electrode and the separator shown in Figure 3.64, the boundary labeled 3, and the boundary labeled 2 was set to 0. The equation used for the Zero Flux subnode is shown below

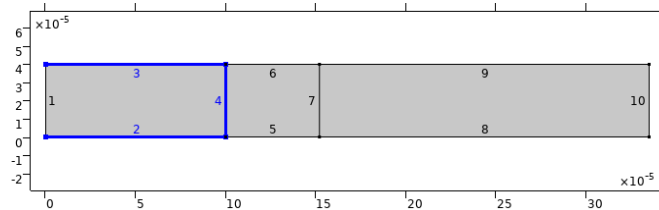


Figure 3.64 2d model, cbsn zero flux boundaries.

$$-n \cdot \Gamma = 0 \quad (3.95)$$

where n is the normal vector and Γ is the conservative flux.

3.3.5 Charge Balance Solid Positive

The charge balance in the solid phase of the positive electrode (CBSP) was applied to region 3 shown below in Figure 3.65.

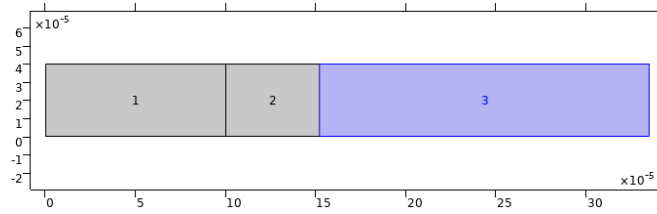


Figure 3.65 2D model, cbsp region.

The General Form PDE in the Mathematics-PDE Interfaces was used to implement the partial differential equation described in equation (2.9) to solve for $\varphi_{s,pos}$. The General Form PDE equation is shown below

$$f = e_a \frac{\partial^2 u}{\partial t^2} + d_a \frac{\partial u}{\partial t} + \nabla \cdot \Gamma \quad (3.96)$$

where f is the source term, e_a is the mass coefficient, u is the dependent variable, d_a is the damping or mass coefficient, $\nabla = \frac{\partial}{\partial x}, \frac{\partial}{\partial y}$, and Γ is the conservative flux. Matching like coefficients between equations (2.9) and (3.96), results in the relations shown below in Table 3.26.

Table 3.26 2D Model, CBSP Parameters

General Form	Value
f	$j_{li,pos}$
e_a	0
d_a	0
Γ_x	$\sigma_{eff,pos} \frac{\partial}{\partial x} \varphi_{s,pos}$
Γ_y	$\sigma_{eff,pos} \frac{\partial}{\partial y} \varphi_{s,pos}$

The effective electrical conductivity used in the conservative flux in equation (3.96), $\sigma_{eff,pos}$, was set equal to σ_{pos} as in there was no Bruggeman correction used. Shown below is this relationship

$$\sigma_{eff,pos} = \sigma_{pos} \quad (3.97)$$

$\sigma_{eff,pos}$ is the effective electrical conductivity and σ_{pos} is the electrical conductivity. Within the General Form PDE interface an Initial Value subnode was created. Within this subnode, the region shown in Figure 3.65 was selected, and the initial value for $\varphi_{s,pos}$ was set to the voltage difference between the equilibrium voltage at the positive electrode and the equilibrium voltage at the negative electrode at the initial concentrations in each respective electrode shown below

$$\varphi_{s,pos}(x, y, 0) = U_{pos} \left(\frac{c_{s0,pos}}{c_{s,pos,max}} \right) - U_{neg} \left(\frac{c_{s0,neg}}{c_{s,neg,max}} \right) \quad (3.98)$$

where $\varphi_{s,pos}$ is the potential in the solid positive electrode, U_{pos} is the positive equilibrium

voltage, $c_{s0,pos}$ is the initial concentration in the solid positive electrode, $c_{s,pos,max}$ is the maximum concentration in the solid positive electrode, U_{neg} is the negative equilibrium voltage, $c_{s0,neg}$ is the initial concentration in the solid negative electrode, and $c_{s,neg,max}$ is the maximum concentration in the solid negative electrode. Next the flux at the boundary between the positive electrode and the separator as shown in Figure 3.66, the boundary labeled 8, and the boundary labeled 9 were set to 0. The equation used for the Zero Flux subnode is shown below

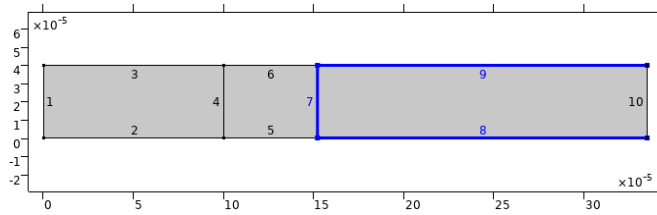


Figure 3.66 2D model, cbsp zero flux boundaries.

$$-n \cdot \Gamma = 0 \quad (3.99)$$

where n is the normal vector and Γ is the conservative flux. Finally within the interface a Flux/Source subnode was created. The equation used for the Flux/Source subnode is shown below

$$-n \cdot \Gamma = g - qu \quad (3.100)$$

where n is the normal vector, Γ is the conservative flux, g is the boundary flux/source, q is the boundary absorption/impedance term, and u is the dependent variable. This flux is for the current density on the rightmost positive electrode boundary shown in Figure 3.67.

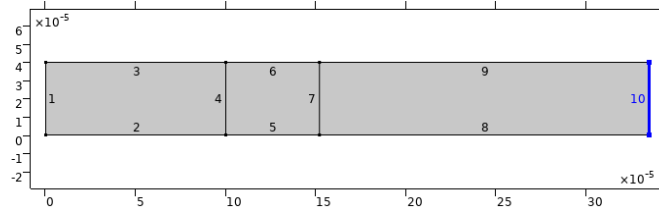


Figure 3.67 2D model, cbsp applied current boundary.

Matching like coefficients between equations (2.8) and (3.100), results in the relations shown below in Table 3.27. With the convention that the negative of the normal vector is pointing into the domain, a positive applied current means that the vector would be pointing into the domain and the current would be moving to the left.

Table 3.27 2D Model, CBSP Flux/Source

Flux/Source	Value
g	I_{app}
q	0

3.3.6 Charge Balance Electrolyte Negative

The charge balance in the electrolyte phase of the negative electrode (CBEN) was applied to region 1 shown below in Figure 3.68.

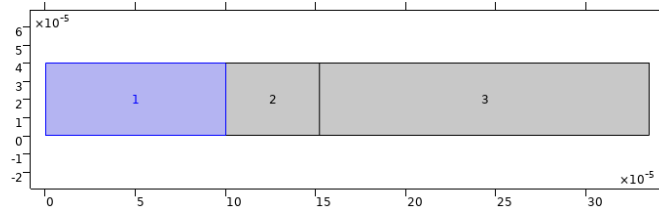


Figure 3.68 2D model, cben region.

The General Form PDE in the Mathematics-PDE Interfaces was used to implement the partial differential equation described in equation (2.7) to solve for $\varphi_{e,neg}$. The General Form PDE equation is shown below

$$f = e_a \frac{\partial^2 u}{\partial t^2} + d_a \frac{\partial u}{\partial t} + \nabla \cdot \Gamma \quad (3.101)$$

where f is the source term, e_a is the mass coefficient, u is the dependent variable, d_a is the damping or mass coefficient, $\nabla = \frac{\partial}{\partial x}, \frac{\partial}{\partial y}$, and Γ is the conservative flux. Matching like coefficients between equations (2.7) and (3.101), results in the relations shown below in Table 3.28.

Table 3.28 2D Model, CBEN Parameters

General Form	Value
f	$-\dot{J}_{i,neg}$
e_a	0
d_a	0
Γ_x	$\kappa^{eff,neg} \frac{\partial}{\partial x} \varphi_{e,neg} + \kappa_{d,neg}^{eff,neg} \frac{\partial}{\partial x} \frac{\frac{\partial C_{e,neg}}{\partial x}}{C_{e,neg}}$
Γ_y	$\kappa^{eff,neg} \frac{\partial}{\partial y} \varphi_{e,neg} + \kappa_{d,neg}^{eff,neg} \frac{\partial}{\partial y} \frac{\frac{\partial C_{e,neg}}{\partial y}}{C_{e,neg}}$

The effective ionic conductivity used in the conservative flux in equation (3.101), $\kappa^{eff,neg}$, was set equal to $\kappa_{neg}(\epsilon_{e,neg})^{brugg}$ as in there is Bruggeman correction used. Shown below is this relationship

$$\kappa^{eff,neg} = \kappa_{neg}(\epsilon_{e,neg})^{brugg} \quad (3.102)$$

where $\kappa^{eff,neg}$ is the effective electrical ionic conductivity, κ_{neg} is the graph in Figure 3.3, $\epsilon_{e,neg}$ is the negative electrolyte phase volume fraction, and $brugg$ is the Bruggeman correction coefficient. The effective diffusion coefficient used in the conservative flux in equation

(3.101), $\kappa_{d,neg}^{eff,neg}$, was set equal to $\frac{2RT}{F}(t_+ - 1)\kappa_{neg}(\epsilon_{e,neg})^{brugg}$ as in there is Bruggeman correction used. Shown below is this relationship

$$\kappa_{d,neg}^{eff,neg} = \frac{2RT}{F}(t_+ - 1)\kappa_{neg}(\epsilon_{e,neg})^{brugg} \quad (3.103)$$

where $\kappa_{d,neg}^{eff,neg}$ is the effective diffusion coefficient, R is the universal gas constant, T is temperature, F is Faraday's constant, t_+ is the transference number, κ_{neg} is the graph in 3.3, $\epsilon_{e,neg}$ is the negative electrolyte phase volume fraction, and $brugg$ is the bruggeman correction coefficient. Within the General Form PDE interface an Initial Value subnode was created. Within this subnode, the region shown in Figure 3.68 was selected, and the initial value for $\varphi_{e,neg}$ was set to $-U_{neg}$ as shown below

$$\varphi_{e,neg}(x, y, 0) = -U_{neg} \left(\frac{C_{s0,neg}}{C_{s,neg,max}} \right) \quad (3.104)$$

where $\varphi_{s,neg}$ is the potential in the electrolyte in the negative electrode, U_{neg} is the negative equilibrium voltage, $C_{s0,neg}$ is the initial concentration in the solid negative electrode, and $C_{s,neg,max}$ is the maximum concentration in the solid negative electrode. Then within the interface a Dirichlet Boundary Condition subnode was created. The boundary between the negative electrode and the separator shown in Figure 3.69 was selected and the value of $\varphi_{e,neg}$ was set equal to $\varphi_{e,sep}$ as shown below to maintain continuity

$$\varphi_{e,neg}(L_{neg}, y, t) = \varphi_{e,sep}(L_{neg}, y, t) \quad (3.105)$$

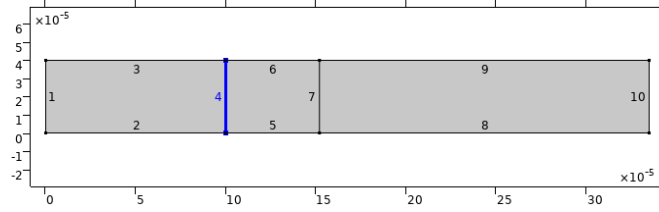


Figure 3.69 2D model, cben dirichlet/flux boundary.

where $\varphi_{e,neg}$ is the potential in the negative electrode and $\varphi_{e,sep}$ is the potential in the separator electrolyte. Next the flux at the leftmost boundary shown in Figure 3.70, the boundary labeled 2, and the boundary labeled 3 were set to 0. The equation used for the Zero Flux subnode is shown below

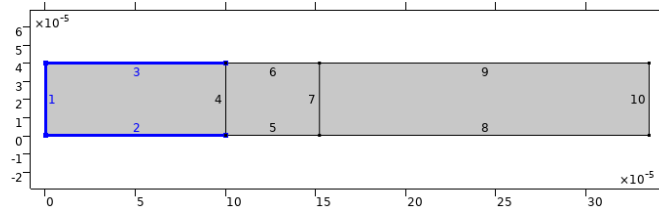


Figure 3.70 2D model, cben zero flux boundaries.

$$-n \cdot \Gamma = 0 \quad (3.106)$$

where n is the normal vector and Γ is the conservative flux. Finally within the interface a Flux/Source subnode was created. The equation used for the Flux/Source subnode is shown below

$$-n \cdot \Gamma = g - qu \quad (3.107)$$

where n is the normal vector, Γ is the conservative flux, g is the boundary flux/source,

q is the boundary absorption/impedance term, and u is the dependent variable. This flux is for continuity between the negative electrode and separator at the boundary shown in Figure 3.69. Matching like coefficients between equations (2.8) and (3.107), results in the relations shown below in Table 3.29. With the convention that the negative of the normal vector is pointing into the domain, a negative flux means that the vector would be pointing out of the domain and the potential would be moving to the right.

Table 3.29 2D Model, CBEN Flux/Source

Flux/Source	Value
g	$-\left(\kappa^{eff,sep} \frac{\partial}{\partial x} \varphi_{e,sep} + \kappa_{d,sep}^{eff,sep} \frac{\partial}{\partial x} \frac{\partial C_{e,sep}}{C_{e,sep}} \right)$
q	0

3.3.7 Charge Balance Electrolyte Separator

The charge balance in the electrolyte phase of the separator (CBES) was applied to region 2 shown below in Figure 3.71.

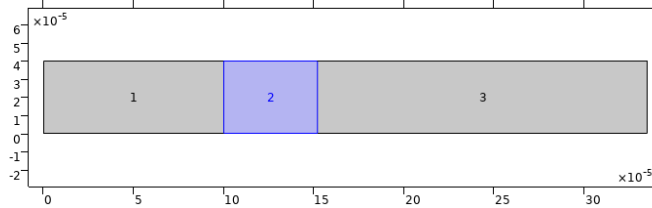


Figure 3.71 2D model, cbes region.

The General Form PDE in the Mathematics-PDE Interfaces was used to implement the partial differential equation described in equation (2.7) to solve for $\varphi_{e,sep}$. The General Form PDE equation is shown below

$$f = e_a \frac{\partial^2 u}{\partial t^2} + d_a \frac{\partial u}{\partial t} + \nabla \cdot \Gamma \quad (3.108)$$

where f is the source term, e_a is the mass coefficient, u is the dependent variable, d_a is the damping or mass coefficient, $\nabla = \frac{\partial}{\partial x}, \frac{\partial}{\partial y}$, and Γ is the conservative flux. Matching like coefficients between equations (2.7) and (3.108), results in the relations shown below in Table 3.30.

Table 3.30 2D Model, CBES Parameters

General Form	Value
f	0
e_a	0
d_a	0
Γ_x	$\kappa^{eff,sep} \frac{\partial}{\partial x} \varphi_{e,sep} + \kappa_{d,sep}^{eff,sep} \frac{\partial}{\partial x} \frac{\frac{\partial C_{e,sep}}{\partial x}}{C_{e,sep}}$
Γ_y	$\kappa^{eff,sep} \frac{\partial}{\partial y} \varphi_{e,sep} + \kappa_{d,sep}^{eff,sep} \frac{\partial}{\partial y} \frac{\frac{\partial C_{e,sep}}{\partial y}}{C_{e,sep}}$

The effective ionic conductivity used in the conservative flux in equation (3.108), $\kappa^{eff,sep}$, was set equal to $\kappa_{sep}(\epsilon_{e,sep})^{brugg}$ as in there is Bruggeman correction used. Shown below is this relationship

$$\kappa^{eff,sep} = \kappa_{sep}(\epsilon_{e,sep})^{brugg} \quad (3.109)$$

where $\kappa^{eff,sep}$ is the effective electrical ionic conductivity, κ_{sep} is the graph in Figure 3.3, $\epsilon_{e,sep}$ is the separator electrolyte phase volume fraction, and $brugg$ is the Bruggeman correction coefficient. The effective diffusion coefficient used in the conservative flux in equation (3.108), $\kappa_{d,sep}^{eff,sep}$, was set equal to $\frac{2RT}{F}(t_+ - 1)\kappa_{sep}(\epsilon_{e,sep})^{brugg}$ as in there is Bruggeman correction used. Shown below is this relationship

$$\kappa_{d,sep}^{eff,sep} = \frac{2RT}{F}(t_+ - 1)\kappa_{sep}(\epsilon_{e,sep})^{brugg} \quad (3.110)$$

where $\kappa_{d,sep}^{eff,sep}$ is the effective diffusion coefficient, R is the universal gas constant, T is temperature, F is Faraday's constant, t_+ is the transference number, κ_{neg} is the graph in 3.3, $\epsilon_{e,sep}$ is the separator electrolyte phase volume fraction, and $brugg$ is the Bruggeman correction coefficient. Within the General Form PDE interface an Initial Value subnode was created. Within this subnode, the region shown in Figure 3.71 was selected, and the initial value for $\varphi_{e,sep}$ was set to $-U_{neg}$ shown below

$$\varphi_{e,sep}(x, y, 0) = -U_{neg} \left(\frac{c_{s0,neg}}{c_{s,neg,max}} \right) \quad (3.111)$$

where φ_{sep} is the potential in the electrolyte in the separator electrode, U_{neg} is the negative equilibrium voltage, $c_{s0,neg}$ is the initial concentration in the solid negative electrode, and $c_{s,neg,max}$ is the maximum concentration in the solid negative electrode. Then within the interface a Dirichlet Boundary Condition subnode was created. The boundary between the separator and the negative electrode shown in Figure 3.72 was selected and the value of $\varphi_{e,sep}$ was set equal to $\varphi_{e,neg}$ to maintain continuity as shown below

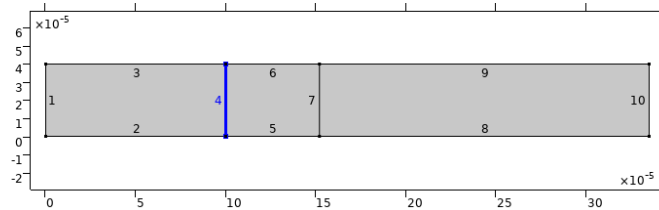


Figure 3.72 2D model, cbes dirichlet/flux boundary 1.

$$\varphi_{e,sep}(L_{neg}, y, t) = \varphi_{e,neg}(L_{neg}, y, t) \quad (3.112)$$

where $\varphi_{e,sep}$ is the potential in the separator electrolyte and $\varphi_{e,neg}$ is the potential in the negative electrolyte. After that within the interface an additional Dirichlet Boundary Condition subnode was created. The boundary between the separator and the positive electrode as shown in Figure 3.73 was selected and the value of $\varphi_{e,sep}$ was set equal to $\varphi_{e,pos}$ to maintain continuity as shown below

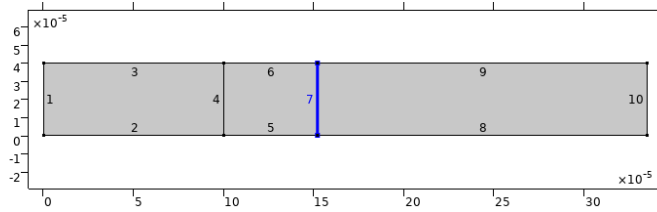


Figure 3.73 2D model, cbes dirichlet/flux boundary 2.

$$\varphi_{e,sep}\left((L_{neg} + L_{sep}), y, t\right) = \varphi_{e,pos}\left((L_{neg} + L_{sep}), y, t\right) \quad (3.113)$$

where $\varphi_{e,sep}$ is the potential in the separator electrolyte and $\varphi_{e,pos}$ is the potential in the positive electrolyte. Next the flux at the boundaries shown in Figure 3.74 were set to 0.

The equation used for the Zero Flux subnode is shown below

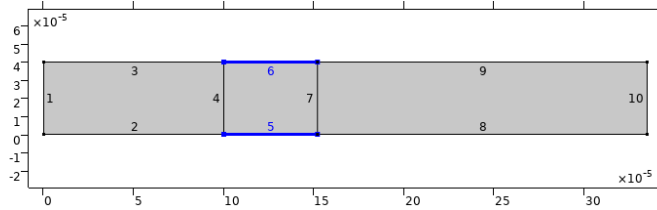


Figure 3.74 2D model, cbes zero flux boundaries.

$$-n \cdot \Gamma = 0 \quad (3.114)$$

where n is the normal vector and Γ is the conservative flux. Finally within the interface a Flux/Source subnode was created. Next within the interface a Flux/Source subnode was created. The equation used for the Flux/Source subnode is shown below

$$-n \cdot \Gamma = g - qu \quad (3.115)$$

where n is the normal vector, Γ is the conservative flux, g is the boundary flux/source, q is the boundary absorption/impedance term, and u is the dependent variable. This flux is for continuity between the separator and negative electrode at the boundary as shown in Figure 3.72. Matching like coefficients between equations (2.8) and (3.115), results in the relations shown below in Table 3.31. With the convention that the negative of the normal vector is pointing into the domain, a positive flux means that the vector would be pointing into the domain and the potential would be moving to the right.

Table 3.31 2D Model, CBES Flux/Source 1

Flux/Source	Value
g	$\left(\kappa^{eff,neg} \frac{\partial}{\partial x} \varphi_{e,neg} + \kappa_{d,neg}^{eff} \frac{\partial}{\partial x} \frac{\frac{\partial C_{e,neg}}{\partial x}}{C_{e,neg}} \right)$
q	0

Finally within the interface an additional Flux/Source subnode was created. The equation used for the Flux/Source subnode is shown below

$$-n \cdot \Gamma = g - qu \tag{3.116}$$

where n is the normal vector, Γ is the conservative flux, g is the boundary flux/source, q is the boundary absorption/impedance term, and u is the dependent variable. This flux is for continuity between the separator and positive electrode at the boundary as shown in Figure 3.73. Matching like coefficients between equations (2.8) and (3.116), results in the relations shown below in Table 3.32. With the convention that the negative of the normal vector is pointing into the domain, a negative flux means that the vector would be pointing out of the domain and the potential would be moving to the right.

Table 3.32 2D Model, CBES Flux/Source 2

Flux/Source	Value
g	$-\left(\kappa^{eff,pos} \frac{\partial}{\partial x} \varphi_{e,pos} + \kappa_{d,pos}^{eff} \frac{\partial}{\partial x} \frac{\partial C_{e,pos}}{C_{e,pos}} \right)$
q	0

3.3.8 Charge Balance Electrolyte Positive

The charge balance in the electrolyte phase of the positive electrode (CBEP) was applied to region 3 shown below in Figure 3.75.

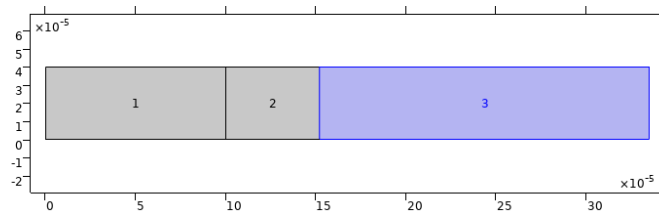


Figure 3.75 2D model, cbep region.

The General Form PDE in the Mathematics-PDE Interfaces was used to implement

the partial differential equation described in equation (2.7) to solve for $\varphi_{e,pos}$. The General Form PDE equation is shown as

$$f = e_a \frac{\partial^2 u}{\partial t^2} + d_a \frac{\partial u}{\partial t} + \nabla \cdot \Gamma \quad (3.117)$$

where f is the source term, e_a is the mass coefficient, u is the dependent variable, d_a is the damping or mass coefficient, $\nabla = \frac{\partial}{\partial x}, \frac{\partial}{\partial y}$, and Γ is the conservative flux. Matching like coefficients between equations (2.7) and (3.117), results in the relations shown below in Table 3.33.

Table 3.33 2D Model, CBEP Parameters

General Form	Value
f	$-j_{li,pos}$
e_a	0
d_a	0
Γ_x	$\kappa^{eff,pos} \frac{\partial}{\partial x} \varphi_{e,pos} + \kappa_{d,pos}^{eff,pos} \frac{\partial}{\partial x} \frac{\frac{\partial C_{e,pos}}{\partial x}}{C_{e,pos}}$
Γ_y	$\kappa^{eff,pos} \frac{\partial}{\partial y} \varphi_{e,pos} + \kappa_{d,pos}^{eff,pos} \frac{\partial}{\partial y} \frac{\frac{\partial C_{e,pos}}{\partial y}}{C_{e,pos}}$

The effective ionic conductivity used in the conservative flux in equation (3.117), $\kappa^{eff,pos}$, was set equal to $\kappa_{pos}(\epsilon_{e,pos})^{brugg}$ as in there is Bruggeman correction used. Shown below is this relationship

$$\kappa^{eff,pos} = \kappa_{pos}(\epsilon_{e,pos})^{brugg} \quad (3.118)$$

where $\kappa^{eff,pos}$ is the effective electrical ionic conductivity, κ_{pos} is the graph in Figure 3.3,

$\epsilon_{e,pos}$ is the positive electrolyte phase volume fraction, and *brugg* is the Bruggeman correction coefficient. The effective diffusion coefficient used in the conservative flux in equation (3.117), $\kappa_{d,pos}^{eff,pos}$, was set equal to $\frac{2RT}{F}(t_+ - 1)\kappa_{pos}(\epsilon_{e,pos})^{brugg}$ as in there is Bruggeman correction used. Shown below is this relationship

$$\kappa_{d,pos}^{eff,pos} = \frac{2RT}{F}(t_+ - 1)\kappa_{pos}(\epsilon_{e,pos})^{brugg} \quad (3.119)$$

where $\kappa_{d,pos}^{eff,pos}$ is the effective diffusion coefficient, R is the universal gas constant, T is temperature, F is Faraday's constant, t_+ is the transference number, κ_{neg} is the graph in 3.3, $\epsilon_{e,pos}$ is the positive electrolyte phase volume fraction, and *brugg* is the bruggeman correction coefficient. Within the General Form PDE interface an Initial Value subnode was created. Within this subnode, the region shown in Figure 3.75 was selected, and the initial value for $\varphi_{e,pos}$ was set to $-U_{neg}$ shown below

$$\varphi_{e,pos}(x, y, 0) = -U_{neg} \left(\frac{C_{s0,neg}}{C_{s,neg,max}} \right) \quad (3.120)$$

where φ_{pos} is the potential in the electrolyte in the positive electrode, U_{neg} is the negative equilibrium voltage, $C_{s0,neg}$ is the initial concentration in the solid negative electrode, and $C_{s,neg,max}$ is the maximum concentration in the solid negative electrode. Then within the interface a Dirichlet Boundary Condition subnode was created. The boundary between the positive electrode and the separator shown in Figure 3.76 was selected and the value of $\varphi_{e,pos}$ was set equal to $\varphi_{e,sep}$ as shown below to maintain continuity

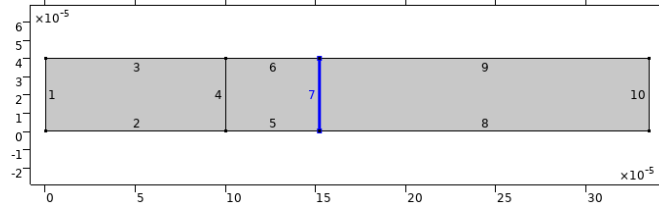


Figure 3.76 2D model, cbep dirichlet/flux boundary.

$$\varphi_{e,pos} \left((L_{neg} + L_{sep}), y, t \right) = \varphi_{e,sep} \left((L_{neg} + L_{sep}), y, t \right) \quad (3.121)$$

where $\varphi_{e,pos}$ is the potential in the positive electrolyte and $\varphi_{e,neg}$ is the potential in the separator electrolyte. Next the flux at the rightmost boundary as shown in Figure 3.77, the boundary labeled 8, and the boundary labeled 9 were set to 0. The equation used for the Zero Flux subnode is shown as

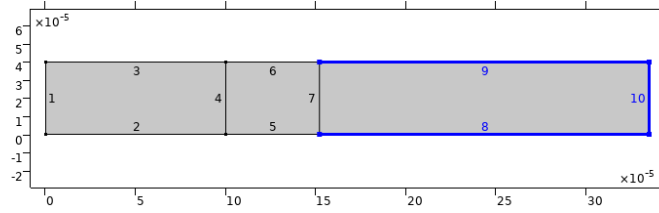


Figure 3.77 2D model, cbep zero flux boundaries.

$$-n \cdot \Gamma = 0 \quad (3.122)$$

where n is the normal vector and Γ is the conservative flux. Finally within the interface a Flux/Source subnode was created. The equation used for the Flux/Source subnode is shown below

$$-n \cdot \Gamma = g - qu \tag{3.123}$$

where n is the normal vector, Γ is the conservative flux, g is the boundary flux/source, q is the boundary absorption/impedance term, and u is the dependent variable. This flux is for continuity between the positive electrode and separator at the boundary shown in Figure 3.76. Matching like coefficients between equations (2.8) and (3.123), results in the relations shown below in Table 3.34. With the convention that the negative of the normal vector is pointing into the domain, a positive flux means that the vector would be pointing into the domain and the potential would be moving to the right.

Table 3.34 2D Model, CBEP Flux/Source

Flux/Source	Value
g	$\left(\kappa^{eff,sep} \frac{\partial}{\partial x} \varphi_{e,sep} + \kappa_{d,sep}^{eff,sep} \frac{\partial}{\partial x} \frac{\partial C_{e,sep}}{C_{e,sep}} \right)$
q	0

3.3.9 Material Balance Electrolyte Negative

The material balance in the electrolyte phase of the negative electrode (MBEN) was applied to region 1 shown below in Figure 3.78.

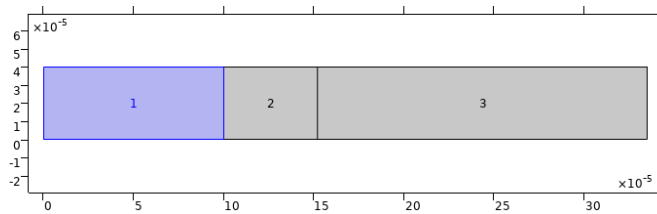


Figure 3.78 2D model, mben region.

The General Form PDE in the Mathematics-PDE Interfaces was used to implement

the partial differential equation described in equation (2.3) to solve for $C_{e,neg}$. The General Form PDE equation is shown as

$$f = e_a \frac{\partial^2 u}{\partial t^2} + d_a \frac{\partial u}{\partial t} + \nabla \cdot \Gamma \quad (3.124)$$

where f is the source term, e_a is the mass coefficient, u is the dependent variable, d_a is the damping or mass coefficient, $\nabla = \frac{\partial}{\partial x}, \frac{\partial}{\partial y}$, and Γ is the conservative flux. Matching like coefficients between equations (2.3) and (3.124), results in the relations shown below in Table 3.35.

Table 3.35 2D Model, MBEN Parameters

General Form	Value
f	$\frac{j_{i,neg}(1-t_+)}{F}$
e_a	0
d_a	$\epsilon_{e,neg}$
Γ_x	$-D_{e,neg}^{eff} \frac{\partial C_{e,neg}}{\partial x}$
Γ_y	$-D_{e,neg}^{eff} \frac{\partial C_{e,neg}}{\partial y}$

The diffusion coefficient used in the conservative flux in equation (3.124), $D_{e,neg}^{eff}$, was set equal to $D_{e,neg}(\epsilon_{e,neg})^{brugg}$ as in there is Bruggeman correction used. Shown below is this relationship

$$D_{e,neg}^{eff} = D_{e,neg}(\epsilon_{e,neg})^{brugg} \quad (3.125)$$

where $D_{e,neg}^{eff}$ is the effective diffusion coefficient, $D_{e,neg}$ is the diffusion coefficient, $\epsilon_{e,neg}$

is the negative electrolyte phase volume fraction, and *brugg* is the Bruggeman correction coefficient. Within the General Form PDE interface an Initial Value subnode was created. Within this subnode, the region shown in Figure 3.78 was selected, and the initial value for $C_{e,neg}$ was set to c_{l0} as

$$C_{e,neg}(x, y, 0) = c_{l0} \quad (3.126)$$

where $C_{e,neg}$ is the concentration in the electrolyte in the negative electrode and c_{l0} is the initial concentration. Then within the interface a Dirichlet Boundary Condition subnode was created. The boundary between the negative electrode and the separator shown in Figure 3.79 was selected and the value of $C_{e,neg}$ was set equal to $C_{e,sep}$ as shown below to maintain continuity

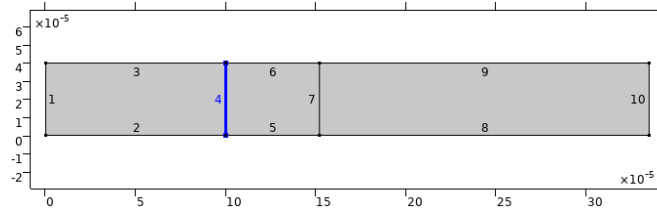


Figure 3.79 2D model, mben dirichlet/flux boundary.

$$C_{e,neg}(L_{neg}, y, t) = C_{e,sep}(L_{neg}, y, t) \quad (3.127)$$

where $C_{e,neg}$ is the concentration in the negative electrolyte and $C_{e,sep}$ is the concentration in the separator electrolyte. Next the flux at the leftmost boundary shown in Figure 3.80, the boundary labeled 2, and the boundary labeled 3 were set to 0. The equation used for the Zero Flux subnode is shown below

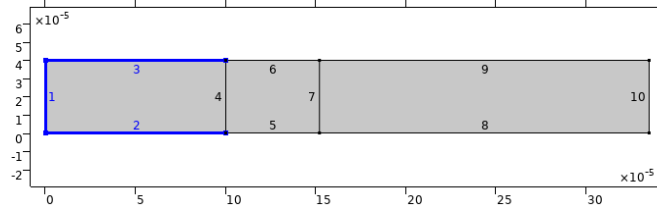


Figure 3.80 2D model, mben zero flux boundaries.

$$-n \cdot \Gamma = 0 \quad (3.128)$$

where n is the normal vector and Γ is the conservative flux. Finally within the interface a Flux/Source subnode was created. The equation used for the Flux/Source subnode is shown below

$$-n \cdot \Gamma = g - qu \quad (3.129)$$

where n is the normal vector, Γ is the conservative flux, g is the boundary flux/source, q is the boundary absorption/impedance term, and u is the dependent variable. This flux is for continuity between the negative electrode and separator at the boundary shown in Figure 3.79. Matching like coefficients between equations (2.4) and (3.129), results in the relations shown below in Table 3.36. With the convention that the negative of the normal vector is pointing into the domain, a positive flux means that the vector would be pointing into the domain and the flux would be moving to the left.

Table 3.36 2D Model, MBEN Flux/Source

Flux/Source	Value
g	$D_{e,sep}(\epsilon_{e,sep})^{brugg} \frac{\partial C_{e,sep}}{\partial x}$
q	0

3.3.10 Material Balance Electrolyte Separator

The material balance in the electrolyte phase of the separator (MBES) was applied to region 2 shown below in Figure 3.81.

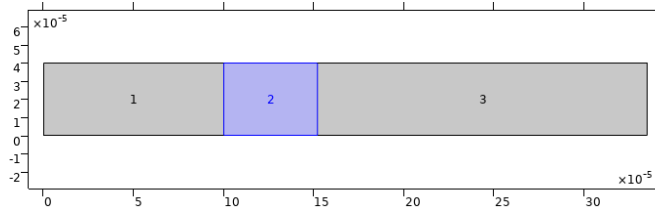


Figure 3.81 2D model, mbes region.

The General Form PDE in the Mathematics-PDE Interfaces was used to implement the partial differential equation described in equation (2.3) to solve for $C_{e,sep}$. The General Form PDE equation is shown as

$$f = e_a \frac{\partial^2 u}{\partial t^2} + d_a \frac{\partial u}{\partial t} + \nabla \cdot \Gamma \quad (3.130)$$

where f is the source term, e_a is the mass coefficient, u is the dependent variable, d_a is the damping or mass coefficient, $\nabla = \frac{\partial}{\partial x}, \frac{\partial}{\partial y}$, and Γ is the conservative flux. Matching like coefficients between equations (2.3) and (3.130), results in the relations shown below in Table 3.37.

Table 3.37 2D Model, MBES Parameters

General Form	Value
f	0
e_a	0
d_a	$\epsilon_{e,sep}$
Γ_x	$-D_{e,sep}^{eff} \frac{\partial C_{e,sep}}{\partial x}$
Γ_y	$-D_{e,sep}^{eff} \frac{\partial C_{e,sep}}{\partial y}$

The diffusion coefficient used in the conservative flux in equation (3.130), $D_{e,sep}^{eff}$, was set equal to $D_{e,sep}(\epsilon_{e,sep})^{brugg}$ as in there is Bruggeman correction used. Shown below is this relationship

$$D_{e,sep}^{eff} = D_{e,sep}(\epsilon_{e,sep})^{brugg} \quad (3.131)$$

where $D_{e,sep}^{eff}$ is the effective diffusion coefficient, $D_{e,sep}$ is the diffusion coefficient, $\epsilon_{e,sep}$ is the separator electrolyte phase volume fraction, and $brugg$ is the Bruggeman correction coefficient. Within the General Form PDE interface an Initial Value subnode was created. Within this subnode, the region shown in Figure 3.81 was selected, and the initial value for $C_{e,sep}$ was set to c_{l0} shown below

$$C_{e,sep}(x, y, 0) = c_{l0} \quad (3.132)$$

where $C_{e,sep}$ is the concentration in the electrolyte in the separator electrode and c_{l0} is the initial concentration. Then within the interface a Dirichlet Boundary Condition subnode

was created. The boundary between the separator and the negative electrode shown in Figure 3.82 was selected and the value of $C_{e,sep}$ was set equal to $C_{e,neg}$ to maintain continuity as shown below

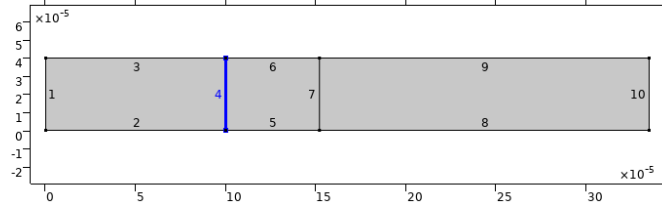


Figure 3.82 2D model, mbes dirichlet/flux boundary 1.

$$C_{e,sep}(L_{neg}, y, t) = C_{e,neg}(L_{neg}, y, t) \quad (3.133)$$

where $C_{e,sep}$ is the concentration in the separator electrolyte and $C_{e,neg}$ is the concentration in the negative electrolyte. Then an additional Dirichlet Boundary Condition subnode was created. The boundary between the separator and the positive electrode as shown in Figure 3.83 was selected and the value of $C_{e,sep}$ was set equal to $C_{e,pos}$ to maintain continuity as shown below

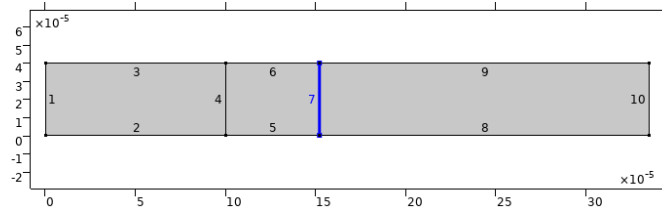


Figure 3.83 2D model, mbes dirichlet/flux boundary 2.

$$C_{e,sep}\left((L_{neg} + L_{sep}), y, t\right) = C_{e,pos}\left((L_{neg} + L_{sep}), y, t\right) \quad (3.134)$$

where $C_{e,sep}$ is the concentration in the separator electrolyte and $C_{e,pos}$ is the concentration in the positive electrolyte. Next the flux at the boundaries shown in Figure 3.84 were set to 0. The equation used for the Zero Flux subnode is shown below

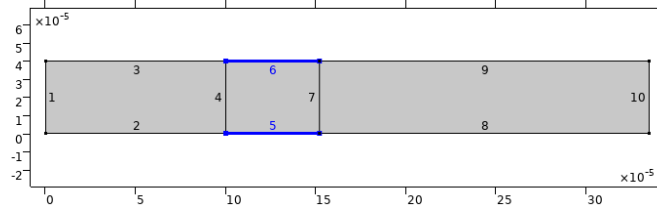


Figure 3.84 2D model, mbes zero flux boundaries.

$$-n \cdot \Gamma = 0 \quad (3.135)$$

where n is the normal vector and Γ is the conservative flux. Then within the interface a Flux/Source subnode was created. The equation used for the Flux/Source subnode is shown below

$$-n \cdot \Gamma = g - qu \quad (3.136)$$

where n is the normal vector, Γ is the conservative flux, g is the boundary flux/source, q is the boundary absorption/impedance term, and u is the dependent variable. This flux is for continuity between the separator and the negative electrode at the boundary as shown in Figure 3.82. Matching like coefficients between equations (2.4 and (3.136), results in the relations shown below in Table 3.38. With the convention that the negative of the normal vector is pointing into the domain, a negative flux means that the vector would be pointing out of the domain and the flux would be moving to the left.

Table 3.38 2D Model, MBES Flux/Source 1

Flux/Source	Value
g	$-D_{e,neg}(\epsilon_{e,neg})^{brugg} \frac{\partial C_{e,neg}}{\partial x}$
q	0

Finally within the interface an additional Flux/Source subnode was created. The equation used for the Flux/Source subnode is shown below

$$-n \cdot \Gamma = g - qu \quad (3.137)$$

where n is the normal vector, Γ is the conservative flux, g is the boundary flux/-source, q is the boundary absorption/impedance term, and u is the dependent variable. This flux is for continuity between the separator and the positive electrode at the boundary as shown in Figure 3.83. Matching like coefficients between equations (2.4) and (3.137,) results in the relations shown below in Table 3.39. With the convention that the negative of the normal vector is pointing into the domain, a positive flux means that the vector would be pointing into the domain and the flux would be moving to the left.

Table 3.39 2D Model, MBES Flux/Source 2

Flux/Source	Value
g	$D_{e,pos}(\epsilon_{e,pos})^{brugg} \frac{\partial C_{e,pos}}{\partial x}$
q	0

3.3.11 Material Balance Electrolyte Positive

The material balance in the electrolyte phase of the positive electrode (MBEP) was applied to region 3 shown below in Figure 3.85.

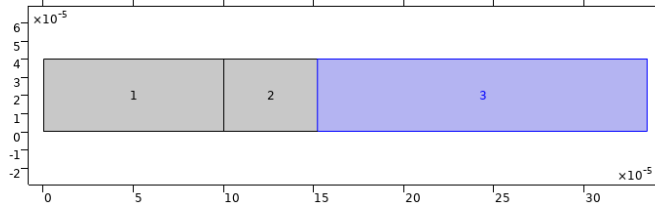


Figure 3.85 2D model, mbep region.

The General Form PDE in the Mathematics-PDE Interfaces was used to implement the partial differential equation described in equation (2.3) to solve for $C_{e, pos}$. The General Form PDE equation is shown below

$$f = e_a \frac{\partial^2 u}{\partial t^2} + d_a \frac{\partial u}{\partial t} + \nabla \cdot \Gamma \quad (3.138)$$

where f is the source term, e_a is the mass coefficient, u is the dependent variable, d_a is the damping or mass coefficient, $\nabla = \frac{\partial}{\partial x}, \frac{\partial}{\partial y}$, and Γ is the conservative flux. Matching like coefficients between equations (2.3) and (3.138), results in the relations shown below in Table 3.40.

Table 3.40 2D Model, MBEP Parameters

General Form	Value
f	$\frac{j_{i,pos}(1-t_+)}{F}$
e_a	0
d_a	$\epsilon_{e,pos}$
Γ_x	$-D_{e,pos}^{eff} \frac{\partial C_{e,pos}}{\partial x}$
Γ_y	$-D_{e,pos}^{eff} \frac{\partial C_{e,pos}}{\partial y}$

The diffusion coefficient used in the conservative flux in equation (3.138), $D_{e,pos}^{eff}$, was set equal to $D_{e,pos}(\epsilon_{e,pos})^{brugg}$ as in there is Bruggeman correction used. Shown below is this relationship

$$D_{e,pos}^{eff} = D_{e,pos}(\epsilon_{e,pos})^{brugg} \quad (3.139)$$

where $D_{e,pos}^{eff}$ is the effective diffusion coefficient, $D_{e,pos}$ is the diffusion coefficient, $\epsilon_{e,pos}$ is the positive electrolyte phase volume fraction, and $brugg$ is the Bruggeman correction coefficient. Within the General Form PDE interface an Initial Value subnode was created. Within this subnode, the region shown in Figure 3.85 was selected, and the initial value for $C_{e,pos}$ was set to c_{l0} as shown below

$$C_{e,pos}(x, y, 0) = c_{l0} \quad (3.140)$$

where $C_{e,pos}$ is the concentration in the electrolyte in the positive electrode and c_{l0} is the initial concentration. Then within the interface a Dirichlet Boundary Condition subnode

was created. The boundary between the positive electrode and the separator shown in Figure 3.86 was selected and the value of $C_{e,pos}$ was set equal to $C_{e,sep}$ as shown below to maintain continuity

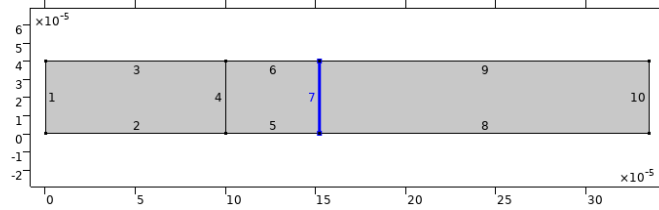


Figure 3.86 2D model, mbep dirichlet/flux boundary.

$$C_{e,pos}\left((L_{neg} + L_{sep}), y, t\right) = C_{e,sep}\left((L_{neg} + L_{sep}), y, t\right) \quad (3.141)$$

where $C_{e,pos}$ is the concentration in the positive electrolyte and $C_{e,sep}$ is the concentration in the separator electrolyte. Next the flux at the rightmost boundary shown in Figure 3.87, the boundary labeled 8, and the boundary labeled 9 were set to 0. The equation used for the Zero Flux subnode is shown below

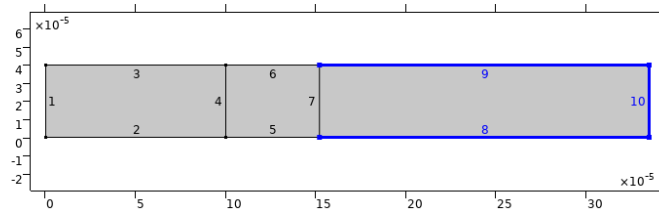


Figure 3.87 2D model, mbep zero flux boundaries.

$$-n \cdot \Gamma = 0 \quad (3.142)$$

where n is the normal vector and Γ is the conservative flux. Finally within the interface a

Flux/Source subnode was created. The equation used for the Flux/Source subnode is shown below

$$-n \cdot \Gamma = g - qu \quad (3.143)$$

where n is the normal vector, Γ is the conservative flux, g is the boundary flux/source, q is the boundary absorption/impedance term, and u is the dependent variable. flux is for continuity between the positive electrode and separator at the boundary shown in Figure 3.86. Matching like coefficients between equations (2.4) and (3.143), results in the relations shown below in Table 3.41. With the convention that the negative of the normal vector is pointing into the domain, a negative flux means that the vector would be pointing out of the domain and the flux would be moving to the left.

Table 3.41 2D Model, MBEP Flux/Source

Flux/Source	Value
g	$-D_{e,sep}(\epsilon_{e,sep})^{brugg} \frac{\partial C_{e,sep}}{\partial x}$
q	0

3.3.12 Material Balance Solid Negative

The material balance in the solid phase of the negative electrode (MBSN) is calculated in its own three dimensional domain. Shown below in Figure 3.88 is the three dimensional domain.

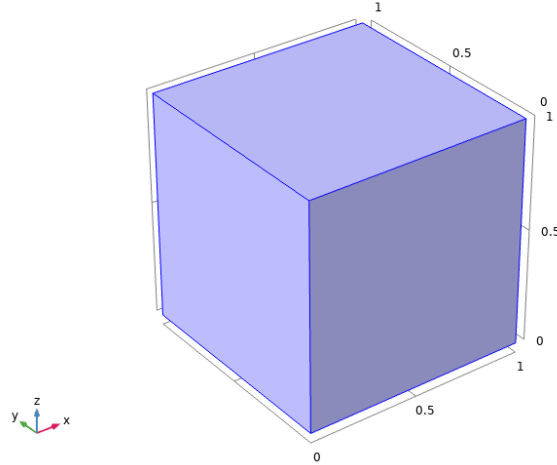


Figure 3.88 2D model, mbsn region.

The General Form PDE in the Mathematics-PDE Interfaces was used to implement the partial differential equation described in equation (2.5) to solve for $C_{s,neg}$. The General Form PDE equation is shown as

$$f = e_a \frac{\partial^2 u}{\partial t^2} + d_a \frac{\partial u}{\partial t} + \nabla \cdot \Gamma \quad (3.144)$$

where f is the source term, e_a is the mass coefficient, u is the dependent variable, d_a is the damping or mass coefficient, $\nabla = \frac{\partial}{\partial x}, \frac{\partial}{\partial y}, \frac{\partial}{\partial z}$, and Γ is the conservative flux. The top boundary shown in Figure 3.89 of the domain is the function that is mapped to the two dimensional domain for the negative electrode. The z -dimension represents the radius of a sphere at that (x,y) value. The top boundary is when z is equal to the radius of the spherical particle ($r = R_p$). The bottom boundary is when z is equal to 0 which represents the center of a spherical particle ($r = 0$).

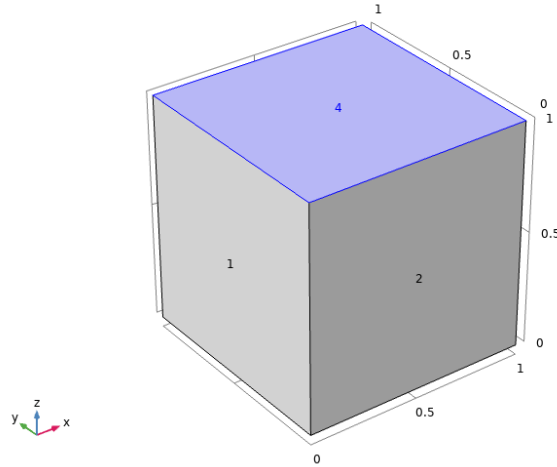


Figure 3.89 2D model, mbsn flux/top boundary.

To avoid division by zero when ($r = 0$), equation (2.5) is multiplied by r^2 . The resulting differential equation is shown below

$$r^2 \frac{\partial C_s}{\partial t} = D_s \frac{\partial}{\partial r} \left(r^2 \frac{\partial C_s}{\partial r} \right) \quad (3.145)$$

where C_s is the concentration in the solid phase and D_s is the diffusion coefficient. After that the equation is scaled in reference to the particle radius. The scaling is done through the relationship shown below

$$\begin{aligned} \hat{r} &= \frac{r}{R_p} \\ \frac{\partial}{\partial r} &= \frac{1}{R_p} \frac{\partial}{\partial \hat{r}} \end{aligned} \quad (3.146)$$

With these changes the new partial differential equation that describes the diffusion of lithium in the solid phase is shown below

$$\hat{r}^2 \frac{\partial C_s}{\partial t} = D_s \frac{\partial}{\partial \hat{r}} \left(\frac{\hat{r}^2}{R_p^2} \frac{\partial C_s}{\partial \hat{r}} \right) \quad (3.147)$$

where C_s is the concentration in the solid phase, D_s is the diffusion coefficient, and R_p is the particle radius. Matching like coefficients between equations (3.147) and (3.144), results in the relations shown below in Table 3.42.

Table 3.42 2D Model, MBSN Parameters

General Form	Value
f	0
e_a	0
d_a	r^2
Γ_x	0
Γ_y	0
Γ_z	$-D_{s,neg} \frac{r^2}{(R_{s,neg})^2} \frac{\partial C_{s,neg}}{\partial r}$

The flux at the surface of the particle would also need to change. Shown below is the adjusted flux at the surface while the other two conditions in equation (3.148) are reiterated as

$$\begin{aligned} -D_s \frac{\partial C_s}{\partial x} \Big|_{r=0} &= 0 \\ -D_s \frac{\partial C_s}{\partial x} \Big|_{r=R_p} &= \frac{\hat{r}^2}{R_p} \frac{j_{li}}{a_s F} \end{aligned} \quad (3.148)$$

$$C_s(x, y, r, 0) = C_s^{init}(r)$$

where R_p is the radius of the particle, j_{li} is the pore-wall flux across the interface, F is Faraday's constant, and a_s is the surface area to volume ratio. Within the General Form PDE interface an Initial Value subnode was created. Within this subnode, the region shown

in Figure 3.88 was selected, and the initial value for $C_{s,neg}$ was set to $c_{s0,neg}$ as shown below

$$C_{s,neg}(x, y, r, 0) = c_{s0,neg} \quad (3.149)$$

where $C_{s,neg}$ is the concentration in the solid negative electrode and $c_{s0,neg}$ is the initial concentration in the solid phase. Next the flux at the faces labelled 1, 2, 3, 5 and 6 as shown in Figure 3.90 were set to zero. The equation used for the Zero Flux subnode is shown below

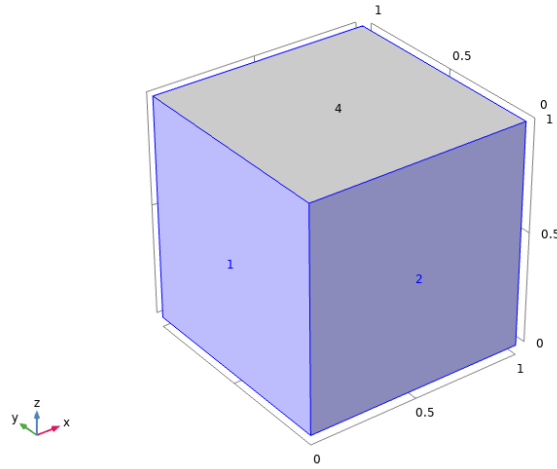


Figure 3.90 2D model, mbsn zero flux boundaries.

$$-n \cdot \Gamma = 0 \quad (3.150)$$

where n is the normal vector and Γ is the conservative flux. Finally within the interface a Flux/Source subnode was created. The equation used for the Flux/Source subnode is shown below

$$-n \cdot \Gamma = g - qu \quad (3.151)$$

where n is the normal vector, Γ is the conservative flux, g is the boundary flux/source, q is the boundary absorption/impedance term, and u is the dependent variable. This flux is for pore-wall flux across the interface on the boundary shown in Figure 3.89. Matching like coefficients between equations (3.148) and (3.151), results in the relations shown below in Table 3.43. With the convention that the negative of the normal vector is pointing into the domain, a negative flux means that the vector would be pointing out of the domain and the flux would be moving to the upwards.

Table 3.43 2D Model, MBSN Flux/Source

Flux/Source	Value
g	$-\frac{r^2}{R_{s,neg}} \frac{j_{li,neg}}{a_{s,neg} F}$
q	0

3.3.13 Material Balance Solid Positive

The material balance in the solid phase of the positive electrode (MBSP) is calculated in its own three dimensional domain. Shown below in Figure 3.91 is the three dimensional domain.

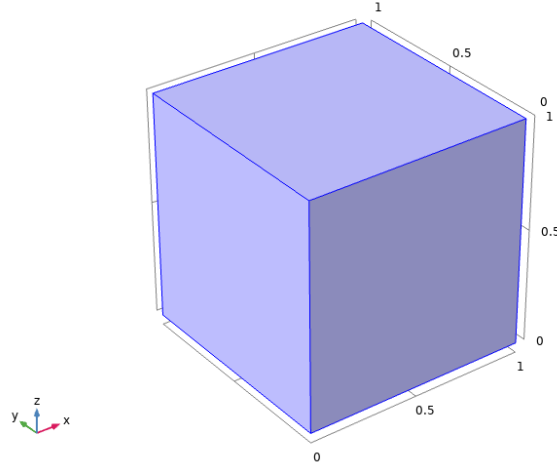


Figure 3.91 2D model, mbsp region.

The General Form PDE in the Mathematics-PDE Interfaces was used to implement the partial differential equation described in equation (3.147) to solve for $C_{s,pos}$. The General Form PDE equation is shown below

$$f = e_a \frac{\partial^2 u}{\partial t^2} + d_a \frac{\partial u}{\partial t} + \nabla \cdot \Gamma \quad (3.152)$$

where f is the source term, e_a is the mass coefficient, u is the dependent variable, d_a is the damping or mass coefficient, $\nabla = \frac{\partial}{\partial x}, \frac{\partial}{\partial y}, \frac{\partial}{\partial z}$, and Γ is the conservative flux. The top boundary shown in Figure 3.92 of the domain is the function that is mapped to the two dimensional domain for the positive electrode. The z-dimension represents the radius of a sphere at that (x,y) value. The top boundary is when z is equal to the radius of the spherical particle ($r = R_p$). The bottom boundary is when z is equal to 0 which represents the center of a spherical particle ($r = 0$).

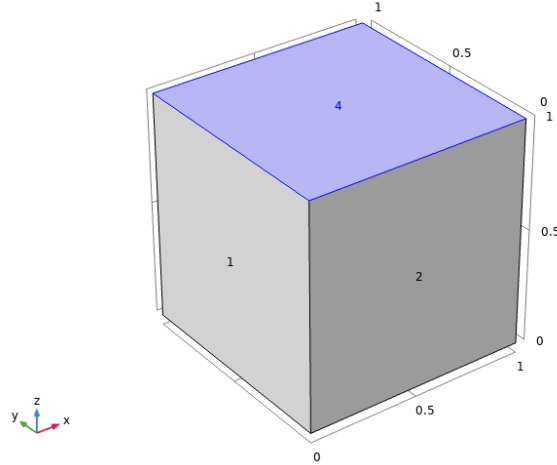


Figure 3.92 2D model, mbsp flux/top boundary.

Matching like coefficients between equations (3.147) and (3.152), results in the relations shown below in Table 3.44.

Table 3.44 2D Model, MBSP Parameters

General Form	Value
f	0
e_a	0
d_a	r^2
Γ_x	0
Γ_y	0
Γ_z	$-D_{s,pos} \frac{r^2}{(R_{s,pos})^2} \frac{\partial C_{s,pos}}{\partial r}$

Within the General Form PDE interface an Initial Value subnode was created. Within this subnode, the region shown in Figure 3.91 was selected, and the initial value for $C_{s,pos}$ was set to $c_{s0,pos}$ as shown below

$$C_{s,pos}(x, y, r, 0) = c_{s0,pos} \quad (3.153)$$

where $C_{s,pos}$ is the concentration in the solid positive electrode and $c_{s0,pos}$ is the initial

concentration in the solid phase. Next the flux at the faces labelled 1, 2, 3, 5, and 6 as shown in Figure 3.93 were set to zero. The equation used for the Zero Flux subnode is shown below

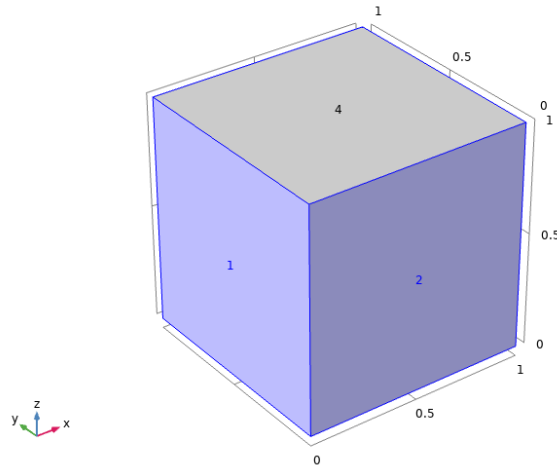


Figure 3.93 2D model, mbsp zero flux boundaries.

$$-n \cdot \Gamma = 0 \quad (3.154)$$

where n is the normal vector and Γ is the conservative flux. Finally within the interface a Flux/Source subnode was created. The equation used for the Flux/Source subnode is shown below

$$-n \cdot \Gamma = g - qu \quad (3.155)$$

where n is the normal vector, Γ is the conservative flux, g is the boundary flux/source, q is the boundary absorption/impedance term, and u is the dependent variable. This flux is for pore-wall flux across the interface on the boundary shown in Figure 3.92. Matching like

coefficients between equations (3.148) and (3.155), results in the relations shown below in Table 3.45. With the convention that the negative of the normal vector is pointing into the domain, a negative flux means that the vector would be pointing out of the domain and the flux would be moving to the upwards.

Table 3.45 2D Model, MBSP Flux/Source

Flux/Source	Value
g	$-\frac{r^2}{R_{s,pos}} \frac{j_{li,pos}}{a_{s,pos}F}$
q	0

3.3.14 Linear Extrusions

Because the model has three components to it; a two dimensional domain, a three dimensional domain, and an additional three dimensional name, COMSOL does not directly allow solved dependent variables to be cross coupled to other components. To accomplish this there are multiple options. The the most abstract way is what COMSOL calls General Extrusions. But in the case of this model a Linear Extrusion would suffice because in all three cases a boundary is being mapped to a boundary.

For the component that consists of eight partial differential equations; CBSN, CBSP, CBEN, CBES, CBEP, MBEN, MBES, and MBEP two linear extrusions are required. One linear extrusion is required to couple the variables to the material balance in the solid negative electrode (MBSN), and the second linear extrusion is required to couple the variables to the material balance in the solid positive electrode (MBSP).

For the linear extrusion to the MBSN, the source domain would be the region shown in Figures 3.62, 3.68, and 3.78. This region is again shown below in Figure 3.94. The destination domain would be Geometry 2 which is the geometry for the MBSN shown in

the model tree in Figure 3.52 and shown below in Figure 3.95.

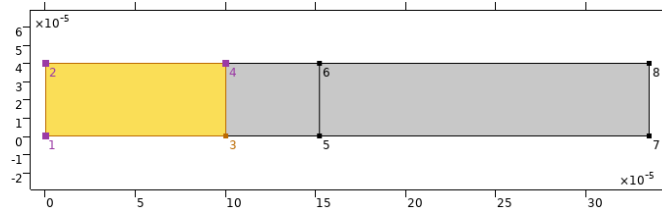


Figure 3.94 2D model, linear extrusion 1 source.

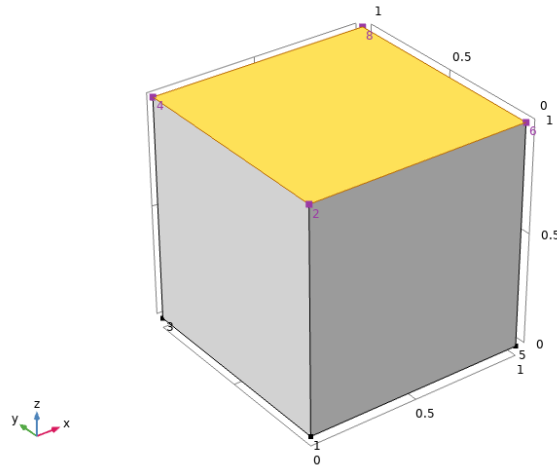


Figure 3.95 2D model, linear extrusion 1 destination.

Source vertex 1 would be point 2 in Figure 3.94, source vertex 2 would be point 4 in Figure 3.94, and source vertex 3 would be point 1 in Figure 3.94. Destination vertex 1 would be point 4 in Figure 3.95, destination vertex 2 would be point 8 in Figure 3.95, and destination vertex 3 would be point 2 in Figure 3.95.

For the linear extrusion to the MBSP, the source domain would be the region shown in Figures 3.65, 3.75, and 3.85. This region is again shown below in Figure 3.96. The destination domain would be Geometry 3 which is the geometry for the MBSP shown in the model tree in Figure 3.52 and shown below in Figure 3.97.

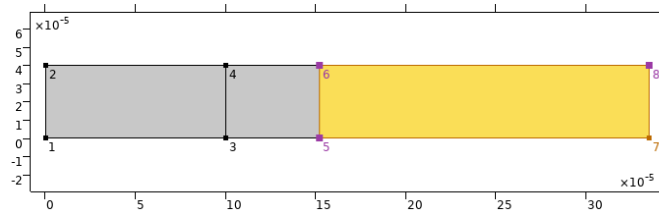


Figure 3.96 2D model, linear extrusion 2 source.

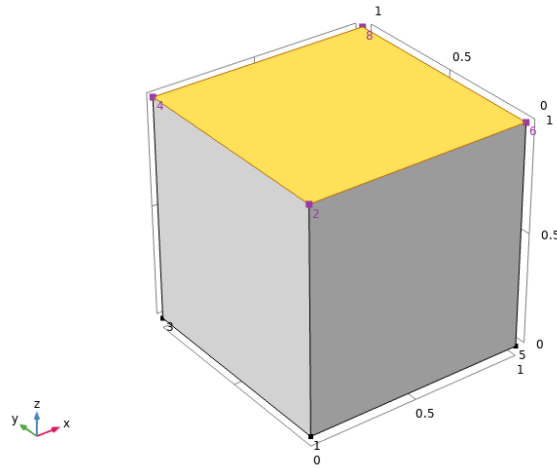


Figure 3.97 2D model, linear extrusion 2 destination.

Source vertex 1 would be point 2 in Figure 3.96, source vertex 2 would be point 4 in Figure 3.96, and source vertex 3 would be point 1 in Figure 3.96. Destination vertex 1 would be point 4 in Figure 3.97, destination vertex 2 would be point 8 in Figure 3.47, and destination vertex 3 would be point 2 in Figure 3.97.

For the component that consists of the partial differential equation for the material balance in the solid negative electrode (MBSN), one linear extrusion is required. One is only because it is only mapping to the component that has the CBSN, CBSP, CBEN, CBES, CBEP, MBEN, MBES, and MBEP equations.

For the linear extrusion to the main component, the source domain would be region shown below in Figure 3.98. The destination domain would be Geometry 1 which is the geometry for the main component shown in the model tree in Figure 3.52, and the region

shown in Figures 3.62, 3.68, and 3.78. This region is again shown below in Figure 3.99.

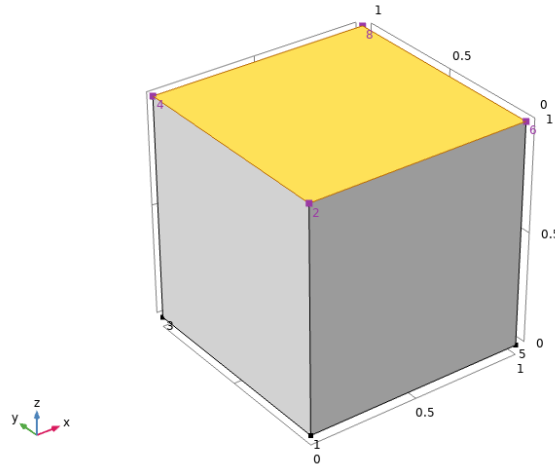


Figure 3.98 2D model, linear extrusion 3 source.

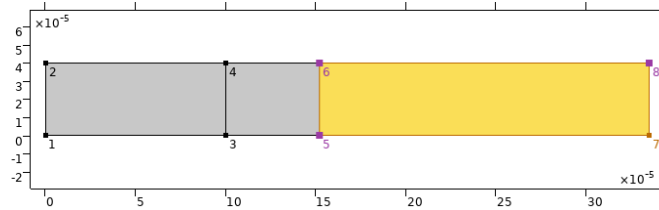


Figure 3.99 2D model, linear extrusion 3 destination.

Source vertex 1 would be point 4 in Figure 3.98, source vertex 2 would be point 8 in Figure 3.98, and source vertex 3 would be point 2 in Figure 3.98. Destination vertex 1 would be point 2 in Figure 3.99, destination vertex 2 would be point 4 in Figure 3.99, and destination vertex 3 would be point 1 in Figure 3.99.

For the component that consists of the partial differential equation for the material balance in the solid positive electrode (MBSP), one linear extrusion is required. One is only required because it is only mapping to the component that has the CBSN, CBSP, CBEN, CBES, CBEP, MBEN, MBES, and MBEP equations.

For the linear extrusion to the main component, the source domain would be region shown below in Figure 3.100. The destination domain would be Geometry 1 which is the

geometry for the main component shown in the model tree in Figure 3.52, and the region shown in Figures 3.65, 3.75, and 3.85. This region is again shown below in Figure 3.101.

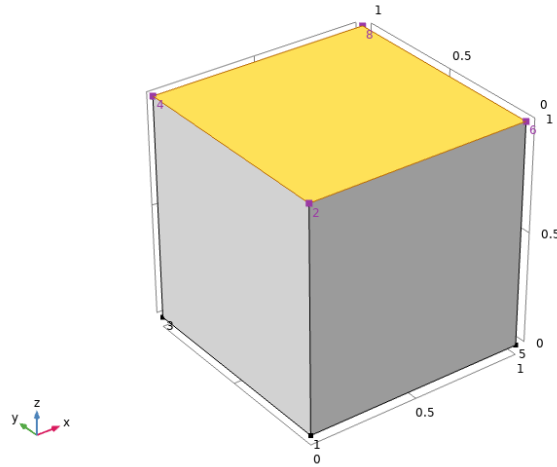


Figure 3.100 2D model, linear extrusion 4 source.

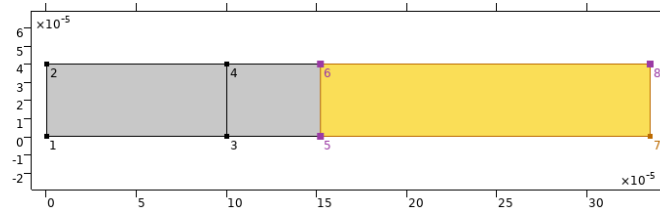


Figure 3.101 2D model, linear extrusion 4 destination.

Source vertex 1 would be point 4 in Figure 3.100, source vertex 2 would be point 8 in Figure 3.100, and source vertex 3 would be point 2 in Figure 3.100. Destination vertex 1 would be point 2 in Figure 3.101, destination vertex 2 would be point 4 in Figure 3.101, and destination vertex 3 would be point 1 in Figure 3.101.

3.4 Magnetic Field

The magnetic field was added to the two dimensional model in the following partial differential equations; CBEN, CBES, CBEP, CBSN, and CBSP. If the applied magnetic field were into the two dimensional battery or out of the two dimensional battery, not in the x

or y direction, then the resulting cross product with the current density in the x direction, would be an addition in the y direction. This cross product is shown in Figure 3.53. For the CBEN, Table 3.28 was modified accordingly as seen below in Table 3.46.

Table 3.46 2D Model, CBEN Magnetic Field Parameters

General Form	Value
f	$-j_{li,neg}$
e_a	0
d_a	0
Γ_x	$\kappa^{eff,neg} \frac{\partial}{\partial x} \varphi_{e,neg} + \kappa_{d,neg}^{eff,neg} \frac{\partial}{\partial x} \frac{\frac{\partial C_{e,neg}}{\partial x}}{C_{e,neg}}$
Γ_y	$\kappa^{eff,neg} \left(\frac{\kappa^{eff,neg}}{C_{e,neg} F} B_z + 1 \right) \frac{\partial}{\partial y} \varphi_{e,neg} + \kappa_{d,neg}^{eff,neg} \frac{\partial}{\partial y} \frac{\frac{\partial C_{e,neg}}{\partial y}}{C_{e,neg}}$

For the CBES, Table 3.30 was modified accordingly as seen below in Table 3.47.

Table 3.47 2D Model, CBES Magnetic Field Parameters

General Form	Value
f	0
e_a	0
d_a	0
Γ_x	$\kappa^{eff,sep} \frac{\partial}{\partial x} \varphi_{e,sep} + \kappa_{d,sep}^{eff,sep} \frac{\partial}{\partial x} \frac{\frac{\partial C_{e,sep}}{\partial x}}{C_{e,sep}}$
Γ_y	$\kappa^{eff,sep} \left(\frac{\kappa^{eff,sep}}{C_{e,sep} F} B_z + 1 \right) \frac{\partial}{\partial y} \varphi_{e,sep} + \kappa_{d,sep}^{eff,sep} \frac{\partial}{\partial y} \frac{\frac{\partial C_{e,sep}}{\partial y}}{C_{e,sep}}$

For the CBEP, Table 3.33 was modified accordingly as seen below in Table 3.48.

Table 3.48 2D Model, CBEP Magnetic Field Parameters

General Form	Value
f	$-j_{li,pos}$
e_a	0
d_a	0
Γ_x	$\kappa^{eff,pos} \frac{\partial}{\partial x} \varphi_{e,pos} + \kappa_{d,pos}^{eff,pos} \frac{\partial}{\partial x} \frac{\frac{\partial C_{e,pos}}{\partial x}}{C_{e,pos}}$
Γ_y	$\kappa^{eff,pos} \left(\frac{\kappa^{eff,pos}}{C_{e,pos} F} B_z + 1 \right) \frac{\partial}{\partial y} \varphi_{e,pos} + \kappa_{d,pos}^{eff,pos} \frac{\partial}{\partial y} \frac{\frac{\partial C_{e,pos}}{\partial y}}{C_{e,pos}}$

For the CBSN, Table 3.25 was modified accordingly as seen below in Table 3.49.

Table 3.49 2D Model, CBSN Magnetic Field Parameters

General Form	Value
f	$j_{li,neg}$
e_a	0
d_a	0
Γ_x	$\sigma_{eff,neg} \frac{\partial}{\partial x} \varphi_{s,neg}$
Γ_y	$\sigma_{eff,neg} \left(\frac{\sigma_{eff,neg}}{C_{e,neg} F} B_z + 1 \right) \frac{\partial}{\partial y} \varphi_{s,neg}$

For the CBSP, Table 3.26 was modified accordingly as seen below in Table 3.50.

Table 3.50 2D Model, CBSP Magnetic Field Parameters

General Form	Value
f	$\dot{j}l_{i,pos}$
e_a	0
d_a	0
Γ_x	$\sigma_{eff,pos} \frac{\partial}{\partial x} \varphi_{s,pos}$
Γ_y	$\sigma_{eff,pos} \left(\frac{\sigma_{eff,pos}}{C_{e,pos} F} B_z + 1 \right) \frac{\partial}{\partial y} \varphi_{s,pos}$

3.5 Experiment Setup

Shown below in Figure 3.102 is a diagram of the charging circuit.

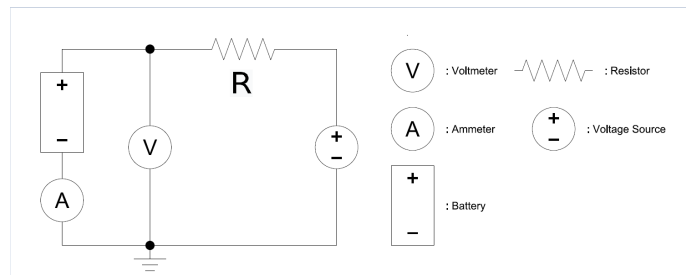


Figure 3.102 Experimental charging circuit.

Shown below in Figure 3.103 is a diagram of the discharging circuit.

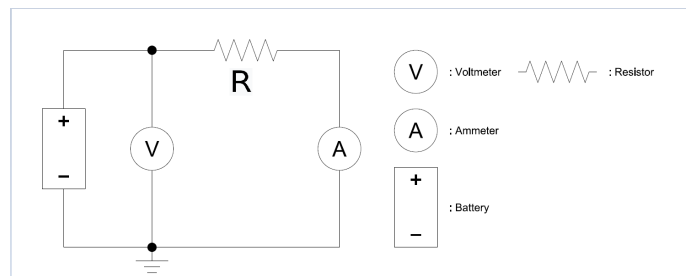


Figure 3.103 Experimental discharging circuit.

The magnetic field was created through a 6.5 Ohm coil rated for 1200A. The coil was enclosed, 9.5 mm tall, had an inner radius of 3 mm, and an outer radius of 9.5 mm.

Shown below in Figure 3.104 is a picture of the coil.



Figure 3.104 Experimental coil.

The power source for the coil was a HP 6200B Dc Power Supply (0-40V 0.75A/0-20V 1.5A). The voltmeter shown in Figure 3.102 and Figure 3.103 was a HP 34401 A Multimeter. The ammeter shown in Figure 3.102 and Figure 3.103 was a Agilent 34411A Multimeter. And the power source shown in Figure 3.102 was a HP 6200B DC Power Supply.

Three lithium ion batteries were tested. Two of the batteries were 3.0-4.0V 5mA batteries, and the other battery was a 3.0-4.0V 400mA battery. The small batteries (5mA) each had a height of 4.5 mm, a width of 3.5 mm, and a thickness of 0.05 mm. The large battery (400mA) had a height of 11 mm, a width of 5.5 mm, and a thickness of 0.3 mm. Shown below in Figure 3.105 is a picture of all the batteries under test.



Figure 3.105 Experimental batteries.

Each battery had a designation on them, but from now they will be referred to as LTB1, LTB8, and FE19. They were each placed on top of the coil. Shown below in Figure is the relative orientation of the batteries. The magnetic field strength was recorded using a Vernier Labpro interface with a Vernier Magnetif Field Sensor using Logger Lite 1.9.4. For the charge and discharge circuits for the smaller batteries, (LTB1 and LTB8), the charging and discharging resistor were both a 476.71Ω resistor. For the charge and discharge circuits for the larger battery, (FE19), the charging and discharging resistor were both a 15.92Ω resistor. Limitations of the Gauss meter sensor is that it can only measure (0-8)mT magnetic flux density \vec{B} . Shown below in Figures 3.106 and 3.107 are the batteries placed on the coil.

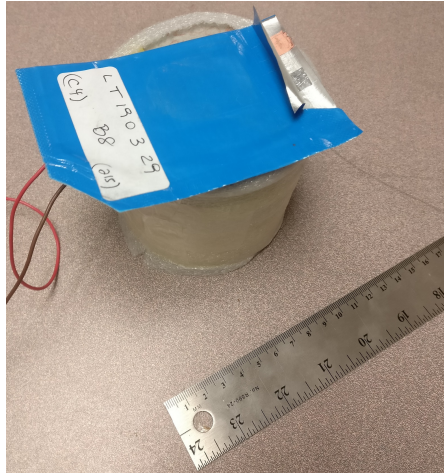


Figure 3.106 Experimental small battery on coil.



Figure 3.107 Experimental large battery on coil.

From the above pictures it can be seen that the magnetic flux density impressed on the small batteries is much more uniform than on the large battery due to their small areas. The large battery only sees a localized magnetic flux density around the center of the battery, but also due to its stacked nature the penetration is subjected to stronger attenuation.

CHAPTER 4

SIMULATION RESULTS AND EXPERIMENTAL RESULTS

4.1 1D Model

The 1D model was constructed to validate the 2D model. The 1D model was compared to plots from COMSOL's pre-built one-dimensional model. Shown below in Figure 4.1 is the plot generated from COMSOL's pre-built one-dimensional lithium battery simulation. Shown below in Figure 4.2 is the charge and discharge curve for the one-dimensional model created.

4.1.1 Discharge Charge Curves

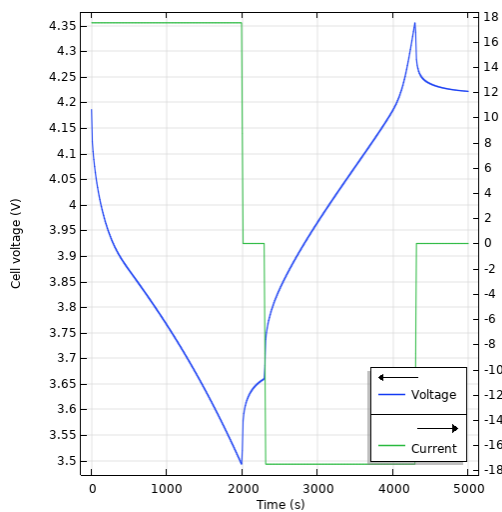


Figure 4.1 COMSOL 1d model, discharge charge curve.

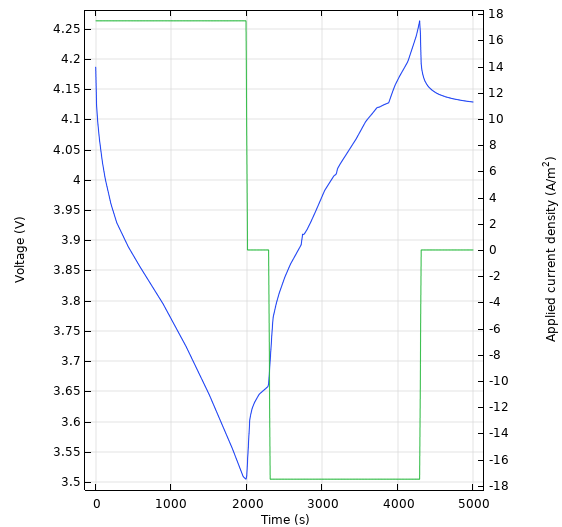


Figure 4.2 1D model, discharge charge curve.

From the above plots it can be seen that the constructed one-dimensional model agrees well with COMSOL's pre-built one-dimensional model. To achieve such agreement, the meshes of the domains were found to be very important. The wrong mesh would result data that did not match with such accuracy.

4.1.2 MBEN, MBES, MBEP

In this sections are the concentration along the one-dimensional domain. Shown in Figure 4.3 are the concentrations from 0 to 2000 seconds from COMSOL's model. Shown in Figure 4.4 are the concentrations from 0 to 2000 seconds from the constructed one-dimensional model.

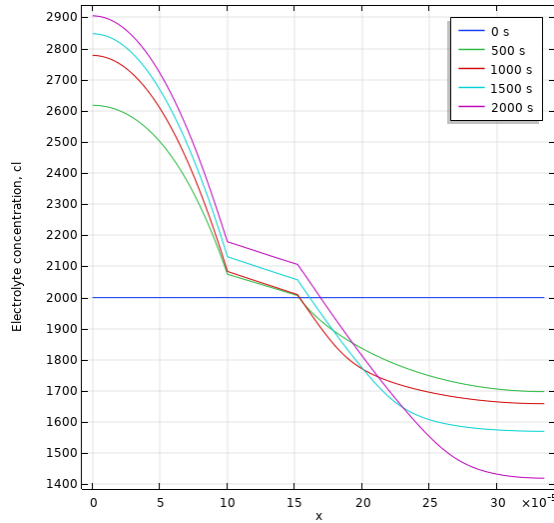


Figure 4.3 COMSOL 1d model, electrolyte concentration.

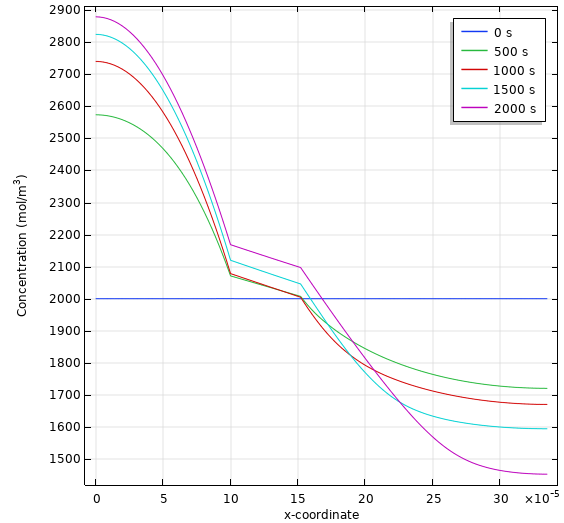


Figure 4.4 1D model, electrolyte concentration.

With the above graphs it shows that concentrations of the constructed model match well with COMSOL's model. Shown in Figure 4.5 are the concentrations from 2000 to 4000 seconds from the constructed one-dimensional model. Shown in Figure 4.6 are the concentrations from 4000 to 5000 seconds from the constructed one-dimensional model.

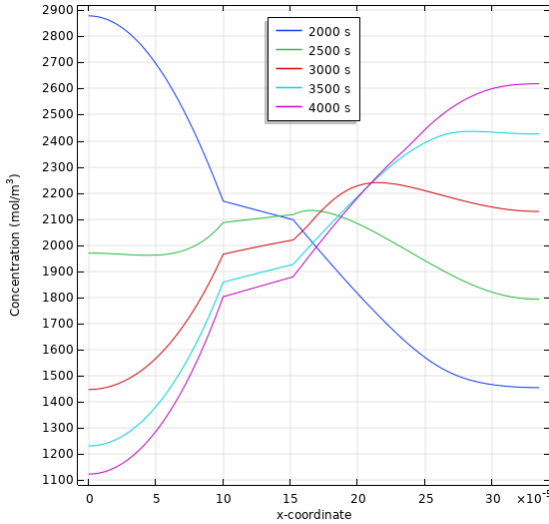


Figure 4.5 1D model, electrolyte concentration 2000s-4000s.

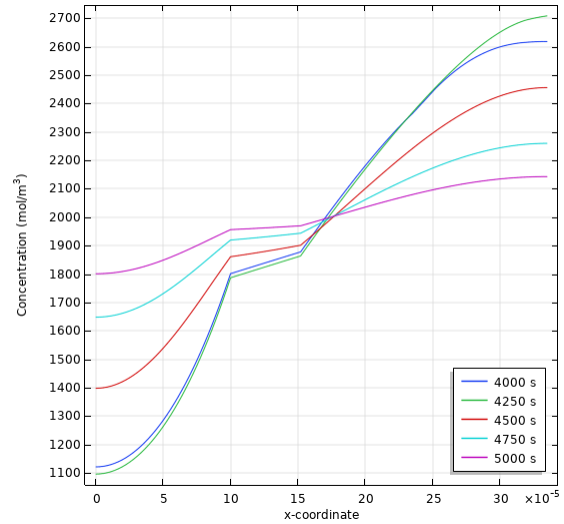


Figure 4.6 1D model, electrolyte concentration 4000s-5000s.

In the above figures it can be seen what happens to the concentrations during a charge cycle and during a rest period. In the charge cycle the concentrations in the negative electrode decrease while the concentrations in the positive electrode increase. In the rest period the concentrations appear to be reaching a equilibrium state through passive diffusion.

4.1.3 CBEN, CBES, CBEP

In this section are the potentials along the one-dimensional domain. Shown in Figure 4.7 are the potentials from 0 to 2000 seconds from COMSOL's model. Shown in Figure 4.8 are the potentials from 0 to 2000 seconds from the constructed one-dimensional model.

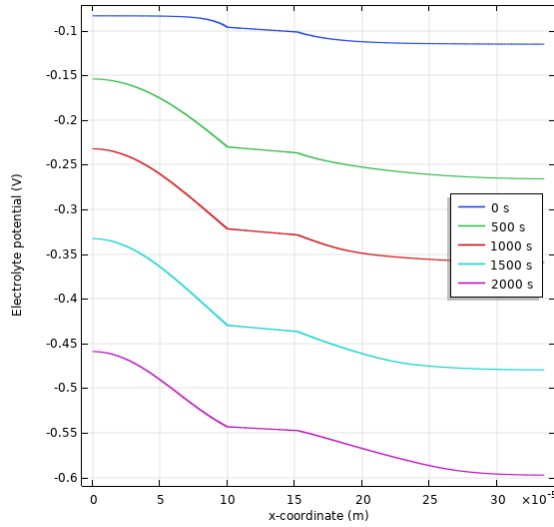


Figure 4.7 COMSOL 1d model, electrolyte potential 0-2000s.

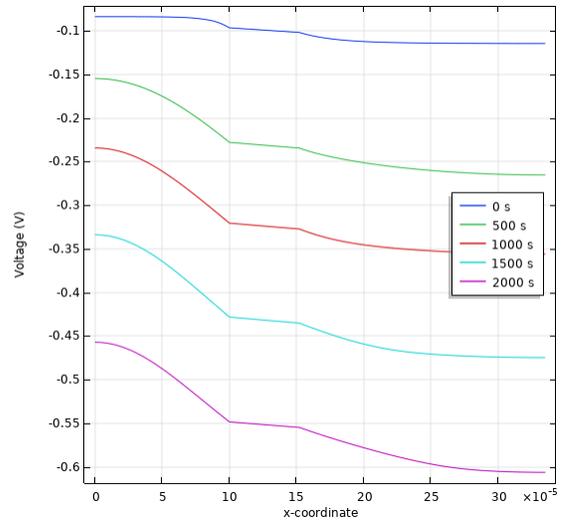


Figure 4.8 1D model, electrolyte potential 0-2000s.

With the above graphs it shows that potentials of the constructed model match well with COMSOL's model. Shown in Figure 4.9 are the potentials from 2000 to 4000 seconds from the constructed one-dimensional model. Shown in Figure 4.10 are the potentials from 4000 to 5000 seconds from the constructed one-dimensional model.

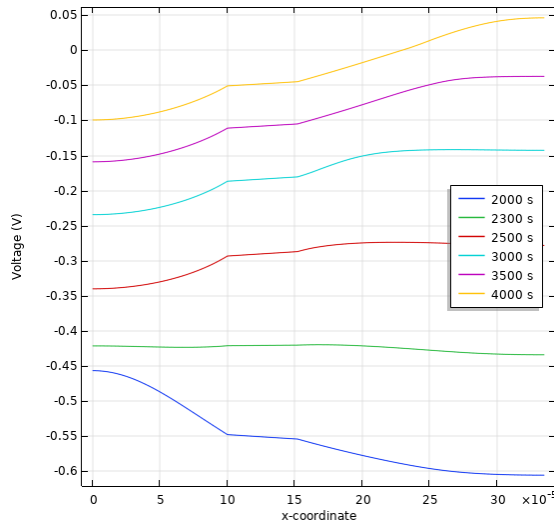


Figure 4.9 1D model, electrolyte potential 2000s-4000s.

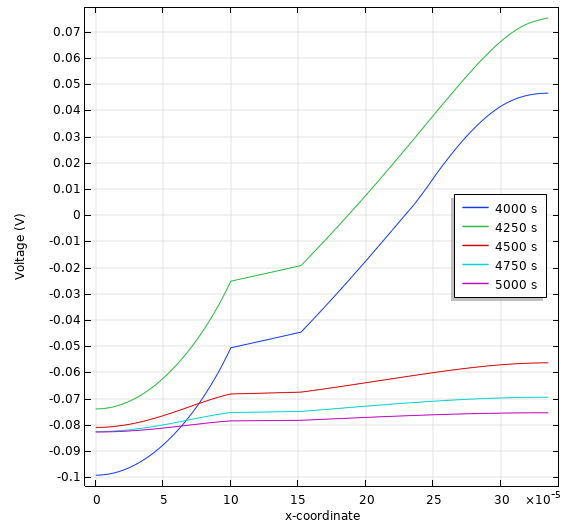


Figure 4.10 1D model, electrolyte potential 4000s-5000s.

In the above figures it can be seen what happens to the potentials during a charge cycle and during a rest period. In the charge cycle the potentials flip orientations along the y-axis. In the rest period the potentials appear to be reaching a steady potential.

4.1.4 MBSN, MBSP

In this section are the concentrations in the solid phase in the two-dimensional domain. Shown in Figure 4.11 are the concentrations from 0 to 1800 seconds from COMSOL's model. Shown in Figure 4.12 are the concentrations in the negative electrode from 0 to 1800 seconds from the constructed one-dimensional model. Shown in Figure 4.13 are the concentrations in the positive electrode from 0 to 1800 seconds from the constructed one-dimensional model.

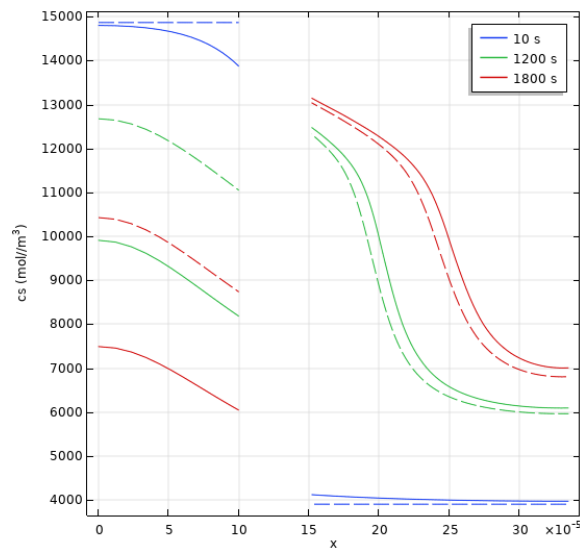


Figure 4.11 COMSOL 1d model, solid concentration.

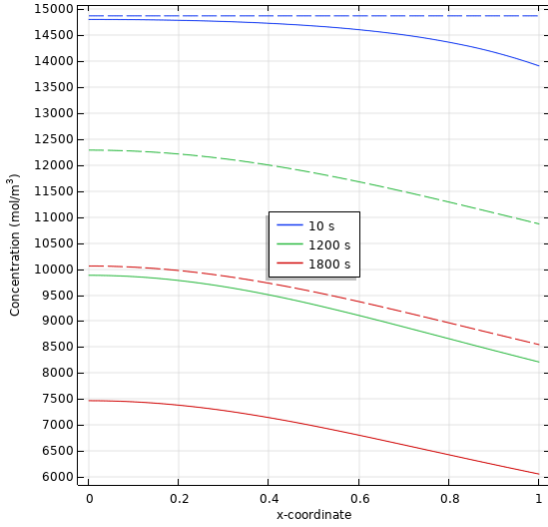


Figure 4.12 1D model, solid negative phase concentration.

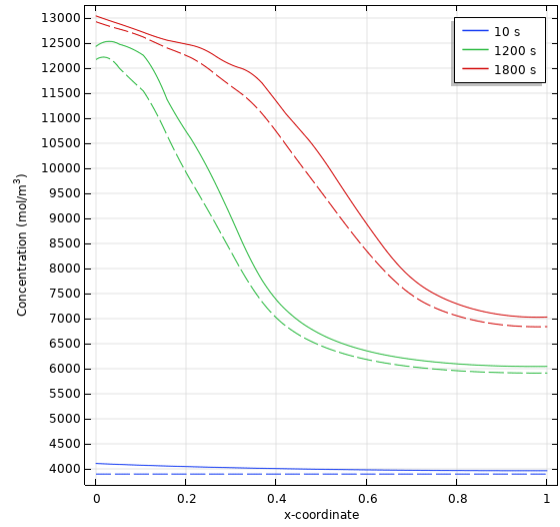


Figure 4.13 1D model, solid positive phase concentration.

With the above graphs it shows that concentrations of the constructed model match well with COMSOL's model. Shown in Figure 4.14 are the concentrations in the negative electrode at 10 seconds from the constructed one-dimensional model. Shown in Figure 4.15 are the concentrations in the positive electrode at 10 seconds from the constructed one-dimensional model.

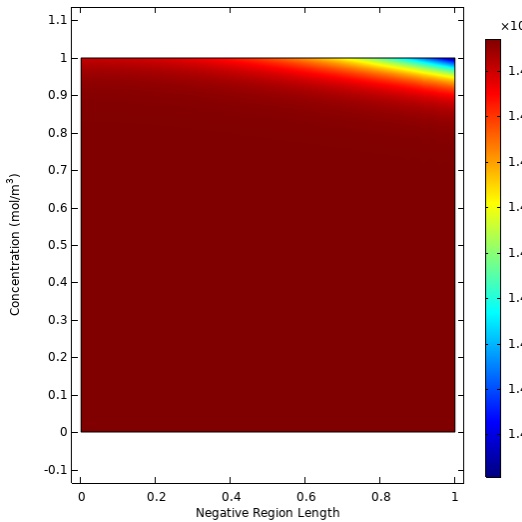


Figure 4.14 1D model, mbsn surface plot 10s.

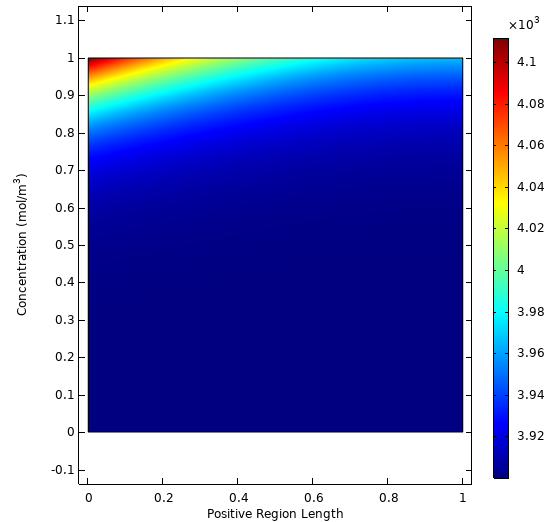


Figure 4.15 1D model, mbsp surface plot 10s.

These results show the symmetry of the lithium leaving one electrode and entering the other electrode. Shown in Figure 4.16 are the concentrations in the negative electrode at 1200 seconds from the constructed one-dimensional model. Shown in Figure 4.17 are the concentrations in the positive electrode at 1200 seconds from the constructed one-dimensional model.

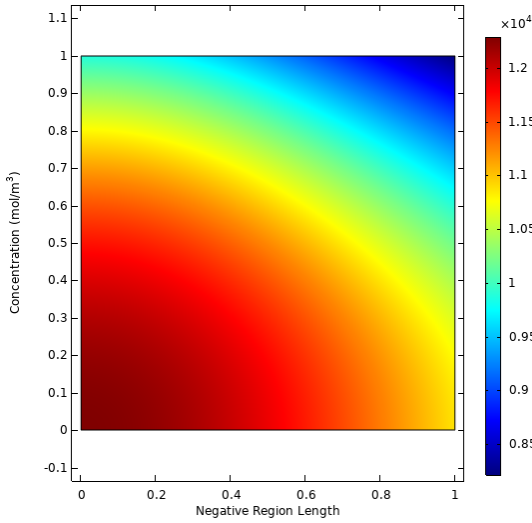


Figure 4.16 1D model, mbsn surface plot 1200s.

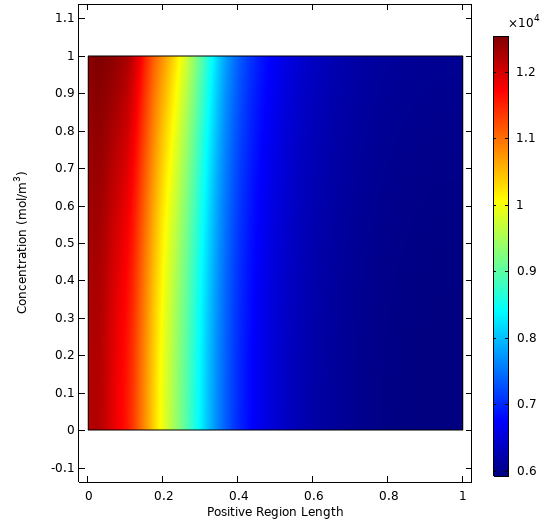


Figure 4.17 1D model, mbsp surface plot 1200s.

These results show the symmetry of the lithium leaving one electrode and entering the other electrode. Shown in Figure 4.18 are the concentrations in the negative electrode at 1200 seconds from the constructed one-dimensional model. Shown in Figure 4.19 are the concentrations in the positive electrode at 1200 seconds from the constructed one-dimensional model.

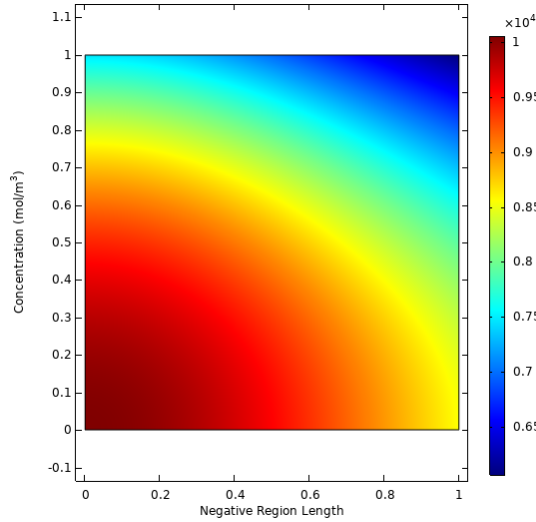


Figure 4.18 1D model, mbsn surface plot 1800s.

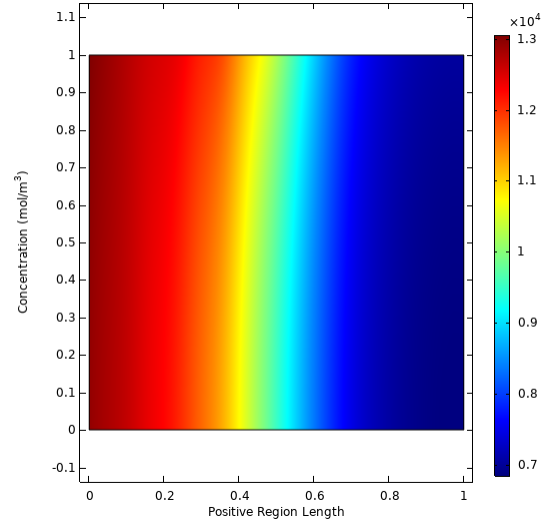


Figure 4.19 1D model, mbsp surface plot 1800s.

The above plots show that the most diffusion of the lithium occurs near the separator.

4.1.5 CBSN

In this section are the potentials in the negative solid phase. Shown in Figure 4.20 is the potential from 0 to 2000 seconds from the constructed one-dimensional model. Shown in Figure 4.21 is the potential from 2000 to 4000 seconds from the constructed one-dimensional model. Shown in Figure 4.22 is the potential from 4000 to 5000 seconds from the constructed one-dimensional model.

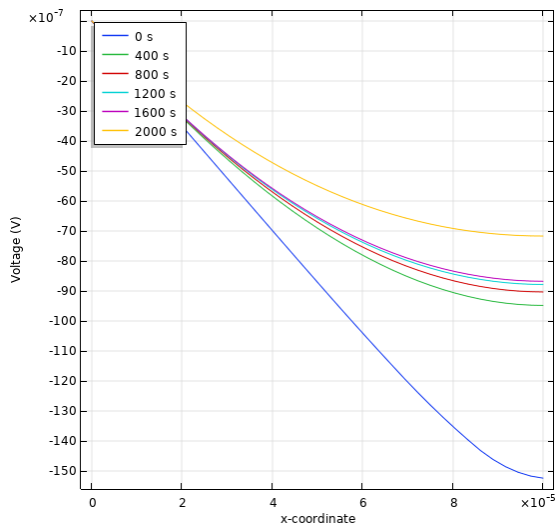


Figure 4.20 1D model, cbsn 0-2000s.

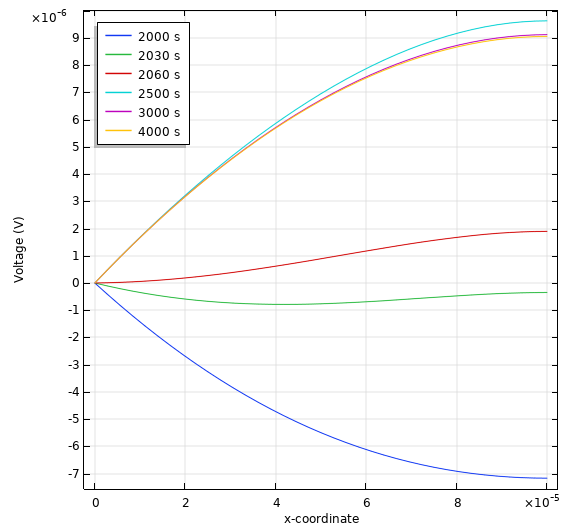


Figure 4.21 1D model, cbsn 2000s-4000s.

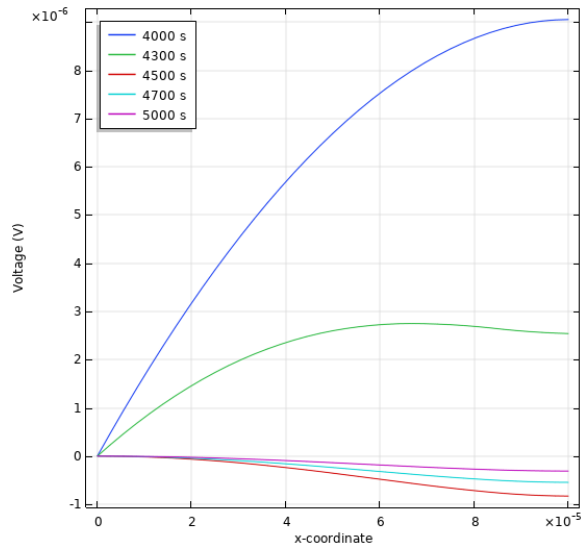


Figure 4.22 COMSOL 1d model, cbsn 4000s-5000s.

As the battery is being discharge the potential in the negative electrode decreases, as it is charged it becomes positive, and as it is left at rest it reaches an equilibrium state.

4.2 2D Model

The constructed two dimensional model had the parameter B_z adjusted to see the effect on the discharge and charge rate. The three values tested for increasing the magnetic field were 0mT, 0.5mT, and 1mT. The three values tested for decreasing the magnetic field and changing its direction were -1mT, 0.75mT, and 1mT.

4.2.1 PMF Discharge Charge Curves

This section focuses on increasing the positive magnetic field (PMF) on the constructed two-dimensional model. Shown below in Figure 4.23 are the charge and discharge curves for the three positive values.

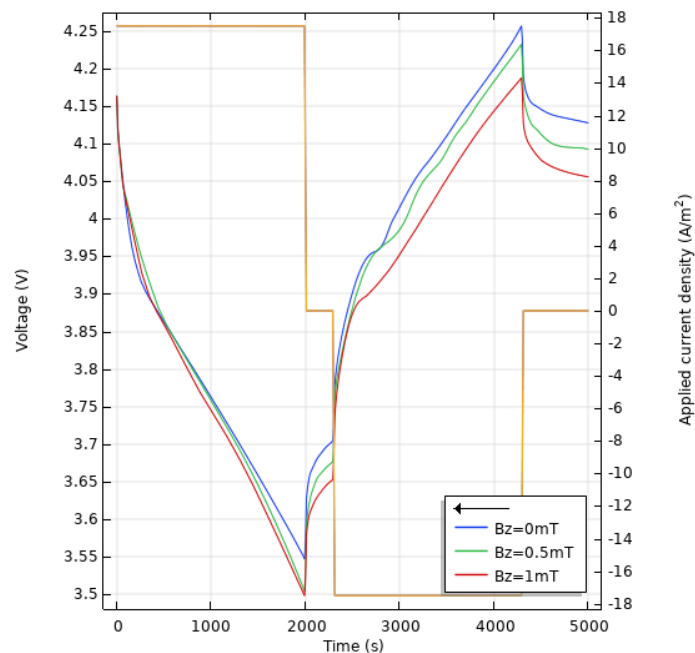


Figure 4.23 COMSOL 2d model, discharge charge curves.

The above graph showed that the magnetic field has an effect on the charging, discharging, and rest periods. As the magnetic field is increased, the battery discharges faster. For charging it appears that the battery takes longer to charge. All respective batteries come to rest at about the same rate.

4.2.2 PMF MBEN, MBES, MBEP

In this section are the concentrations of lithium in each region of the battery, the negative electrode, the separator, and the positive electrode. Shown in Figure 4.25 are the concentrations in the electrolyte from 0 to 2000 seconds for 0mT. Shown in Figure 4.26 are the concentrations in the electrolyte from 0 to 2000 seconds for 0.5mT.

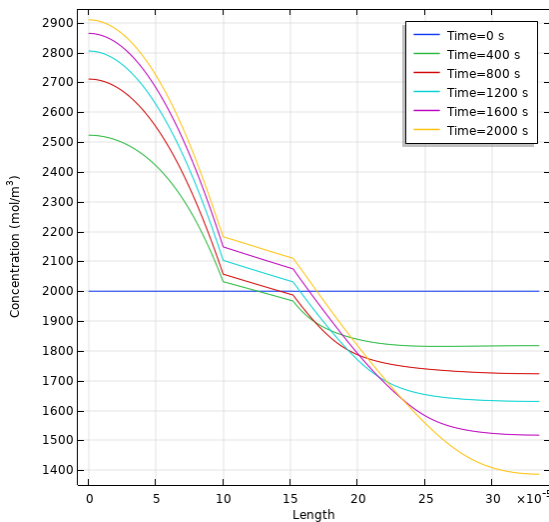


Figure 4.24 2D model, 0mT electrolyte concentration 0-2000s.

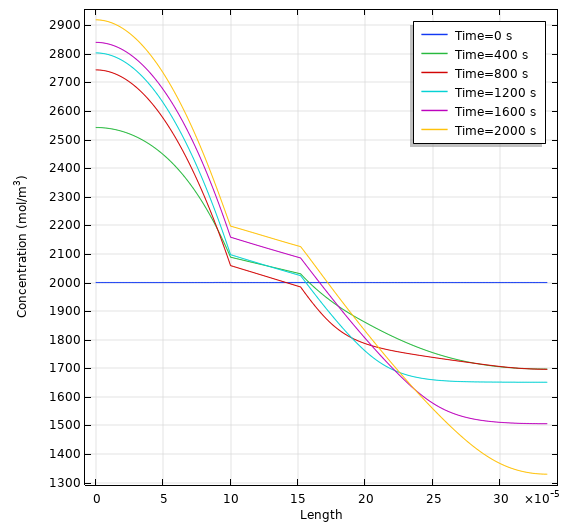


Figure 4.25 2D model, 0.5mT electrolyte concentration 0-2000s.

The above graphs show variation in the electrolyte concentrations during a discharge cycle. Shown in Figure 4.26 are the concentrations in the electrolyte from 2000 to 4000 seconds for 0mT. Shown in Figure 4.27 are the concentrations in the electrolyte from 2000 to 4000 seconds for 0.5mT.

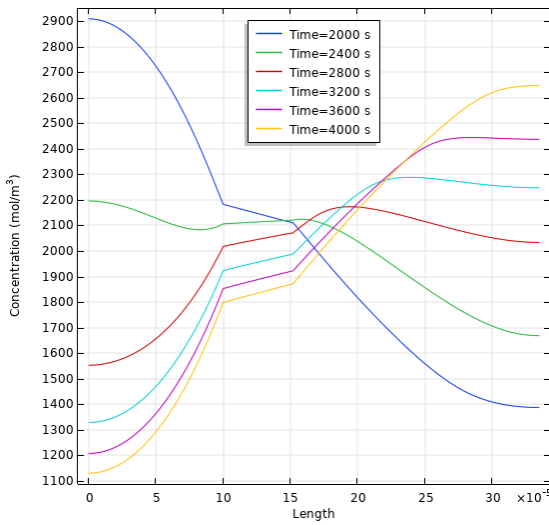


Figure 4.26 2D model, 0mT electrolyte concentration 2000s-4000s.

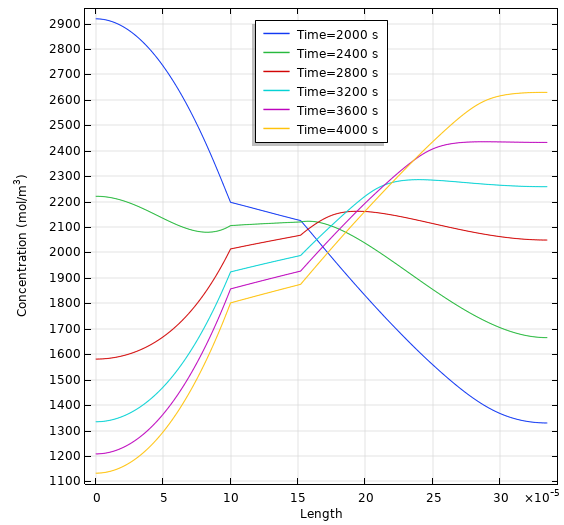


Figure 4.27 2D model, 0.5mT electrolyte concentration 2000s-4000s.

The above graphs show variation in the electrolyte concentrations during a charge cycle. Shown in Figure 4.28 are the concentrations in the electrolyte from 4000 to 5000 seconds for 0mT. Shown in Figure 4.29 are the concentrations in the electrolyte from 4000 to 5000 seconds for 0.5mT.

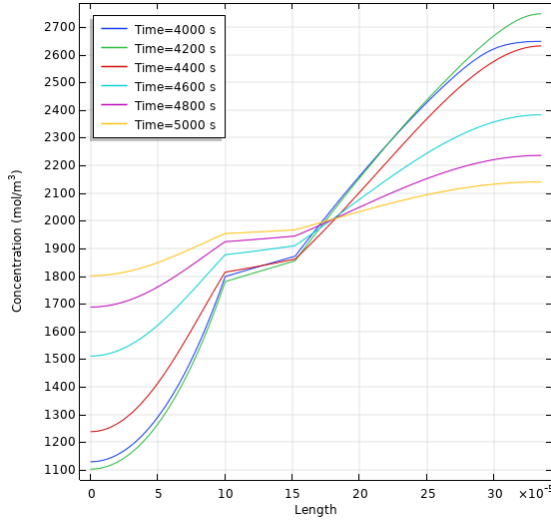


Figure 4.28 2D model, 0mT electrolyte concentration 4000s-5000s.

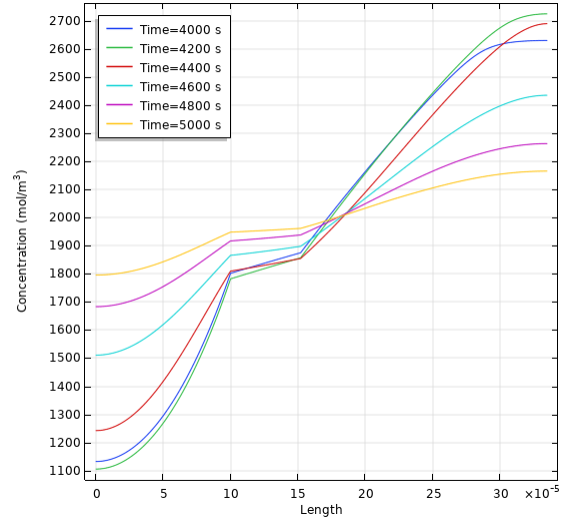


Figure 4.29 2D model, 0.5mT electrolyte concentration 4000s-5000s.

The above graphs show variation in the electrolyte concentrations during a rest period.

4.2.3 PMF CBEN, CBES, and CBEP

In this section are the potentials of the electrolyte in each region of the battery, the negative electrode, the separator, and the positive electrode. Shown in Figure 4.30 are the potentials in the electrolyte from 0 to 2000 seconds for 0mT. Shown in Figure 4.31 are the potentials in the electrolyte from 0 to 2000 seconds for 0.5mT.

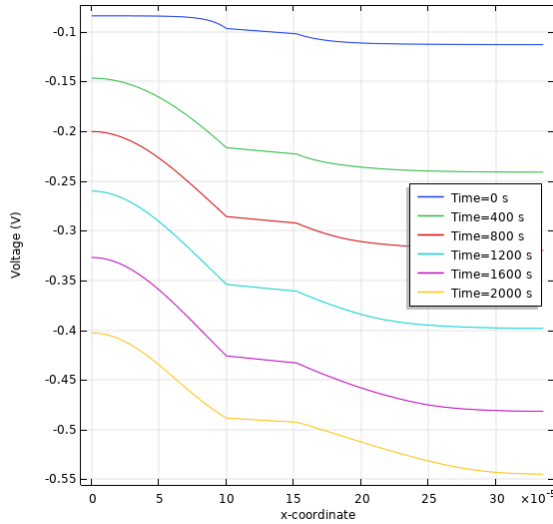


Figure 4.30 2D model, 0mT electrolyte potential 0-2000s.

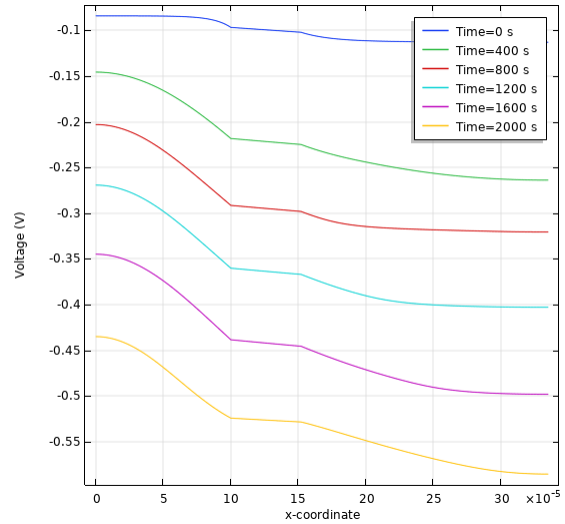


Figure 4.31 2D model, 0.5mT electrolyte potential 0-2000s.

The above graphs show variation in the electrolyte potentials during a discharge cycle. Shown in Figure 4.32 are the potentials in the electrolyte from 2000 to 4000 seconds for 0mT. Shown in Figure 4.33 are the potentials in the electrolyte from 2000 to 4000 seconds for 0.5mT.

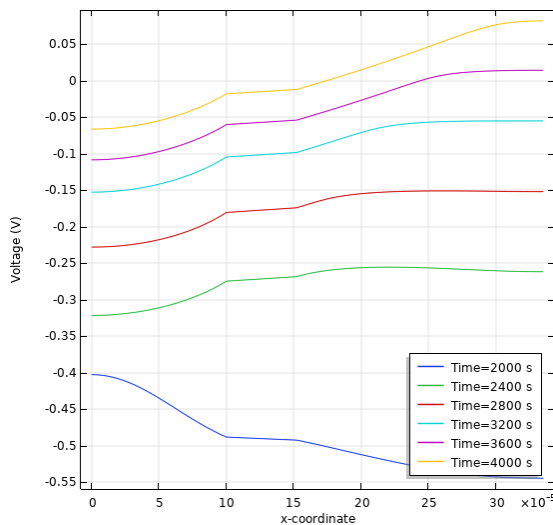


Figure 4.32 2D model, 0mT electrolyte potential 2000s-4000s.

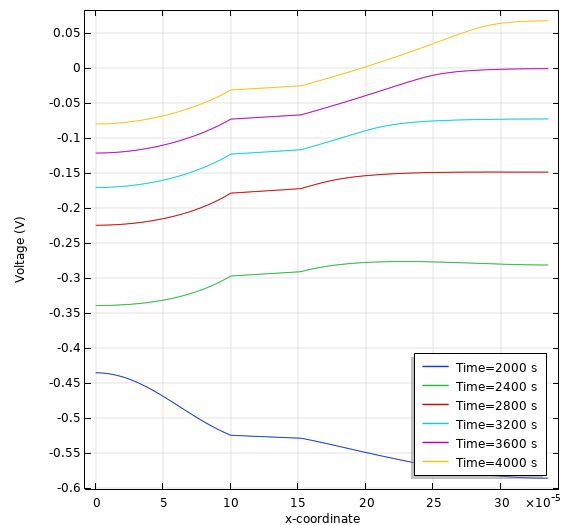


Figure 4.33 2D model, 0.5mT electrolyte potential 2000s-4000s.

The above graphs show variation in the electrolyte potentials during a charge cycle.

Shown in Figure 4.34 are the potentials in the electrolyte from 4000 to 5000 seconds for 0mT. Shown in Figure 4.35 are the potentials in the electrolyte from 4000 to 5000 seconds for 0.5mT.

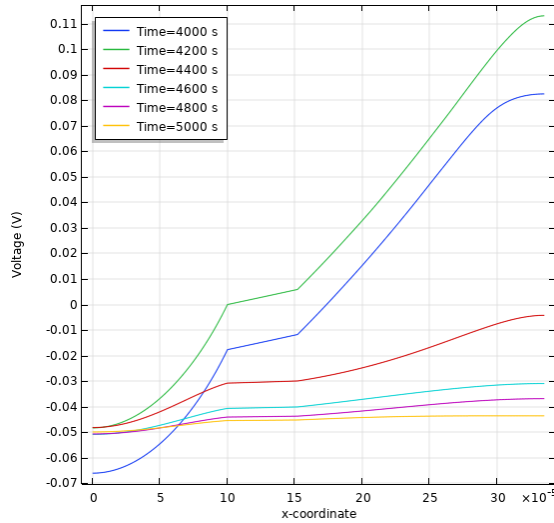


Figure 4.34 2D model, 0mT electrolyte potential 4000s-5000s.

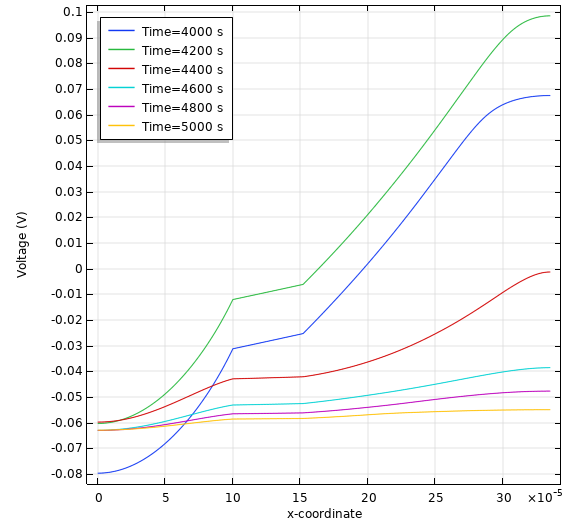


Figure 4.35 2D model, 0.5mT electrolyte potential 4000s-5000s.

The above graphs show variation in the electrolyte potentials during a rest period.

4.2.4 PMF MBSN and MBSP

In this section are the concentrations in the solid electrode for both the positive and negative electrodes. Shown in Figure 4.36 are the concentrations in the negative electrode at 10 seconds for 0mT. Shown in Figure 4.37 are the concentrations in the negative electrode at 10 seconds for 0.5mT.

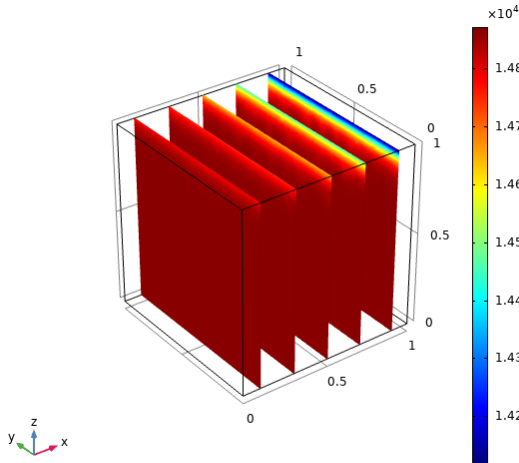


Figure 4.36 2D model, 0mT mbsn 10s.

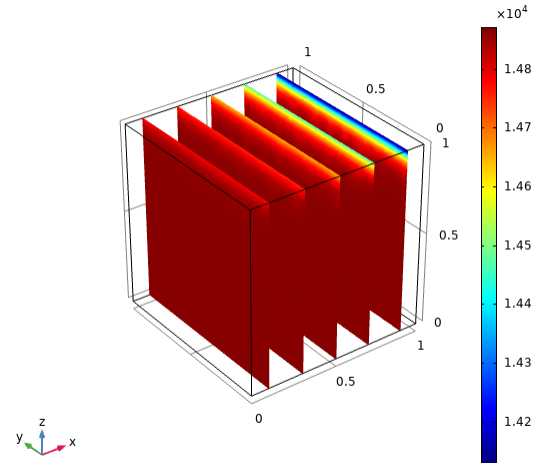


Figure 4.37 2D model, 0.5mT mbsn 10s.

The above graphs show variation in the concentration in the negative electrode during a discharge cycle. Shown in Figure 4.38 are the concentrations at 500s in the negative electrode for 0mT. Shown in Figure 4.39 are the concentrations at 500s in the negative electrode for 0.5mT.

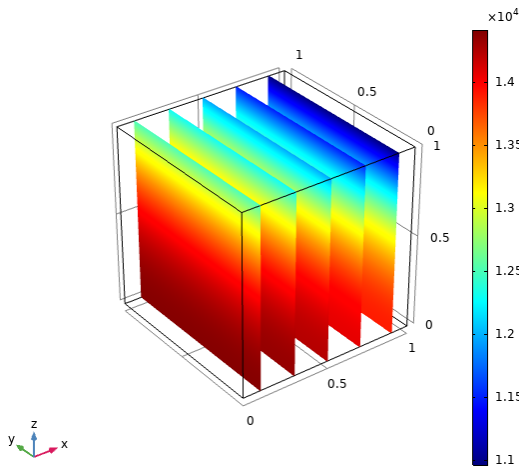


Figure 4.38 2D model, 0mT mbsn 500s.

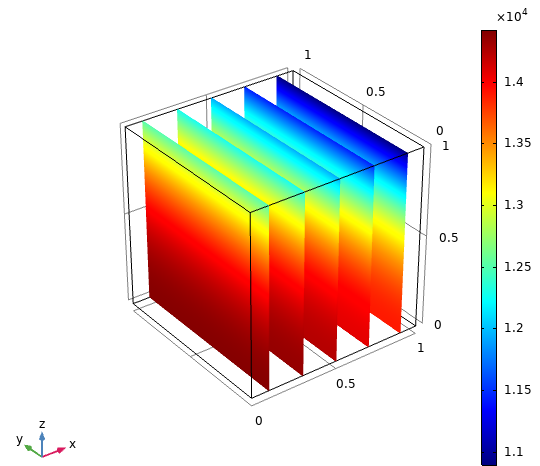


Figure 4.39 2D model, 0.5mT mbsn 500s.

The above graphs show variation in the concentration in the negative electrode during a discharge cycle. Shown in Figure 4.40 are the concentrations at 10s in the positive

electrode for 0mT. Shown in Figure 4.41 are the concentrations in the positive electrode at 10s in the negative electrode for 0.5mT.

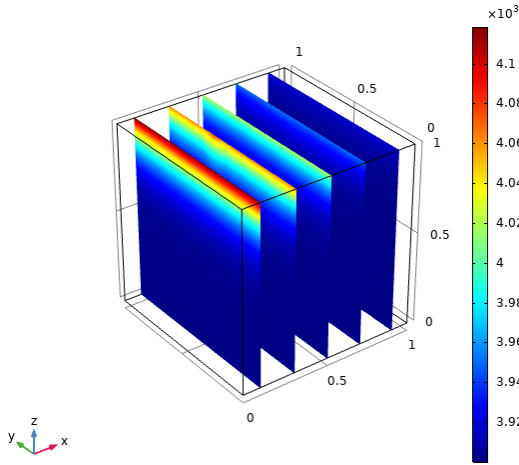


Figure 4.40 2D model, 0mT mbsp 10s.

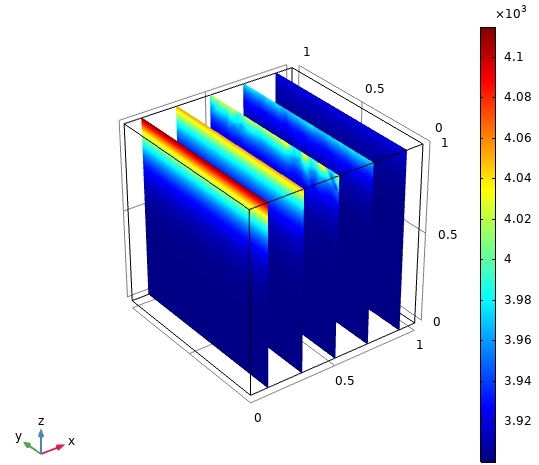


Figure 4.41 2D model, 0.5mT mbsp 10s.

The above graphs show variation in the concentration in the negative electrode during a discharge cycle. Shown in Figure 4.42 are the concentrations at 500s in the positive electrode for 0mT. Shown in Figure 4.43 are the concentrations in the positive electrode at 500s in the negative electrode for 0.5mT.

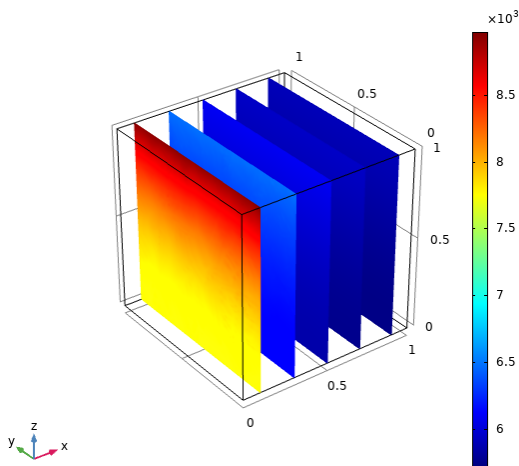


Figure 4.42 2D model, 0mT mbsp 500s.

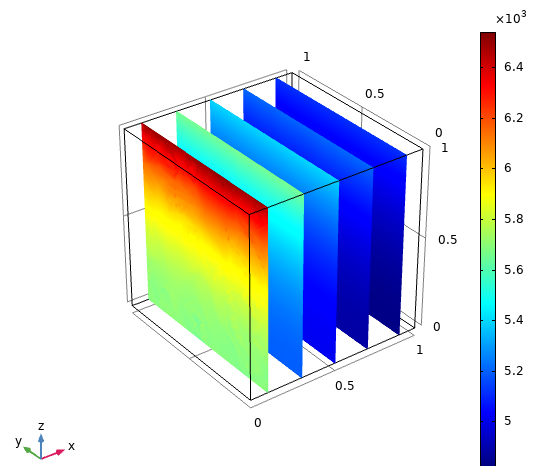


Figure 4.43 2D model, 0.5mT mbsp 500s.

A noticeable variation in the solid concentration at 500s is noticed in the solid positive electrode.

4.2.5 PMF CBSN

In this section is the potential in the solid negative electrode during a discharge, charge, and rest period. Shown in Figure 4.44 is the potential from 0 to 2000s in the negative electrode for 0mT. Shown in Figure 4.45 is the potential from 0 to 2000s in the negative electrode for 0.5mT.

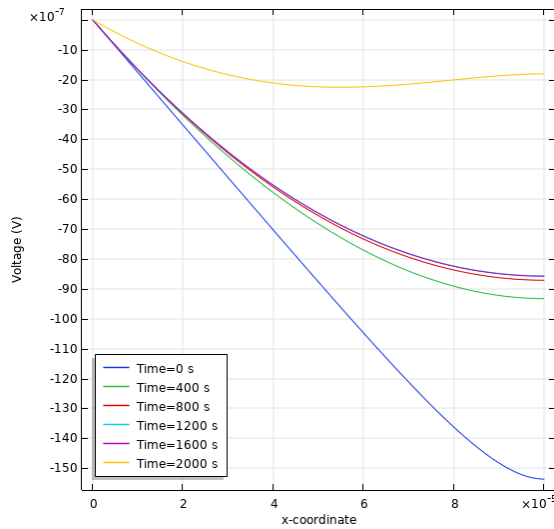


Figure 4.44 2D model, 0mT cbsn 0-2000s.

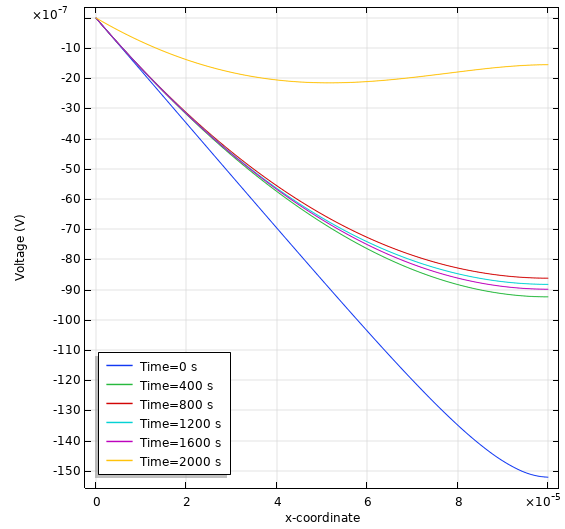


Figure 4.45 2D model, 0.5mT cbsn 0-2000s.

For the 0.5mT curve the potentials seem to be changing faster. Shown in Figure 4.46 is the potential from 2000 to 4000 seconds in the negative electrode for 0mT. Shown in Figure 4.47 is the potential from 2000 to 4000 seconds in the negative electrode for 0.5mT.

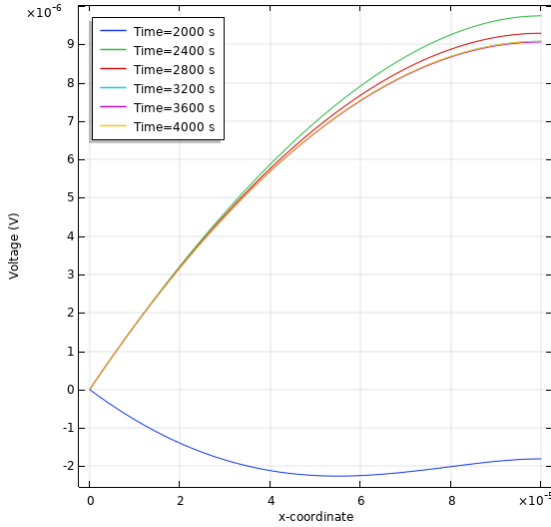


Figure 4.46 2D model, 0mT cbsn 2000s-4000s.

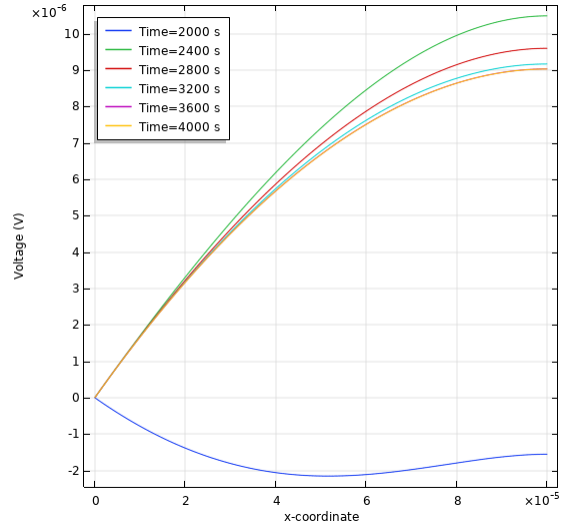


Figure 4.47 2D model, 0.5mT cbsn 2000s-4000s.

There appears to be more variation in the potentials in the 0.5mT curve than the 0mT curve. Shown in Figure 4.48 is the potential from 4000 to 5000 seconds in the negative electrode for 0mT. Shown in Figure 4.49 is the potential from 4000 to 5000 seconds in the negative electrode for 0.5mT.

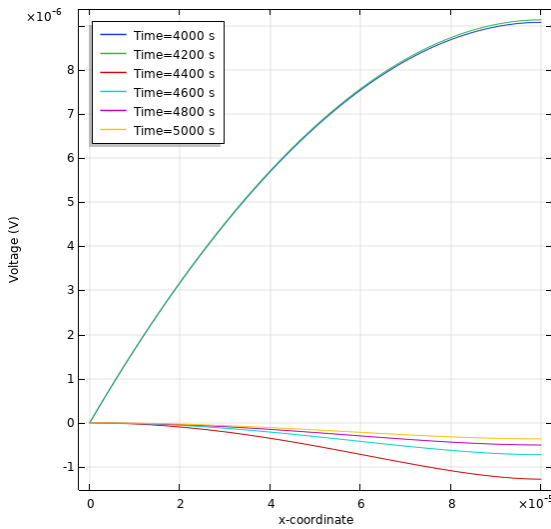


Figure 4.48 2D model, 0mT cbsn 4000s-5000s.

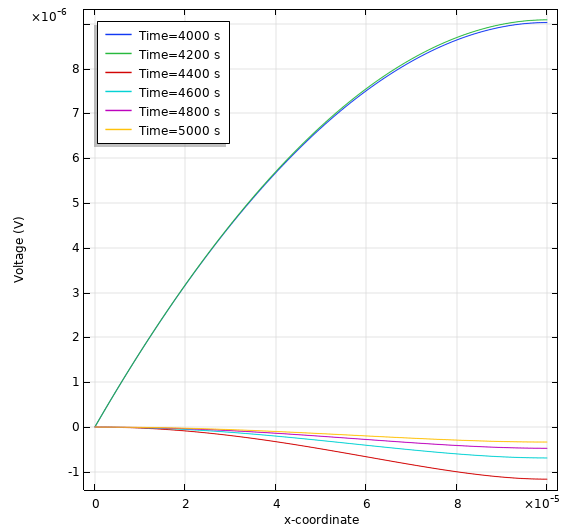


Figure 4.49 2D model, 0.5mT cbsn 4000s-5000s.

Not a significant difference is seen during the rest period for both field magnitudes.

4.2.6 NMF Discharge Charge Curves

This section focuses on changing the direction of the magnetic field to see the effect of a negative magnetic field (NMF) on the constructed two-dimensional model.

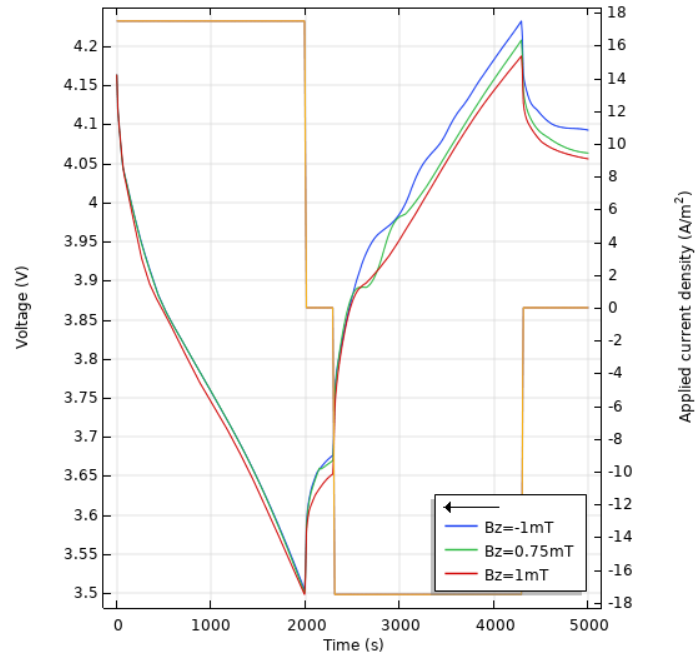


Figure 4.50 2D model, nmf discharge charge curves.

The negative magnetic field appears to charge faster than the positive magnetic field and the absence of the magnetic field.

4.2.7 NMF MBEN, MBES, MBEP

In this section are the concentrations of lithium in each region of the battery, the negative electrode, the separator, and the positive electrode. Shown in Figure 4.51 are the concentrations in the electrolyte from 0 to 2000 seconds for 0.75mT. Shown in Figure 4.52 are the concentrations in the electrolyte from 0 to 2000 seconds for -1mT.

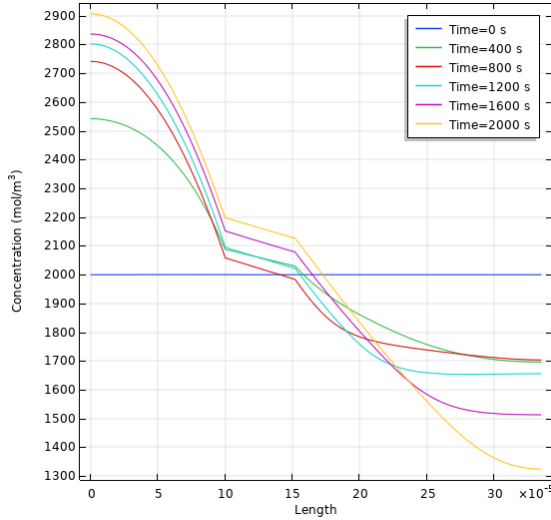


Figure 4.51 2D model, 0.75mT electrolyte concentration 0-2000s.

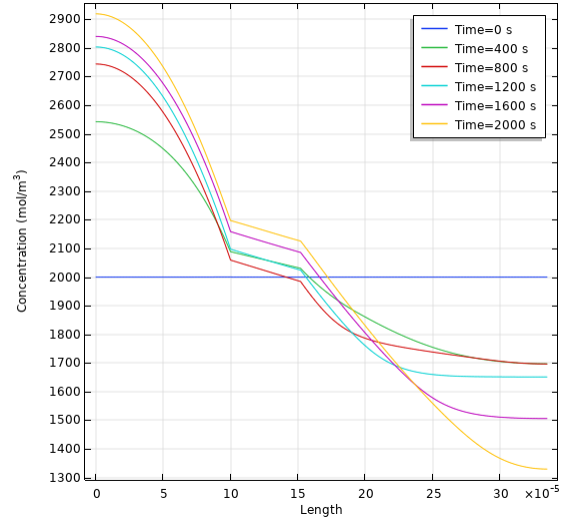


Figure 4.52 2D model, -1mT electrolyte concentration 0-2000s.

There is much variation seen for the electrolyte concentrations from 0 to 2000 seconds from the plots. Shown in Figure 4.53 are the concentrations in the electrolyte from 2000 to 4000 seconds for 0.75mT. Shown in Figure 4.54 are the concentrations in the electrolyte from 2000 to 4000 seconds for -1mT.

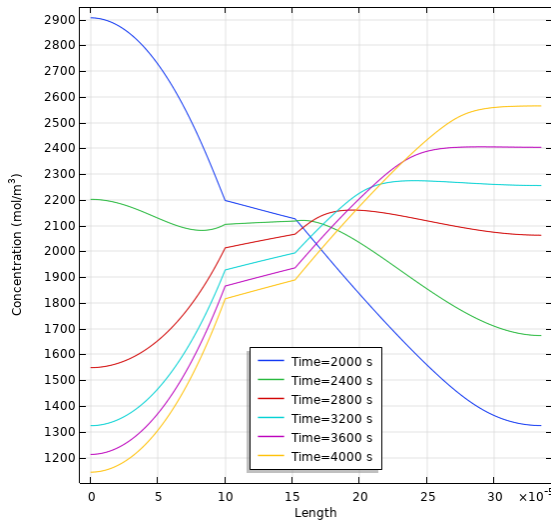


Figure 4.53 2D model, 0.75mT electrolyte concentration 2000s-4000s.

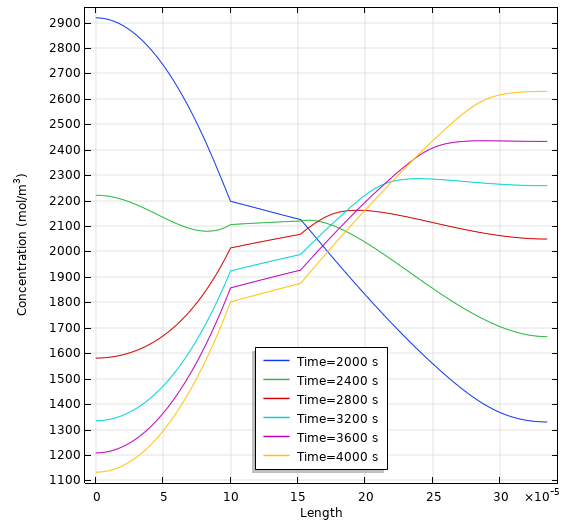


Figure 4.54 2D model, -1mT electrolyte concentration 2000s-4000s.

In the above graphs there is only a slight variation at 2800 seconds seen. Shown in Figure 4.55 are the concentrations in the electrolyte from 4000 to 5000 seconds for 0.75mT. Shown in Figure 4.56 are the concentrations in the electrolyte from 4000 to 5000 seconds for -1mT.

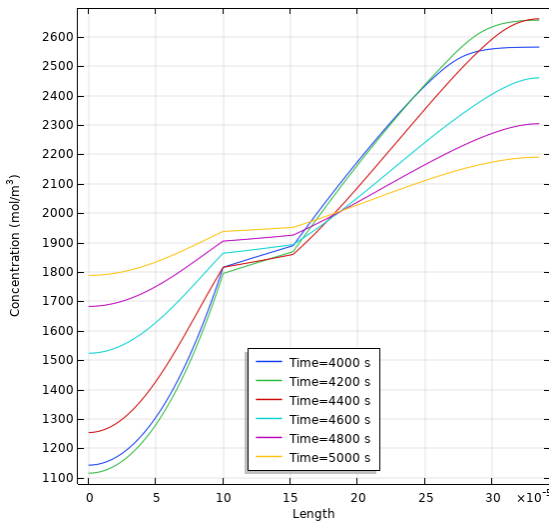


Figure 4.55 2D model, 0.75mT electrolyte concentration 4000s-5000s.

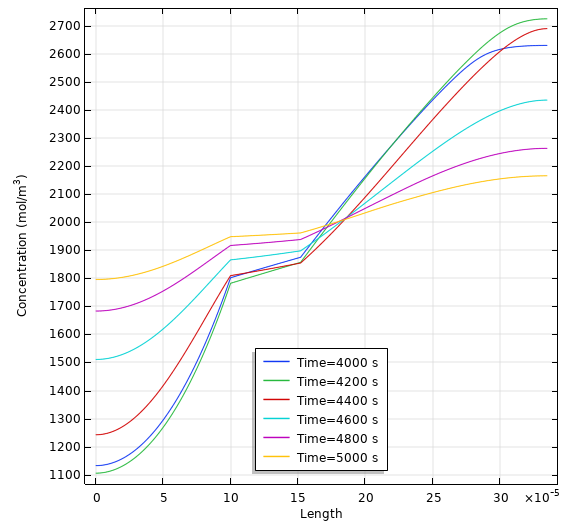


Figure 4.56 2D model, -1mT electrolyte concentration 4000s-5000s.

In the above graphs there is a slightly noticeable variation in the potentials at the various times.

4.2.8 NMF CBEN, CBES, and CBEP

In this section are the potentials of the electrolyte in each region of the battery; the negative electrode, the separator, and the positive electrode. Shown in Figure 4.57 are the potentials in the electrolyte from 0 to 2000s for 0.75mT. Shown in Figure 4.58 are the potentials in the electrolyte from 0 to 2000 seconds for -1mT.

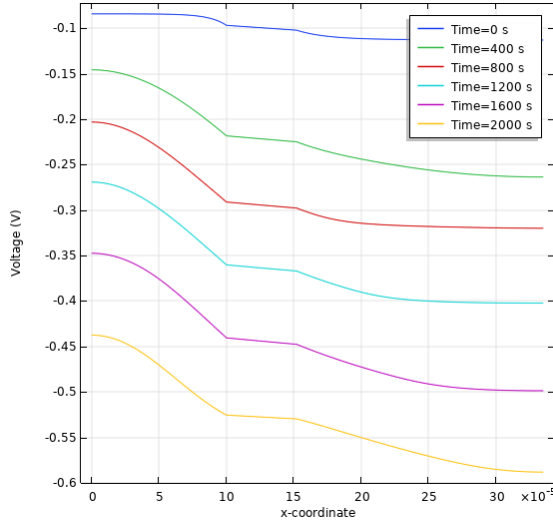


Figure 4.57 2D model, 0.75mT electrolyte potential 0-2000s.

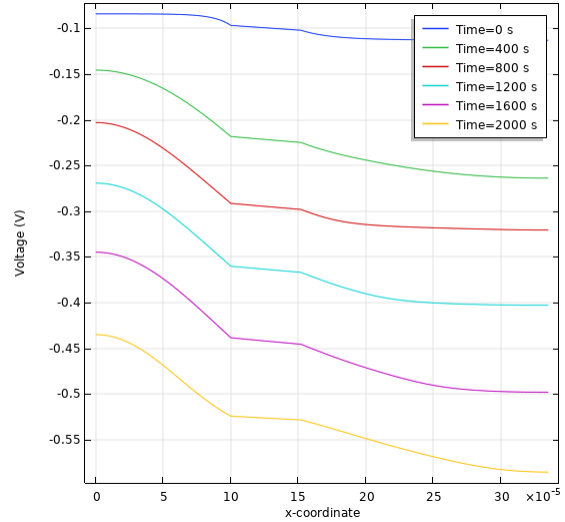


Figure 4.58 2D model, -1mT electrolyte potential 0-2000s.

In the above plots there is not much of a variation in the potentials. Shown in Figure 4.59 are the potentials in the electrolyte from 2000 to 4000s for 0.75mT. Shown in Figure 4.60 are the potentials in the electrolyte from 2000 to 4000 seconds for -1mT.

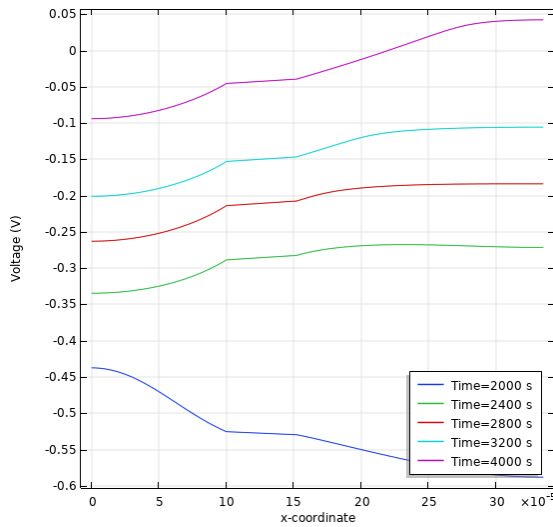


Figure 4.59 2D model, 0.75mT electrolyte potential 2000s-4000s.

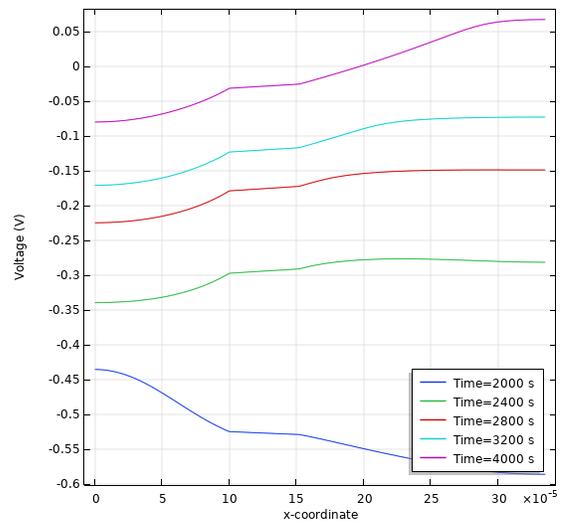


Figure 4.60 2D model, -1mT electrolyte potential 2000s-4000s.

In the above plots there is a slight variation at 2400 seconds. Shown in Figure 4.61 are the potentials in the electrolyte from 2000 to 4000s for 0.75mT. Shown in Figure 4.62

are the potentials in the electrolyte from 2000 to 4000 seconds for -1mT.

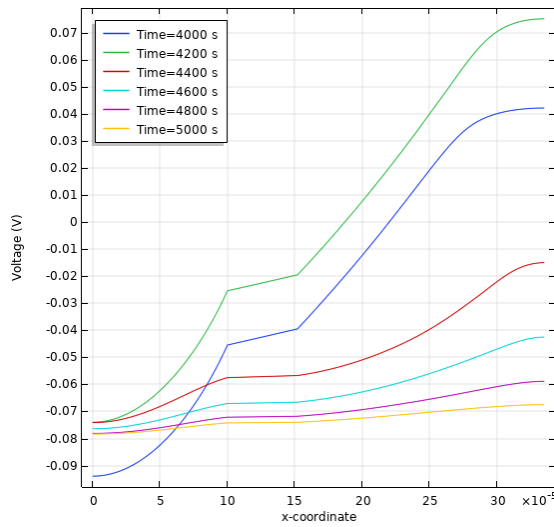


Figure 4.61 2D model, 0.75mT electrolyte potential 4000s-5000s.

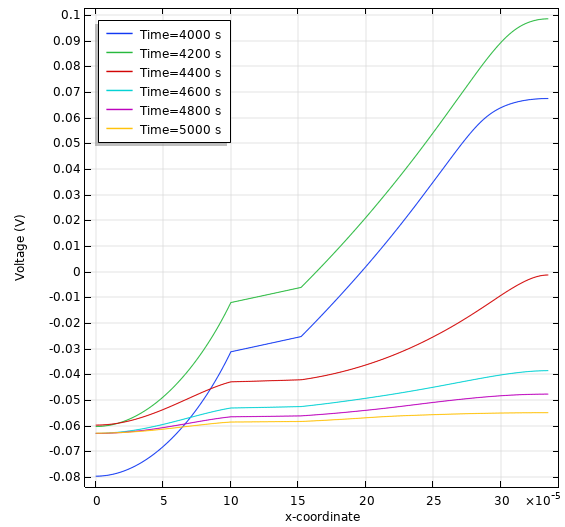


Figure 4.62 2D model, -1mT electrolyte potential 4000s-5000s.

In Figure 4.62 at 4200 seconds the potential is higher than in Figure 4.61.

4.2.9 NMF MBSN and MBSP

In this section are the concentrations in the solid electrode for both the positive and negative electrodes. Shown in Figure 4.63 are the concentrations in the negative electrode at 10 seconds for 0.75mT. Shown in Figure 4.64 are the concentrations in the negative electrode at 10 seconds for -1mT.

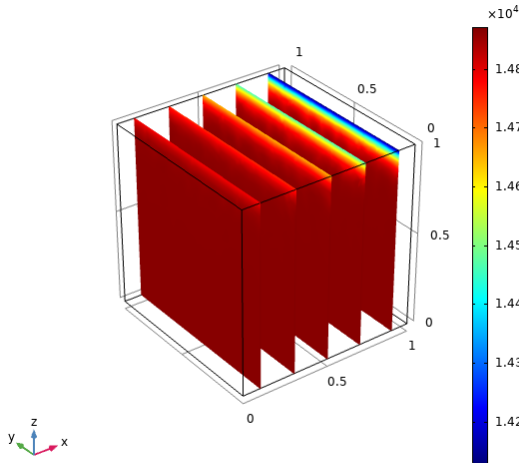


Figure 4.63 2D model, 0.75mT mbsn 10s.

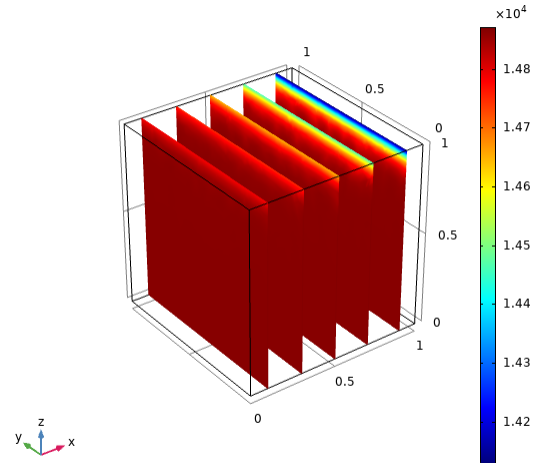


Figure 4.64 2D model, -1mT mbsn 10s.

In the above plots there not a noticeable difference in concentrations. Shown in Figure 4.65 are the concentrations in the solid negative electrode at 500 seconds for 0.75mT. Shown in Figure 4.66 are the concentrations in the solid negative electrode at 500 seconds for -1mT.

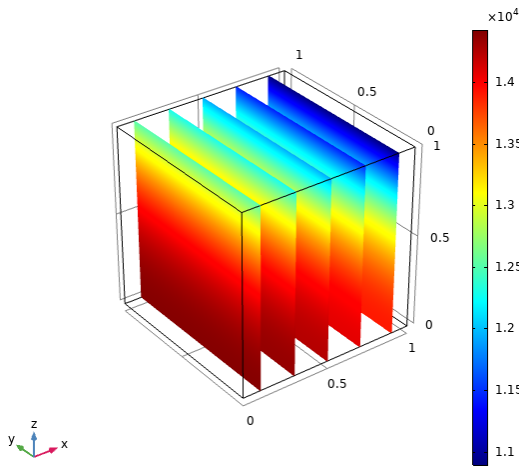


Figure 4.65 2D model, 0.75mT mbsn 500s.

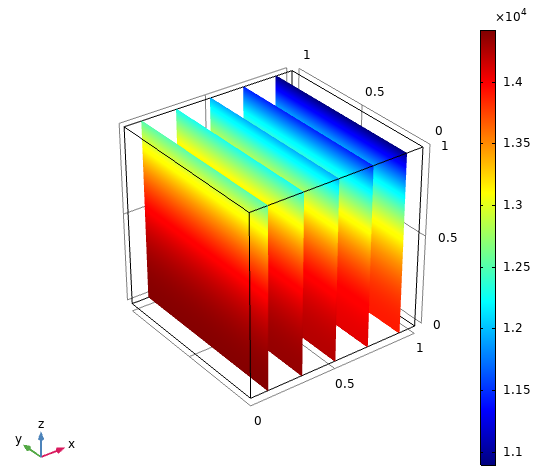


Figure 4.66 2D model, -1mT mbsn 500s.

With the above plots there does not seem to be difference in the concentrations at 500 seconds. Shown in Figure 4.67 are the concentrations in the solid positive electrode at 10 seconds for 0.75mT. Shown in Figure 4.68 are the concentrations in the solid positive electrode at 10 seconds for -1mT.

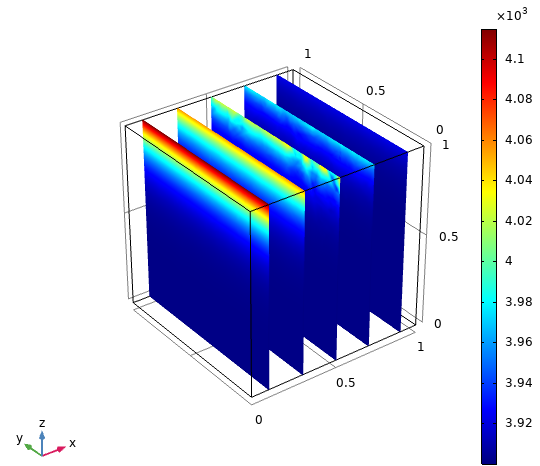
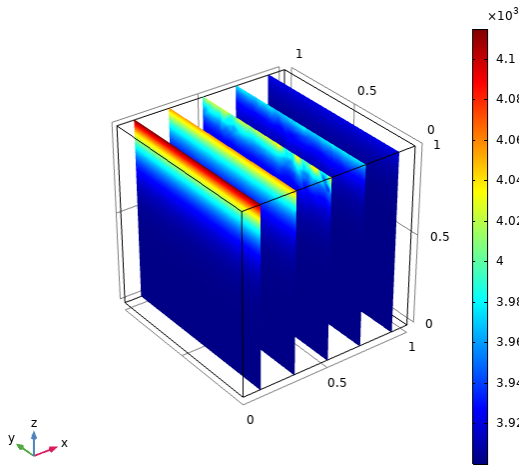


Figure 4.67 2D model, 0.75mT mbsp 10s.

Figure 4.68 2D model, -1mT mbsp 10s.

With the above plots there does not seem to be difference in the concentrations at 10 seconds. Shown in Figure 4.69 are the concentrations in the solid positive electrode at 2500 seconds for 0.75mT. Shown in Figure 4.69 are the concentrations in the solid positive electrode at 2500 seconds for -1mT.

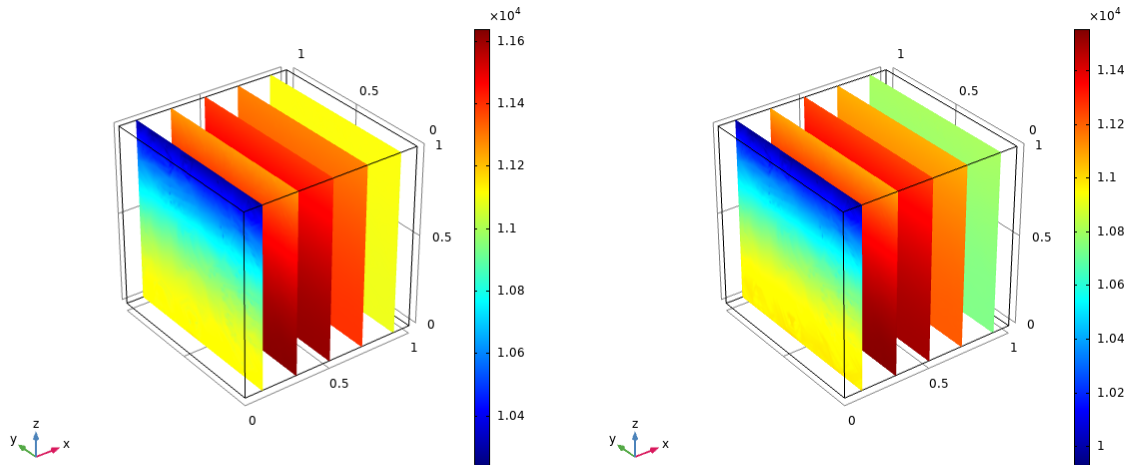


Figure 4.69 2D model, 0.75mT mbsp 500s. **Figure 4.70** 2D model, -1mT mbsp 500s.

There a noticeable difference in the concentrations in the positive electrode at 2500 seconds.

4.2.10 PMF CBSN

In this section is the potential in the solid negative electrode during a discharge, charge, and rest period. Shown in Figure 4.71 is the potential from 0 to 2000 seconds in the negative electrode for 0.75mT. Shown in Figure 4.72 is the potential from 0 to 2000 seconds in the negative electrode for -1mT.

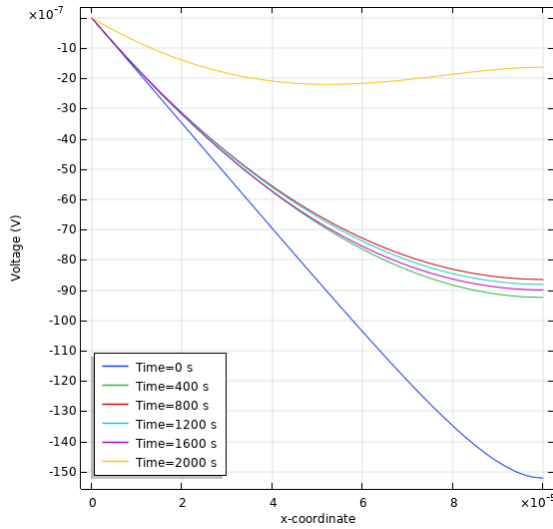


Figure 4.71 2D model, 0.75mT cbsn 0-2000s.

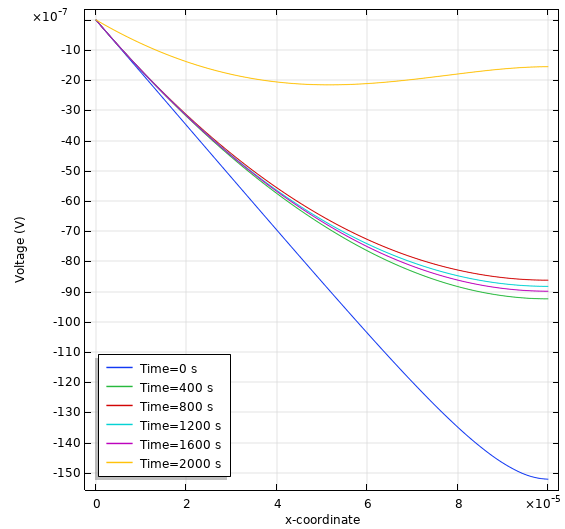


Figure 4.72 2D model, -1mT cbsn 0-2000s.

There is a noticeable difference at 2000 seconds for the potential in the negative electrode. Shown in Figure 4.73 is the potential from 2000 to 4000 seconds in the negative electrode for 0.75mT. Shown in Figure 4.74 is the potential from 0 to 2000 seconds in the negative electrode for -1mT.

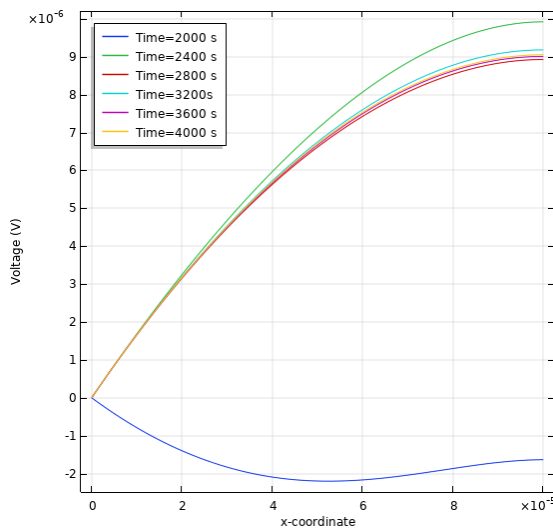


Figure 4.73 2D model, 0.75mT cbsn 2000s-4000s.

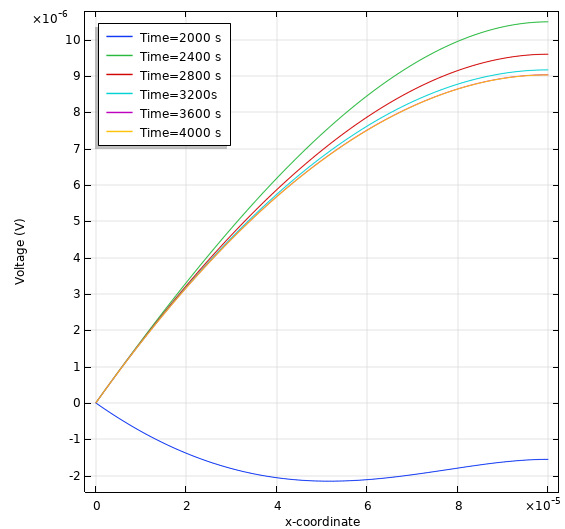


Figure 4.74 2D model, -1mT cbsn 2000s-4000s.

There is a noticeable difference at 2800 seconds for the potential in the negative

electrode. Shown in Figure 4.73 is the potential from 4000 to 5000 seconds in the negative electrode for 0.75mT. Shown in Figure 4.74 is the potential from 4000 to 5000 seconds in the negative electrode for -1mT.

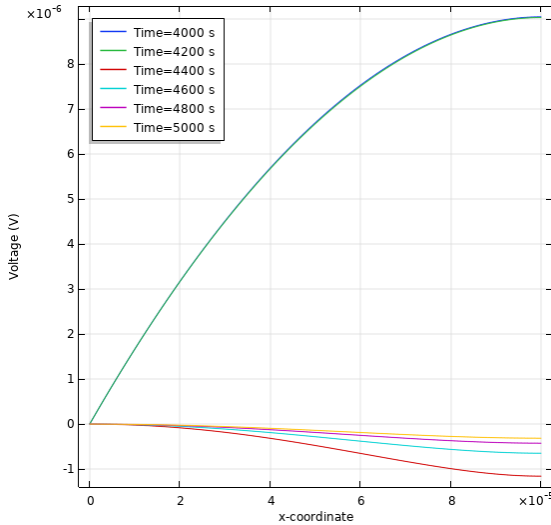


Figure 4.75 2D model, 0.75mT cbsn 4000s-5000s.

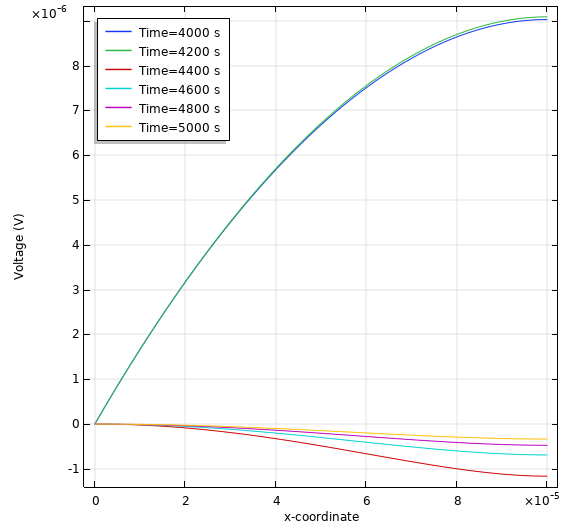


Figure 4.76 2D model, -1mT cbsn 4000s-5000s.

There seems to be a slight variation between 4000 seconds and 4200 seconds. There is more variation in the potential in the negative electrode with -1mT.

4.3 Experimental Measurements

4.3.1 Magnetic Fields Generated from Coil

Shown below in Figure 4.77 is when the magnetic field sensor was 2mm into the top of coil at various currents into the coil. Shown below in Figure 4.78 is when the magnetic field sensor was 0mm into the top of the coil at various currents into the coil.

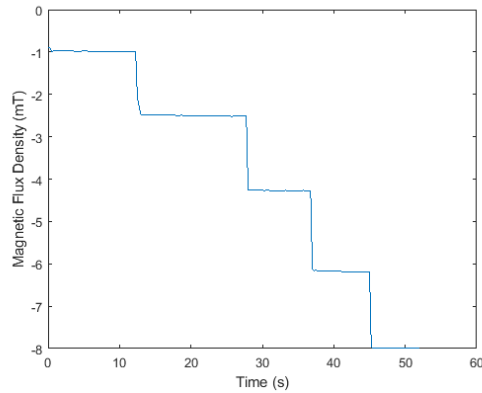


Figure 4.77 Magnetic fields 2mm into top of coil.

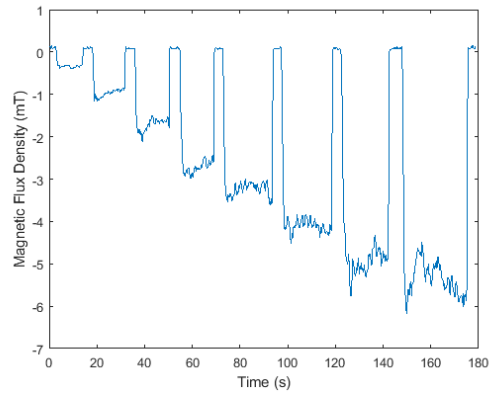


Figure 4.78 Magnetic fields 0mm into top of coil.

In Figure 4.77, 0-10 seconds is when there was 100mA into the coil, 15-30 seconds is when there was 200mA into the coil, 30-35 seconds is when there was 300mA into the coil, 35-40 seconds is when there was 400mA into the coil, and 40-45 seconds is when there was 500mA into the coil.

In Figure 4.78, 0-20 seconds is when there was 100mA into the coil, 20-30 seconds is when there was 200mA into the coil, 40-50 seconds is when there was 300mA into the coil, 50-70 seconds is when there 400mA into the coil, 70-90 seconds is when there was 500mA into the coil, 90-110 seconds is when there was 600mA into the coil, 130-150 seconds is when there was 700mA into the coil, and 150-170 is when there was 800mA into the coil.

Shown below in Figure 4.79 is when the magnetic field sensor was 2mm into the bottom of coil at various currents into the coil. Shown below in Figure 4.80 is when the magnetic field sensor was 0mm into the bottom of the coil at various currents into the coil.

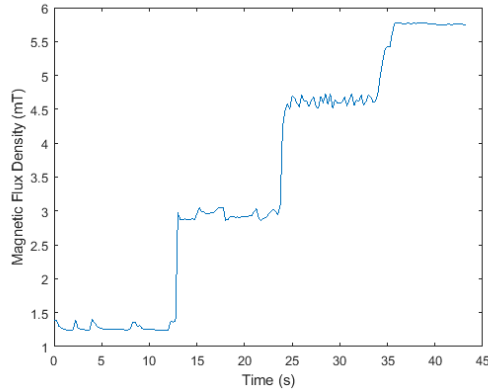


Figure 4.79 Magnetic fields 2mm into bottom of coil.

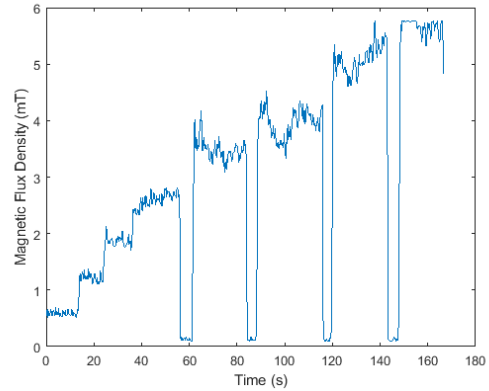


Figure 4.80 Magnetic fields 0mm into bottom of coil.

In Figure 4.79, 0-10 seconds is when there was 100mA into the coil, 15-25 seconds is when there was 200mA into the coil, 25-35 seconds is when there was 300mA into the coil, and 35-40 seconds is when there was 400mA into the coil

In Figure 4.80, 0-10 seconds is when there was 100mA into the coil, 10-30 seconds is when there was 200mA into the coil, 30-40 seconds is when there was 300mA into the coil, 40-60 seconds is when there 400mA into the coil, 60-80 seconds is when there was 500mA into the coil, 90-110 seconds is when there was 600mA into the coil, 120-140 seconds is when there was 700mA into the coil, and 150-170 is when there was 800mA into the coil.

4.3.2 Small Battery LTB8

Shown below Figure 4.81 are the charge currents in the absence of a magnetic field (No Field), the field generated at the top with 800mA in the coil (Field Top 800mA), the field generated at the bottom with 800mA in the coil (Field Bottom), and the field generated at the top with 300mA in the coil (Field Top 300mA). Shown below Figure 4.82 are the charge voltages in the absence of a magnetic field (No Field), the field generated at the top

with 800mA in the coil (Field Top 800mA), the field generated at the bottom with 800mA in the coil (Field Bottom), and the field generated at the top with 300mA in the coil (Field Top 300mA).

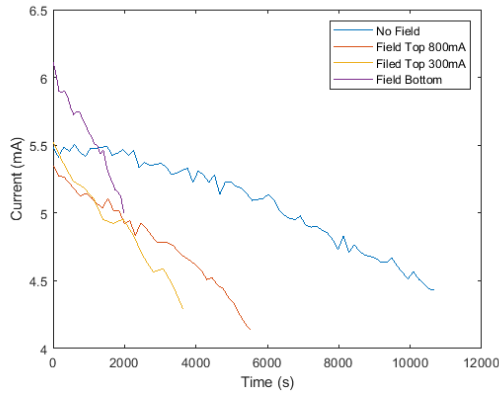


Figure 4.81 Small battery LTB8 charge current.

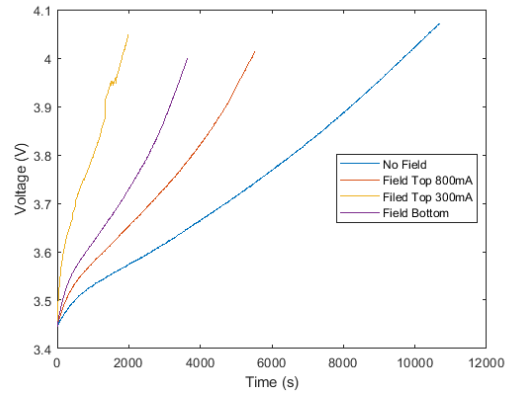


Figure 4.82 Small battery LTB8 charge voltage.

The voltages in Figure 4.82 are to be viewed with caution as of the loading effect of the charge circuit. The battery was charged from 3.45V to 4V in the specified conditions. The currents into the battery were all in the same relative range to keep the same charge rate. Looking at Figure 4.82 the presence of the magnetic field affected the charging time for the battery. Instead of taking 10000 seconds to charge, the magnetic field reduced the time to 3000 seconds. Changing the direction of the magnetic field also had a noticeable effect on the charge times. Decreasing the current into the coil also had effect seen in the reduction of the charge time. Shown below in Figure 4.83 is a plot of the magnetic flux densities versus charging time.

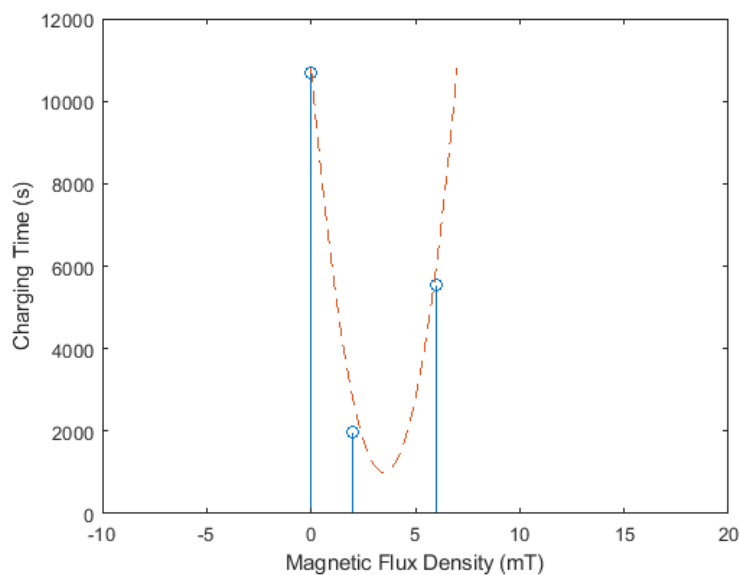


Figure 4.83 Small battery LTB8 optimal.

As can be seen in the above plot, there appears to be an optimal charging magnetic flux density. This plot is a projection based on the three data points for this charge curve; 0mT, 3mT, and 6mT. This optimal solution corresponds to the shortest charging time for when the battery was charged from 3.5V to 4.0V.

Shown below Figure 4.84 are the discharge currents in the absence of a magnetic field (No Field), the field generated at the top with 800mA in the coil (Field Top 800mA), the field generated at the bottom with 800mA in the coil (Field Bottom), and the field generated at the top with 300mA in the coil (Field Top 300mA). Shown below Figure 4.85 are the discharge voltages in the absence of a magnetic field (No Field), the field generated at the top with 800mA in the coil (Field Top 800mA), the field generated at the bottom with 800mA in the coil (Field Bottom), and the field generated at the top with 300mA in the coil (Field Top 300mA).

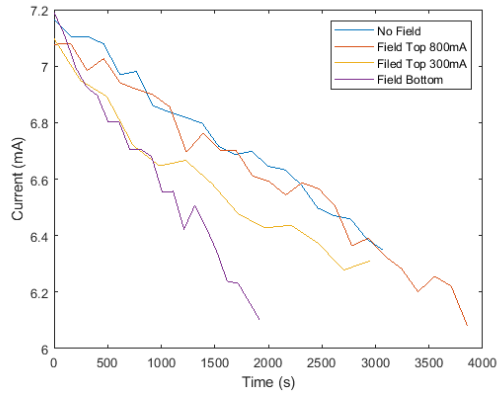


Figure 4.84 Small battery LTB8 discharge current.

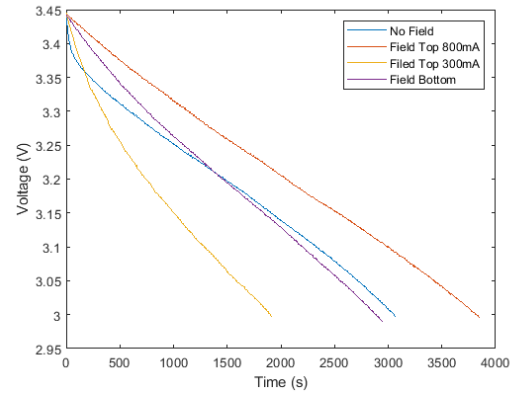


Figure 4.85 Small battery LTB8 discharge voltage.

The voltages in Figure 4.85 are to be viewed with caution as of the loading effect of the discharge circuit. The battery was discharged from 3.45V to 3V in the specified conditions. The currents into the battery were all in the same relative range to keep the same discharge rate. Looking at Figure 4.85 the presence of the magnetic field affected the discharging time for the battery. Instead of taking 3000 seconds to discharge, the magnetic field reduced the time to 2000 seconds. Changing the direction of the magnetic field also had a noticeable effect on the discharge times. The magnitude of the field increased the discharge time for the case of (Field Top 800mA) and decreased the discharge time in the case of (Field Top 300mA). The direction of the magnetic field also had a noticeable effect.

4.3.3 Small Battery LTB1

Shown below Figure 4.86 are the charge currents in the absence of a magnetic field (No Field), the field generated at the top with 800mA in the coil (Field Top 800mA), the field generated at the bottom with 800mA in the coil (Field Bottom), and the field generated at the top with 300mA in the coil (Field Top 300mA). Shown below Figure 4.87 are the charge voltages in the absence of a magnetic field (No Field), the field generated at the top

with 800mA in the coil (Field Top 800mA), the field generated at the bottom with 800mA in the coil (Field Bottom), and the field generated at the top with 300mA in the coil (Field Top 300mA).

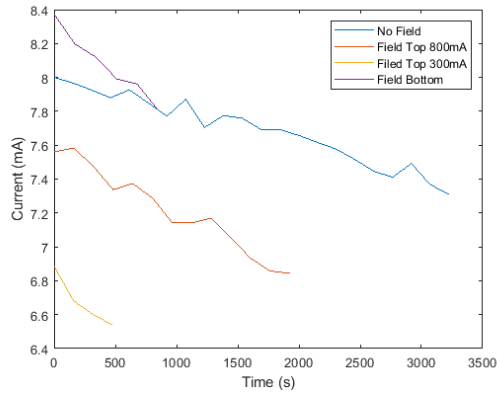


Figure 4.86 Small battery LTB1 charge current.

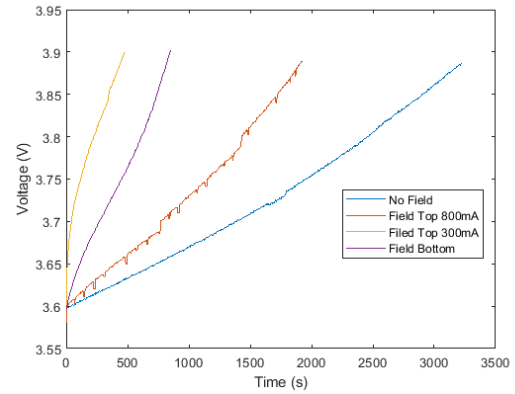


Figure 4.87 Small battery LTB1 charge voltage.

The voltages in Figure 4.87 are to be viewed with caution as of the loading effect of the charge circuit. The battery was charged from 3.6V to 3.9V in the specified conditions. The currents into the battery were all in the same relative range to keep the same charge rate. Looking at Figure 4.87 the presence of the magnetic field affected the charging time for the battery. Instead of taking 3500 seconds to charge, the magnetic field reduced the time to 1500 seconds. Changing the direction of the magnetic field also had a noticeable effect on the charge times. Decreasing the current into the coil also had effect seen in the reduction of the charge time. Shown below in Figure 4.88 is a plot of the magnetic flux densities versus charging time.

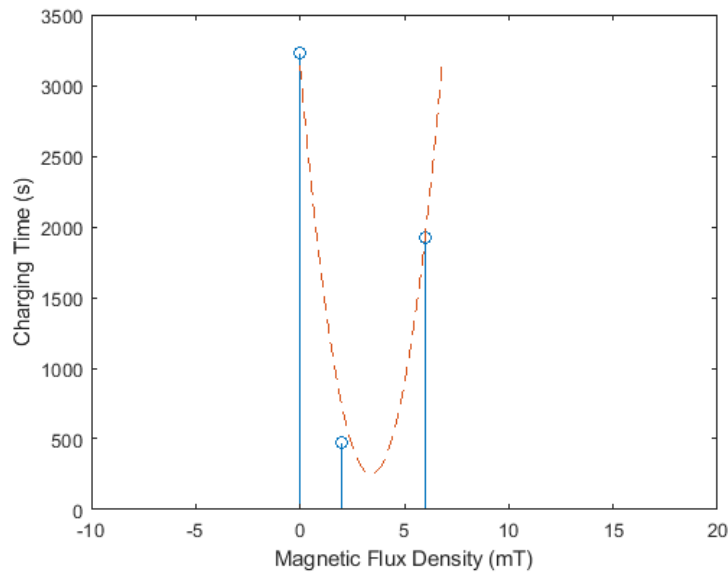


Figure 4.88 Small battery LTB1 optimal.

As can be seen in the above plot, there appears to be an optimal charging magnetic flux density. This plot is a projection based on the three data points for this charge curve; 0mT, 3mT, and 6mT. This optimal solution corresponds to the shortest charging time for when the battery was charged from 3.6V to 3.9V.

Shown below Figure 4.89 are the discharge currents in the absence of a magnetic field (No Field), the field generated at the top with 800mA in the coil (Field Top 800mA), the field generated at the bottom with 800mA in the coil (Field Bottom), and the field generated at the top with 300mA in the coil (Field Top 300mA). Shown below Figure 4.90 are the discharge voltages in the absence of a magnetic field (No Field), the field generated at the top with 800mA in the coil (Field Top 800mA), the field generated at the bottom with 800mA in the coil (Field Bottom), and the field generated at the top with 300mA in the coil (Field Top 300mA).

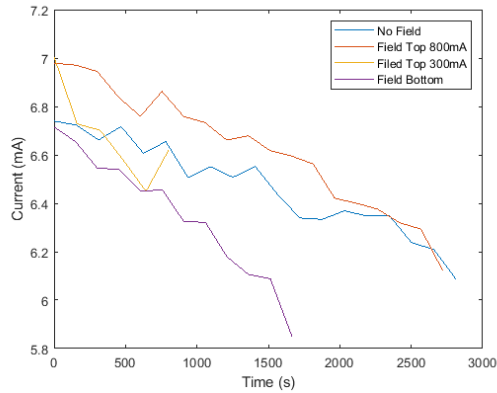


Figure 4.89 Small battery LTB1 discharge current.

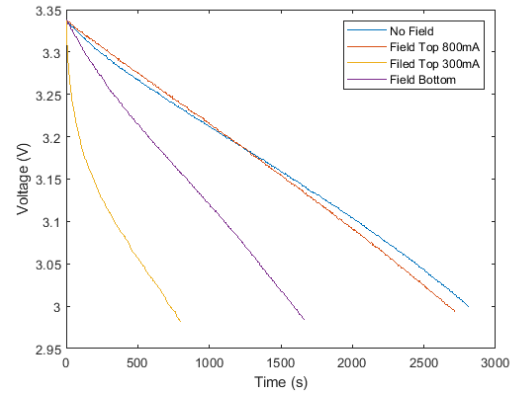


Figure 4.90 Small battery LTB1 discharge voltage.

The voltages in Figure 4.90 are to be viewed with caution as of the loading effect of the discharge circuit. The battery was discharged from 3.43V to 3V in the specified conditions. The currents into the battery were all in the same relative range to keep the same discharge rate. Looking at Figure 4.90 the presence of the magnetic field affected the discharging time for the battery. Instead of taking 3000 seconds to discharge, the magnetic field reduced the time to 2000 seconds. Changing the direction of the magnetic field also had a noticeable effect on the discharge times. The magnitude of the field decreased the discharge time for the case of (Field Top 800mA) and decreased the discharge time in the case of (Field Top 300mA). The direction of the magnetic field also had a noticeable effect.

4.3.4 Big Battery FE19

Shown below Figure 4.91 are the charge currents in the absence of a magnetic field (No Field), the field generated at the top with 800mA in the coil (Field Top 800mA), the field generated at the bottom with 800mA in the coil (Field Bottom), and the field generated at the top with 300mA in the coil (Field Top 300mA). Shown below Figure 4.92 are the charge voltages in the absence of a magnetic field (No Field), the field generated at the top

with 800mA in the coil (Field Top 800mA), the field generated at the bottom with 800mA in the coil (Field Bottom), and the field generated at the top with 300mA in the coil (Field Top 300mA).

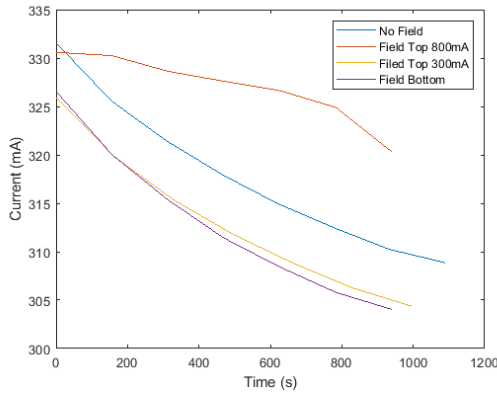


Figure 4.91 Big battery FE19 charge current.

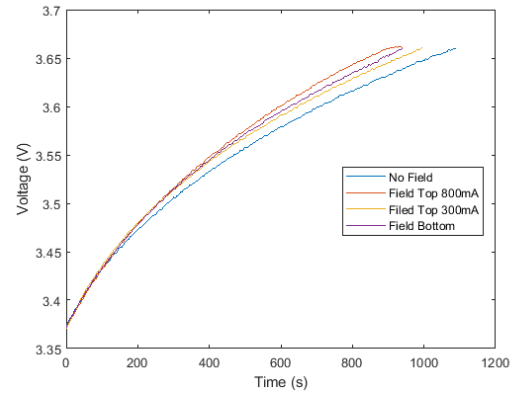


Figure 4.92 Big battery FE19 charge voltage.

The voltages in Figure 4.92 are to be viewed with caution as of the loading effect of the charge circuit. The battery was charged from 3.4V to 3.65V in the specified conditions. The currents into the battery were all in the same relative range to keep the same charge rate. Looking at Figure 4.87 the presence of the magnetic field affected the charging time for the battery slightly. Instead of taking 1000 seconds to charge, the magnetic field reduced the time to 900 seconds. Changing the direction of the magnetic field also had a slightly noticeable effect on the charge times. Decreasing the current into the coil slightly increased the charge time. At the same time, this battery consists of a stacked number of cells which prevent equal penetration of the magnetic field into each individual cell.

Shown below Figure 4.93 are the discharge currents in the absence of a magnetic field (No Field), the field generated at the top with 800mA in the coil (Field Top 800mA), the field generated at the bottom with 800mA in the coil (Field Bottom), and the field generated at the top with 300mA in the coil (Field Top 300mA). Shown below Figure 4.94

are the discharge voltages in the absence of a magnetic field (No Field), the field generated at the top with 800mA in the coil (Field Top 800mA), the field generated at the bottom with 800mA in the coil (Field Bottom), and the field generated at the top with 300mA in the coil (Field Top 300mA).

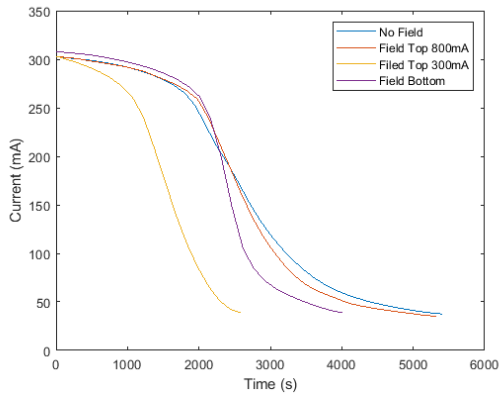


Figure 4.93 Big battery FE19 discharge current.

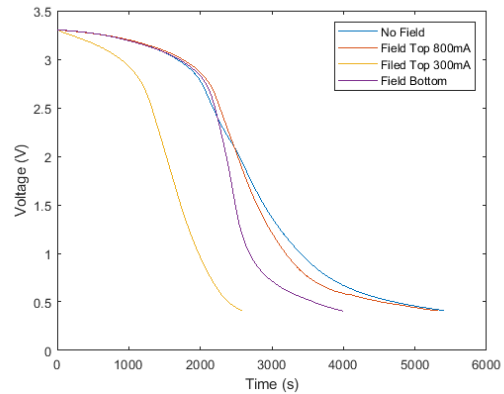


Figure 4.94 Big battery FE19 discharge voltage.

The voltages in Figure 4.94 are to be viewed with caution as of the loading effect of the discharge circuit. The battery was discharged from 3.4V to 0.5V in the specified conditions. The currents into the battery were all in the same relative range to keep the same discharge rate. Looking at Figure 4.94 the presence of the magnetic field affected the discharging time for the battery. Instead of taking 5000 seconds to discharge, the magnetic field reduced the time to 3500 seconds. Changing the direction of the magnetic field also had a noticeable effect on the discharge times. The magnitude of the field slightly decreased the discharge time for the case of (Field Top 800mA) and noticeably decreased the discharge time in the case of (Field Top 300mA). The direction of the magnetic field also had a noticeable effect.

CHAPTER 5

CONCLUSION

Starting with the one-dimensional model it was found that it matched very closely with COMSOL's pre-built one-dimensional model. With that foundation, a two-dimensional model was constructed that would allow the affects of a magnetic field influence its characteristics. Two dimensions were needed because of the cross-product in the Lorentz force and Hall effect. With various impressed external magnetic field intensities an effect was noticed on the charge and discharge curves as well as the charge and mass concentrations within the batteries. With the two-dimensional model starting from 0mT and going to 1mT had the effect of discharging the battery faster and charging the battery faster. With the two-dimensional model starting from 1mT and going to -1mT had the effect of charging the battery faster. In either case an effect on the various characteristics of the battery were studied.

With the experiments conducted on the two types of batteries the effect was more profound than subtle. Discharge times were twice as fast and charge times were equally affected. With the smaller batteries they all generally charged faster under the presence of a magnetic field due to more uniform penetration. In the presence of the field they also discharged faster. The larger batteries would not see the same uniform penetration because only a small area of the battery sees the center of the coil it is placed on. Decreasing the magnetic field had the effect of increasing the charging time implying a parabola-like relationship. This would mean that an optimal magnetic field would result in an optimal charging time. For the larger battery the battery generally discharged faster in the presence

of the magnetic field, but did not have an equally as great of a change in charging speed.

Looking at the simulations and experimental results they do not agree with each other completely. This is due to the fact that the model constructed is based on materials and parameters from COMSOL. To build a more accurate model, the initial concentrations in both electrodes, the conductivity, the diffusion coefficients, the equilibrium potentials, and the exact lengths and widths of the batteries would be needed. Measuring these parameters and constants is pretty difficult almost impossible in real-life batteries. Both the simulation and the experimental results show the general trend that magnetic fields can have an observable effect on the discharge and charge cycles of lithium ion batteries.

REFERENCES

- 1 D. Ebbing and M. Wrighton, "General Chemistry", 11th ed. Boston: Cengage Learning, 2017, pp. 663-668.
- 2 C. Rahn and Z. Wang, "Battery Systems Engineering", 1st ed. Hoboken: John Wiley & Sons Inc, 2013, pp. 7-8.
- 3 J. Warner, "The Handbook of Lithium-Ion Battery Pack Design", 1st ed. Amsterdam: Elsevier, 2015, pp. 75-76.
- 4 M. Gulbinska, B. Ravdel, F. Puglia, S. Cohen and S. Santee, "Lithium-Ion Battery Materials and Engineering", 1st ed. Springer, 2014, pp. 3-23.
- 5 J. Jiang and C. Zhang, "Fundamentals and Applications of Lithium-Ion Batteries in Electric Drive Vehicles" Singapore: Wiley, 2015, p. 10.
- 6 V. Ramadesigan, P. Northrop, S. De, S. Santhanagopalan, R. Braatz and V. Subramanian, "Modeling and Simulation of Lithium-Ion Batteries from a Systems Engineering Perspective", Journal of The Electrochemical Society, vol. 159, no. 3, pp. R31-R45, 2012. Available: 10.1149/2.018203jes.
- 7 Q. Li, S. Tan, L. Li, Y. Lu and Y. He, "Understanding the molecular mechanism of pulse current charging for stable lithium-metal batteries", Science Advances, vol. 3, no. 7, p. e1701246, 2017. Available: 10.1126/sciadv.1701246.
- 8 T. Fuller, M. Doyle and J. Newman, "Simulation and Optimization of the Dual Lithium Ion Insertion Cell", Journal of The Electrochemical Society, vol. 141, no. 1, p. 1, 1994. Available: 10.1149/1.2054684.
- 9 A. Nyman and H. Ekstrom, "Modeling the Lithium-ion battery", COMSOL White Paper, 2012
- 10 M. Cugnet, "Highly Accurate Li-ion Battery Simulation", COMOSOL White Paper, 201
- 11 K. Smith, C. Rahn and C. Wang, "Control oriented 1D electrochemical model of lithium ion battery", Energy Conversion and Management, vol. 48, no. 9, pp. 2565-2578, 2007. Available: 10.1016/j.enconman.2007.03.015.
- 12 L. Cai and R. White, "Mathematical modeling of a lithium ion battery with thermal effects in COMSOL Inc. Multiphysics (MP) software", Journal of Power Sources, vol. 196, no. 14, pp. 5985-5989, 2011. Available: 10.1016/j.jpowsour.2011.03.017.
- 13 A. Latz and J. Zausch, "Thermodynamic consistent transport theory of Li-ion batteries", Journal of Power Sources, vol. 196, no. 6, pp. 3296-3302, 2011. Available: 10.1016/j.jpowsour.2010.11.088.

- 14 X. Zhang, J. Lu, S. Yuan, J. Yang and X. Zhou, "A novel method for identification of lithium-ion battery equivalent circuit model parameters considering electrochemical properties", *Journal of Power Sources*, vol. 345, pp. 21-29, 2017. Available: 10.1016/j.jpowsour.2017.01.126.
- 15 E. Kelly, "Magnetic Field Effects on Electrochemical Reactions Occurring at Metal/Flowing Electrolyte Interfaces", *Journal of The Electrochemical Society*, vol. 124, no. 7, p. 987, 1977. Available: 10.1149/1.2133514.
- 16 P. Singh, N. Khare and P. Chaturvedi, "Li-ion battery ageing model parameter: SEI layer analysis using magnetic field probing", *Engineering Science and Technology, an International Journal*, vol. 21, no. 1, pp. 35-42, 2018. Available: 10.1016/j.jestch.2018.01.007.
- 17 P. Singh, N. Khare and P. Chaturvedi, "COMSOL Modelling for Li-ion Battery Diagnostics", in *COMSOL Conference 2015 Pune*, Pune, 2015.
- 18 N. Trease, T. Ko ster and C. Grey, "In Situ NMR Studies of Lithium Ion Batteries", *Interface magazine*, vol. 20, no. 3, pp. 69-73, 2011. Available: 10.1149/2.f07113if.
- 19 L. Zhai, G. Lee, X. Gao, X. Zhang, Z. Gu and M. Zou, "Impact of Electromagnetic Interforance from Power Inverter Drive System on Batteries in Electric Vehicle", *Energy Procedia*, vol. 88, pp. 881-888, 2016. Available: 10.1016/j.egypro.2016.06.105.
- 20 "Designing EMI/EMC Safe Battery Pack", Texas Instruments, SLUA776-July 2016.
- 21 H. Maleki, R. Zurek, J. Howard and J. Hallmark, "Lithium Ion Cell/Batteries Electromagnetic Field Reduction in Phones for Hearing Aid Compliance", *Batteries*, vol. 2, no. 2, p. 19, 2016. Available: 10.3390/batteries2020019.
- 22 M. Doyle and J. Newman, "Comparison of Modeling Predictions with Experimental Data from Plastic Lithium Ion Cells", *Journal of The Electrochemical Society*, vol. 143, no. 6, p. 1890, 1996. Available: 10.1149/1.1836921.
- 23 O. Aiello, P.S. Croveti, F. Fiori, "Susceptibility to EMI of a Battery Management System IC for electric vehicles", 2015 IEEE International Symposium on Electromagnetic Compatibility (EMC), Dresden, Germany, August 16-22, 2015, IEEE, pp. 749-754.